

# Jordan Journal of Mechanical and Industrial Engineering (JJMIE)

JJMIE is a high-quality scientific journal devoted to fields of Mechanical and Industrial Engineering. It is published by The Hashemite University in corporation with the Jordanian Scientific Research Support Fund.

## EDITORIAL BOARD

---

### Editor-in-Chief

Prof. **Nabil Anagreh**

### Editorial board

Prof. **Mohammad Ahmad Hamdan**  
The University of Jordan

Prof. **Oqab Al-Fayez**  
The University of Jordan

Prof. **Amin Al Robaidi**  
Al Balqa Applied University

Prof. **Naser Al-Huniti**  
The University of Jordan

Prof. **Suhil Kiwan**  
The Jordan University of Science and Technology

Prof. **Mahmoud Abu-Zaid**  
Mutah University

### Assistant Editor

**Dr. Khalid Al-Widyan**  
Hashemite University

## THE INTERNATIONAL ADVISORY BOARD

---

**Abu-Qudais, Mohammad**  
Jordan University of Science & Technology, Jordan

**Abu-Mulaweh, Hosni**  
Purdue University at Fort Wayne, USA

**Afaneh Abdul-Hafiz**  
Robert Bosch Corporation, USA

**Afonso, Maria Dina**  
Institute Superior Tecnico, Portugal

**Badiru, Adedji B.**  
The University of Tennessee, USA

**Bejan, Adrian**  
Duke University, USA

**Chalhoub, Nabil G.**  
Wayne State University, USA

**Cho, Kyu-Kab**  
Pusan National University, South Korea

**Dincer, Ibrahim**  
University of Ontario Institute of Technology,  
Canada

**Douglas, Roy**  
Queen's University, U. K

**El Bassam, Nasir**  
International Research Center for Renewable  
Energy, Germany

**Haik, Yousef**  
United Arab Emirates University, UAE

**Jaber, Jamal**  
Al- Balqa Applied University, Jordan

**Jubran, Bassam**  
Ryerson University, Canada

**Kakac, Sadik**  
University of Miami, USA

**Khalil, Essam-Eddin**  
Cairo University, Egypt

**Mutoh, Yoshiharu**  
Nagaoka University of Technology, Japan

**Pant, Durbin**  
Iowa State University, USA

**Riffat, Saffa**  
The University of Nottingham, U. K

**Saghir, Ziad**  
Ryerson University, Canada

**Sarkar, MD. Abdur Rashid**  
Bangladesh University of Engineering &  
Technology, Bangladesh

**Siginer, Dennis**  
Wichita State University, USA

**Sopian, Kamaruzzaman**  
University Kebangsaan Malaysia, Malaysia

**Tzou, Gow-Yi**  
Yung-Ta Institute of Technology and Commerce,  
Taiwan

## EDITORIAL BOARD SUPPORT TEAM

---

### Language Editor

Dr. Qusai Al-Debyan

### Publishing Layout

Eng. Ali Abu Salimeh

## SUBMISSION ADDRESS:

---

Prof. **Nabil Anagreh**, Editor-in-Chief  
Jordan Journal of Mechanical & Industrial Engineering,  
Hashemite University,  
PO Box 330127, Zarqa, 13133, Jordan  
E-mail: jjmie@hu.edu.jo



Hashemite Kingdom of Jordan



Hashemite University

Jordan Journal of  
Mechanical and Industrial Engineering

JJMIIE

*An International Peer-Reviewed Scientific Journal*  
*Financed by Scientific Research Support Fund*

<http://jjmie.hu.edu.jo/>

ISSN 1995-6665

# Jordan Journal of Mechanical and Industrial Engineering (JJMIE)

JJMIE is a high-quality scientific journal devoted to fields of Mechanical and Industrial Engineering. It is published by The Jordanian Ministry of Higher Education and Scientific Research in corporation with the Hashemite University.

**Introduction:** The Editorial Board is very committed to build the Journal as one of the leading international journals in mechanical and industrial engineering sciences in the next few years. With the support of the Ministry of Higher Education and Scientific Research and Jordanian Universities, it is expected that a heavy resource to be channeled into the Journal to establish its international reputation. The Journal's reputation will be enhanced from arrangements with several organizers of international conferences in publishing selected best papers of the conference proceedings.

**Aims and Scope:** *Jordan Journal of Mechanical and Industrial Engineering (JJMIE)* is a refereed international journal to be of interest and use to all those concerned with research in various fields of, or closely related to, mechanical and industrial engineering disciplines. *Jordan Journal of Mechanical and Industrial Engineering* aims to provide a highly readable and valuable addition to the literature which will serve as an indispensable reference tool for years to come. The coverage of the journal includes all new theoretical and experimental findings in the fields of mechanical and industrial engineering or any closely related fields (Materials, Manufacturing, Management, Design, Thermal and Fluid, Energy, Control, Mechatronics, and Biomedical). The journal also encourages the submission of critical review articles covering advances in recent research of such fields as well as technical notes.

## Guide for Authors

---

### **Manuscript Submission:**

High-quality submissions to this new journal are welcome now and manuscripts may be either submitted online or email.

**Online:** For online and email submission upload one copy of the full paper including graphics and all figures at the online submission site, accessed via <http://jjmie.hu.edu.jo>. The manuscript must be written in MS Word 2010 Format. All correspondence, including notification of the Editor's decision and requests for revision, takes place by e-mail and via the Author's homepage, removing the need for a hard-copy paper trail.

### **Submission address and contact:**

Prof. Nabil Anagreh  
Editor-in-Chief  
*Jordan Journal of Mechanical & Industrial Engineering*,  
Hashemite University,  
PO Box 330127, Zarqa, 13115, Jordan  
E-mail: [jjmie@hu.edu.jo](mailto:jjmie@hu.edu.jo)

**Types of contributions:** Original research papers and Technical reports

**Corresponding author:** Clearly indicate who is responsible for correspondence at all stages of refereeing and publication, including post-publication. Ensure that telephone and fax numbers (with country and area code) are provided in addition to the e-mail address and the complete postal address. Full postal addresses must be given for all co-authors.

**Original material:** Submission of an article implies that the work described has not been published previously (except in the form of an abstract or as part of a published lecture or academic thesis), that it is not under consideration for publication elsewhere, that its publication is approved by all authors and that, if accepted, it will not be published elsewhere in the same form, in English or in any other language, without the written consent of the Publisher. Authors found to be deliberately contravening the submission guidelines on originality and exclusivity shall not be considered for future publication in this journal.

**Withdrawing:** If the author chooses to withdraw his article after it has been assessed, he shall reimburse JJMIE with the cost of reviewing the paper.

### **Manuscript Preparation:**

---

**General:** Editors reserve the right to adjust style to certain standards of uniformity. Original manuscripts are discarded after publication unless the Publisher is asked to return original material after use. Please use MS Word 2010 for the text of your manuscript.

**Structure:** Follow this order when typing manuscripts: Title, Authors, Authors title, Affiliations, Abstract, Keywords, Introduction, Main text, Conclusions, Acknowledgements, Appendix, References, Figure Captions, Figures and then Tables. Please supply figures imported into the text AND also separately as original graphics files. Collate acknowledgements in a separate section at the end of the article and do not include them on the title page, as a footnote to the title or otherwise.

**Text Layout:** Use 1.5 line spacing and wide (3 cm) margins. Ensure that each new paragraph is clearly indicated. Present tables and figure legends on separate pages at the end of the manuscript. If possible, consult a recent issue of the journal to become familiar with layout and conventions. All footnotes (except for table and corresponding author footnotes) should be identified with superscript Arabic numbers. To conserve space, authors are requested to mark the less important parts of the paper (such as records of experimental results) for printing in smaller type. For long papers (more than 4000 words) sections which could be deleted without destroying either the sense or the continuity of the paper should be indicated as a guide for the editor. Nomenclature should conform to that most frequently used in the scientific field concerned. Number all pages consecutively; use 12 or 10 pt font size and standard fonts.

**Corresponding author:** Clearly indicate who is responsible for correspondence at all stages of refereeing and publication, including post-publication. The corresponding author should be identified with an asterisk and footnote. Ensure that telephone and fax numbers (with country and area code) are provided in addition to the e-mail address and the complete postal address. Full postal addresses must be given for all co-authors. Please consult a recent journal paper for style if possible.

**Abstract:** A self-contained abstract outlining in a single paragraph the aims, scope and conclusions of the paper must be supplied.

**Keywords:** Immediately after the abstract, provide a maximum of six keywords (avoid, for example, 'and', 'of'). Be sparing with abbreviations: only abbreviations firmly established in the field may be eligible.

**Symbols:** All Greek letters and unusual symbols should be identified by name in the margin, the first time they are used.

**Units:** Follow internationally accepted rules and conventions: use the international system of units (SI). If other quantities are mentioned, give their equivalent in SI.

**Maths:** Number consecutively any equations that have to be displayed separately from the text (if referred to explicitly in the text).

**References:** All publications cited in the text should be presented in a list of references following the text of the manuscript.

*Text:* Indicate references by number(s) in square brackets in line with the text. The actual authors can be referred to, but the reference number(s) must always be given.

*List:* Number the references (numbers in square brackets) in the list in the order in which they appear in the text.

**Examples:**

**Reference to a journal publication:**

[1] M.S. Mohsen, B.A. Akash, "Evaluation of domestic solar water heating system in Jordan using analytic hierarchy process". Energy Conversion & Management, Vol. 38 (1997) No. 9, 1815-1822.

**Reference to a book:**

[2] Strunk Jr W, White EB. The elements of style. 3rd ed. New York: Macmillan; 1979.

**Reference to a conference proceeding:**

[3] B. Akash, S. Odeh, S. Nijmeh, "Modeling of solar-assisted double-tube evaporator heat pump system under local climate conditions". 5th Jordanian International Mechanical Engineering Conference, Amman, Jordan, 2004.

**Reference to a chapter in an edited book:**

[4] Mettam GR, Adams LB. How to prepare an electronic version of your article. In: Jones BS, Smith RZ, editors. Introduction to the electronic age, New York: E-Publishing Inc; 1999, p. 281-304

**Free Online Color :** If, together with your accepted article, you submit usable color and black/white figures then the journal will ensure that these figures will appear in color on the journal website electronic version.

**Tables:** Tables should be numbered consecutively and given suitable captions and each table should begin on a new page. No vertical rules should be used. Tables should not unnecessarily duplicate results presented elsewhere in the manuscript (for example, in graphs). Footnotes to tables should be typed below the table and should be referred to by superscript lowercase letters.

**Notification:** Authors will be notified of the acceptance of their paper by the editor. The Publisher will also send a notification of receipt of the paper in production.

**Copyright:** All authors must sign the Transfer of Copyright agreement before the article can be published. This transfer agreement enables Jordan Journal of Mechanical and Industrial Engineering to protect the copyrighted material for the authors, but does not relinquish the authors' proprietary rights. The copyright transfer covers the exclusive rights to reproduce and distribute the article, including reprints, photographic reproductions, microfilm or any other reproductions of similar nature and translations.

**Proof Reading:** One set of page proofs in MS Word 2010 format will be sent by e-mail to the corresponding author, to be checked for typesetting/editing. The corrections should be returned within **48 hours**. No changes in, or additions to, the accepted (and subsequently edited) manuscript will be allowed at this stage. Proofreading is solely the author's responsibility. Any queries should be answered in full. Please correct factual errors only, or errors introduced by typesetting. Please note that once your paper has been proofed we publish the identical paper online as in print.

**Author Benefits:**

*No page charges:* Publication in this journal is free of charge.

*Free offprints:* One journal issues of which the article appears will be supplied free of charge to the corresponding author and additional offprint for each co-author. Corresponding authors will be given the choice to buy extra offprints before printing of the article.



<b>PAGES</b>	<b>PAPERS</b>
241 - 252	<b>Validation of a Zero-Dimensional Model for Prediction of Engine Performances with FORTRAN and GT-Power Software.</b> <i>Brahim Menacer and Mostefa Bouchetara.</i>
253 - 261	<b>Numerical Simulation and Nonlinear Stability Analysis of Francis Hydraulic Turbine-Seal System.</b> <i>Qianqian Wu, Leike Zhang and Zhenyue Ma</i>
263– 268	<b>The Effects of a Magnetic Gradient on Lifted Diffusion Flames.</b> <i>Ibrahim Mabrouki, Mohamed Ali Merghini, Zied Driss and Mohamed Salah Abid</i>
269– 278	<b>The Effect of the Couple Stress Fluid Flow on MHD Peristaltic Motion with Uniform Porous Medium in the Presence of Slip Effect.</b> <i>Dr. S. Ravi Kumar</i>
279– 288	<b>The Effect of Chemical Reaction and Double Stratification on MHD Free Convection in a Micropolar Fluid with Heat Generation and Ohmic Heating.</b> <i>Khilap Singh and Manoj Kumar</i>
289– 296	<b>Thermodynamic Analysis of R152a and Dimethylether Refrigerant Mixtures in Refrigeration System.</b> <i>Ayyalusamy Baskaran and Koshy Mathews.</i>
297– 301	<b>Effect of 4%wt. Cu Addition on the Mechanical Characteristics and Fatigue Life of Commercially Pure Aluminum.</b> <i>Nabeel Alshabatat and Safwan Al-qawabah</i>
303– 317	<b>Implementation of Systems Engineering Lifecycle-Tools-Model Framework on Large Industrial Scale.</b> <i>Islam Helaly Afefy, Ahmed Mohamed El-kamash and Nihal Mahmoud El-Sayar.</i>

---



# Validation of a Zero-Dimensional Model for Prediction of Engine Performances with FORTRAN and GT-Power Software

Brahim Menacer \* and Mostefa Bouchetara

Aeronautics and Systems Propelling Laboratory, Department of Mechanical Engineering, University of Sciences and the Technology of Oran, BP 1505 El-Mnaouer, USTO 31000 ORAN (Algeria) Oran 31000 Algeria

Received 21 Dec 2014

Accepted 29 Jun 2015

## Abstract

The increasing complexity of modern engines has rendered the prototyping phase long and expensive. This is where engine modelling has become, in the recent years, extremely useful and can be used as an indispensable tool when developing new engine concepts. The purpose of this work was to provide a flexible thermodynamic model based on the filling-and-emptying approach for the performance prediction of a four-stroke turbocharged compression ignition engine and to present in the qualitatively point of review the effect of a number of parameters considered affecting the performance of turbocharged diesel engines. To validate the model, comparisons were made between results from a computer program developed using FORTRAN language and the commercial GT-Power software operating under different conditions. The comparisons showed that there was a good concurrence between the developed program and the commercial GT-Power software. The range of variation of the rotational speed of the diesel engine chosen extends from 800 to 2100 RPM. By analyzing these parameters with regard to two optimal points in the engine, one relative to maximum power and another to maximum efficiency, it was found that the parameters as stroke-bore ratio and the cylinder wall temperature have a small influence on the brake power and effective efficiency. While the angle of start injection, mass fuel injected, compression ratio have a great influence on the brake power and effective efficiency.

© 2015 Jordan Journal of Mechanical and Industrial Engineering. All rights reserved

**Keywords:** Single-Zone Model, Ignition Compression Engine, Heat Transfer, Friction, Turbocharged Diesel Engine, GT-Power, Performance Optimization.

## NOMONCLATURE

$C_i$	krieger and borman constants	$\dot{m}_{fb}$	burned fuel mass rate
$c_p$	specific heat at constant pressure	$\dot{m}_{fb}^*$	normalized burned fuel mass rate
$c_v$	specific heat at constant volume	$m_f$	injected fuel mass per cycle
$c_r$	compression ratio	$(\dot{m}_{fb})_p$	normalized fuel burning rate in the premixed combustion
$D$	cylinder bore	$(\dot{m}_{fb})_d$	normalized fuel burning rate in the diffusion combustion
$h_{for}$	enthalpy of formation of the fuel	$\dot{m}_{in}$	mass flow through the intake valve
$k_{hoh}$	constant of Hohenberg	$\dot{m}_{out}$	mass flow through the exhaust valve
$q_{LHV}$	lower heating value of fuel	$N$	engine speed
$\dot{Q}_{comb}$	rate of heat release during combustion	$N_{cyls}$	cylinder number
$\dot{Q}$	total heat release during the combustion	$p_{cyl}$	cylinder pressure
$q_{ht}$	rate of the convective heat transfer	$p_{max}$	maximal cycle pressure
$\dot{Q}_{in}, \dot{Q}_{out}$	inlet and outlet enthalpy flows	$\bar{p}_{cyl}$	average value of the pressure in the cylinder
$l$	connecting rod length	$R$	gas constant
$L$	piston stroke		

\* Corresponding author. e-mail: acer.msn@hotmail.fr.

$\bar{T}_{cyl}$	average value of the temperature in the cylinder
$t_{norm}$	normalized time vary between 0 and 1
$\Delta t_{comb}$	combustion duration
$\Delta \theta_{comb}$	combustion duration
$t_{inj}, \theta_{inj}$	injection time and angle
$t, \theta$	actual time and angle
$t$	time measured with respect to TDC
$U$	internal energy
$V_{cyl}$	in-cylinder gas volume
$V_{clear}$	clearance volume
$V_d$	displacement volume
$W$	external work

### Greeks

$\omega$	engine speed
$\lambda$	specific heat ratio
$\alpha_p$	coefficient shape of the piston head
$\alpha_{ch}$	coefficient shape of the cylinder head
$\tau_{id}$	ignition delay
$\beta_{mb}$	ratio of connected rod length to crank radius
$\phi$	fuel-air equivalence ratio

## 1. Introduction

More than one century after its invention by Dr. Rudolf Diesel, the compression ignition engine remains the most efficient internal combustion engine for ground vehicle applications. Thermodynamic models (zero-dimensional) and dimensional models (uni-dimensional and multi-dimensional) are the two types of models that have been used in internal combustion engine simulation modelling. Nowadays, trends in combustion engine simulations are towards the development of comprehensive dimensional models that accurately describe the performance of engines at a very high level of details. However, these models need a precise experimental input and a substantial computational power, which make the process significantly complicated and time-consuming [1]. On the other hand, the zero-dimensional model, which is mainly based on energy conservation (first law of thermodynamics), is used in the present work due to its simplicity and its being less time-consuming in the program execution, and to its relatively accurate results. The zero-dimensional model gives a satisfactory combustion heat, which determines the main thermodynamic parameters. The objective of the present study focuses only on the external performance of the engine (brake power and effective efficiency). The multi-dimensional method is intended particularly for the evaluation of the internal engine performance such as internal combustion and, therefore, the emission of pollutants [2]. There are many modelling approaches to analysis and optimize of the internal combustion engine. Angulo-Brown *et al.* [1] optimized the power of the Otto and Diesel engines with friction loss and finite duration cycle. Chen *et al.* [2] derived the relationships of correlation between net power output and the efficiency

for Diesel and Otto cycles; there are thermal losses only on the transformations in contact with the sources and the heat sinks other than isentropic. Chen *et al.* [2] proposed a model for which the thermal loss is represented more classically in the form of a thermal conductance between the mean temperature of gases, on each transformation = constant, compared to the wall temperature. Among the objectives of the present work is to conduct a comparative study of simulation results of the performances of a six cylinder direct injection turbo-charged compression ignition engine obtained with the elaborate calculation code in FORTRAN and those with the software GT-Power. We also studied the influence of certain important thermodynamic and geometric engine parameters on the brake power, on the effective efficiency, and also on pressure and temperature of the gases in the combustion chamber.

## 2. Diesel Engine Modelling

There are three essential steps in the mathematical modelling of internal combustion engine [3, 4]: (1) Thermodynamic models based on first and second law analysis, they are used since 1950 to help engine design or turbocharger matching and to enhance engine processes understanding; (2) Empirical models based on input-output relations introduced in early 1970s for primary control investigation; (3) Nonlinear models physically-based for both engine simulation and control design. Engine modelling for control tasks involves researchers from different fields, mainly control and physics. As a consequence, several specific nominations may designate the same class of model in accordance with the framework. To avoid any misunderstanding, we classify models within three categories with terminology adapted to each field:

- *Thermodynamic-based models or knowledge* models (so-called white box) for nonlinear model physically-based suitable for control.
- *Non-thermodynamic models* or "black-box" models for experimental input-output models.
- *Semiphysical approximate models* or parametric models (so-called "grey-box"). It is an intermediate category; here, models are built with equations derived from physical laws of which parameters (masses, volume, inertia, etc.) are measured or estimated using identification techniques.

Next section focuses on category 1 with greater interest on thermodynamic models. For the second and third class of models, see [5].

### 2.1. Thermodynamic Based Engine Model

Thermodynamic modeling techniques can be divided, in order of complexity, into the following groups [5]: (a) quasi-stable (b) filling and emptying and (c) the method of characteristics (gas dynamic models). Models that can be adapted to meet one or more requirements for the development of control systems are: quasi-steady, filling and emptying, cylinder-to-cylinder (CCEM) and mean value models (MVEM). Basic classification of thermodynamic models and the emergence of appropriate models for control are shown in Figure 1:

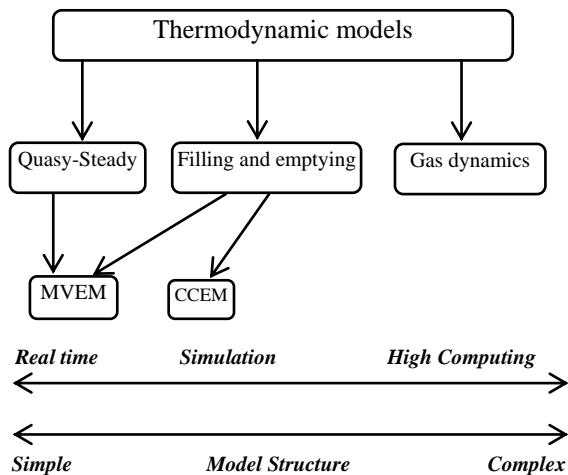


Figure 1. Basic classification of thermodynamic models of internal combustion engines

### 2.1.1. Quasi-Steady Method

The quasi-steady model includes crankshaft and the turbocharger dynamics and empirical relations representing the engine thermodynamic [6]. Quasi-steady models are simple and have the advantage of short run times. For this reason, they are suitable for real-time simulation. Among the disadvantages of this model were the strong dependence of the experimental data and the low accuracy. Thus, the quasi-steady method is used in the combustion subsystem with mean value engine models to reduce computing time.

### 2.1.2. Filling and Emptying Method

Under the filling and emptying concept, the engine is treated as a series of interconnected control volumes (open thermodynamic volume) [7, 8]. Energy and mass conservation equations are applied to every open system with the assumption of uniform state of gas. The main motivation for filling and emptying technique is to give general engine models with the minimum requirement of empirical data (maps of turbine and compressor supplied by the manufacturer). In this way, the model can be adapted to other types of engines with minimal effort. The filling and emptying model shows a good prediction of the engine performance under steady state and transient conditions and provides information about parameters known to affect pollutant or noise. However, assumptions of uniform state of gas cover up complex acoustic phenomena (resonance).

### 2.1.3. Method of Characteristics (or Gas Dynamic Models)

It is a very powerful method to accurately access parameters such as the equivalence ratio or the contribution to the overall noise sound level of the intake and the exhaust manifold. Its advantage is to effectively understand the mechanism of the phenomena that happen in a manifold [9] and to allow to accurately obtain laws of evolution of pressure, speed and temperature manifolds at any point, depending on the time, but the characteristic method requires a much more important calculation

program, and the program's complexity increases widely with the number of singularities to be treated.

## 3. General Equation of the Model

In the present work, we developed a zero-dimensional model based on that proposed by [8], that gives a satisfactory combustion heat and determines the main thermodynamic parameters. The assumptions that have been made in developing the in-cylinder model for the direct injection diesel engine are:

1. Engine plenums (cylinders, intake and exhaust manifolds) are modelled as separate thermodynamic systems containing gases at uniform state.
2. The pressure, temperature and composition of the cylinder charge are uniform at each time step, which is to say that no distinction is made between burned and unburned gas during the combustion phase inside the cylinder.
3. There is no gas leakage through the valves and piston rings so that the mass remains constant.
4. The heat transfer region is limited by the cylinder head, the bottom surface of the piston and the instantaneous cylinder wall.
5. From the results of Semin *et al.* [10], the temperature of the surfaces mentioned above is constant during the cycle.
6. The rate of heat transfer of gases to the wall is calculated from the temperature of the combustion gases and the wall. Heat transfer through the gas to the wall changes rapidly due to the motion of the gas during piston motion and the geometry of the combustion chamber. The correlation from Hohenberg is used to calculate the rate of heat transfer of the cylinder.
7. With respect to the filling-and-emptying method, mass, temperature and pressure of gas are calculated using first law and mass conservation.
8. Ideal gases with constant specific heats, effects of heat transfer through intake and exhaust manifolds are neglected.
9. Compressor inlet and turbocharger outlet temperatures and pressures are assumed to be equal to ambient pressure and temperature.
10. The crank speed is uniform (steady-state engine). The rate of change of the volume with respect to time is given as follows, Figure 2:

$$V_{cyl}(t) = V_{clear} + \frac{\pi D^2 L}{4} \left( 1 + \beta_{mb} (1 - \cos(\omega t)) - \sqrt{1 - \beta_{mb}^2 \sin^2(\omega t)} \right) \quad (1)$$

$t$  is the time corresponding to crank angle measured with respect to the top dead center (s),  $\omega$  is the engine speed (rad/s),  $V_{clear}$  is the clearance volume ( $V_{clear} = V_{cyl}(t) / c_r$ ),  $c_r$  is the compression ratio,  $\beta_{mb} = 2l / L$  is the ratio of connected rod length to crank radius,  $l$  is the connecting rod length (m),  $L$  is the piston stroke [m] and  $D$  is the cylinder bore (m).

The piston speed  $v_{pis}$  (m/s) is equal to:

$$v_{pis} = \frac{4}{\pi D^2} \left. \frac{dV_{cyl}(t)}{dt} \right|_r \quad (2)$$

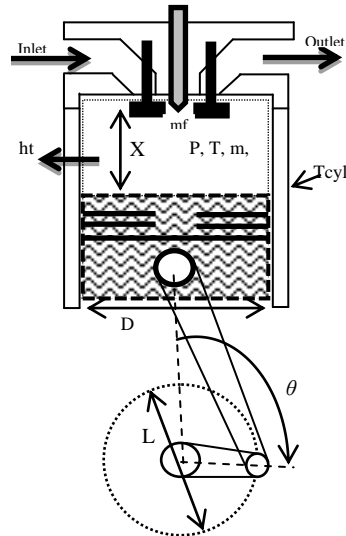


**Figure 2.** Cylinder scheme and its variables (p: pressure; T: temperature; m: mass and V: volume)

### 3.1. Mass Entering the Cylinder

The conservation equation of the mass applied to the cylinder is :

$$\frac{dm_{cyl}}{dt} = \dot{m}_f + \dot{m}_{in} - \dot{m}_{out} \quad (3)$$

### 3.2. Ideal Gas

The ideal gas model gives the relationship between the mass  $m_{cyl}$  in the cylinder, the volume  $V_{cyl}$ , the pressure  $P_{cyl}$  and temperature  $T_{cyl}$  [11]:

$$\frac{dT_{cyl}}{dt} = \frac{1}{m_{cyl} C_v} \left( \frac{dQ}{dt} - P_{cyl} \frac{dV_{cyl}}{dt} \right) \quad (4)$$

From equations (3) and (4), we obtain the following final state equation for cylinder pressure:

$$\frac{dp_{cyl}}{dt} = \frac{\gamma}{V_{cyl}} \left[ RT_{in} \dot{m}_{in} - RT_{cyl} \dot{m}_{out} - p_{cyl} \dot{V}_{cyl} \right] + \frac{\gamma-1}{V_{cyl}} \left[ \dot{m}_{bf} Q_{LHV} - \dot{Q}_{ht} \right] \quad (5)$$

$\lambda$  is the specific heat ratio ( $\lambda = C_p / C_v$ )

### 3.3. Equations of Heat Transfer, Combustion and Friction Losses

#### 3.3.1. Heat Exchange Correlation

Heat transfer at cylinder walls are represented by the Woschni correlation modified by Hohenberg [12], with the ideal gas, the instantaneous convective heat transfer rate from the in-cylinder gas to cylinder wall  $\dot{Q}_{ht}$  is calculated by [7]:

$$\frac{dQ_{ht}}{dt} = A_{cyl} h_t (T_{cyl} - T_{wall}) \quad (6)$$

$T_{wall}$  is the temperature walls of the combustion chamber (bounded by the cylinder head, piston head and the cylinder liner). From the results of Rakopoulos *et al.* [13],  $T_{wall}$  is assumed constant.

The heat transfer coefficient  $h_t$  in [kW/K.m<sup>2</sup>] at a given piston position. After numerical tests, it was found that the results obtained with the application of Hohenberg correlation are similar to those obtained with the GT-Power software. So according to Hohenberg's correlation, the heat transfer coefficient [12] is:

$$h_t(t) = k_{hoh} p_{cyl}^{0.8} V_{cyl}^{-0.06} T_{cyl}^{-0.4} (v_{pis} + 1.4)^{0.8} \quad (7)$$

$p_{cyl}$  is the cylinder pressure,  $V_{cyl}$  the in cylinder gas volume at each crank angle position and  $k_{hoh}$  is Hohenberg's constant that characterises the engine, ( $k_{hoh} = 130$ ).

#### 3.3.2. Combustion Model

In the present paper, we chose the single-zone combustion model proposed by Watson *et al.* [4]. This model reproduces in two combustion phases, the first is the faster combustion process (premixed combustion) and the second is the diffusion combustion which is slower and represents the main combustion phase. During the

combustion phase, but the term  $\dot{Q}_{comb}$  is equal to zero apart from this phase. So the amount of heat release  $\dot{Q}_{comb}$  is assumed proportional to the burned fuel mass:

$$\frac{dQ_{comb}}{dt} = \frac{dm_{fb}}{dt} h_{for} \quad (8)$$

$$\frac{dm_{fb}}{dt} = \frac{dm_{fb}^*}{dt} \frac{m_f}{\Delta t_{comb}} \quad (9)$$

The combustion process is described using an empirical model, the single-zone model obtained by Watson *et al.* [4]:

$$\frac{dm_{fb}^*}{dt} = \beta \left( \frac{dm_{fb}}{dt} \right)_p + (1-\beta) \left( \frac{dm_{fb}}{dt} \right)_d \quad (10)$$

$\frac{dQ_{comb}}{dt}$  is the rate of heat release during combustion [kJ/s],  $\frac{dm_{fb}}{dt}$  is the burned fuel mass rate [kg/s],  $h_{for}$  the

enthalpy of formation of the fuel [kJ/kg],  $\frac{d\dot{m}_{fb}}{dt}$  is the

normalized burned fuel mass rate,  $m_f$  is the fuel mass injected per cycle [kg/cycle],  $\left( \frac{dm_{fb}}{dt} \right)_p$  is the normalized

fuel burning rate in the premixed combustion,

$\left( \frac{dm_{fb}}{dt} \right)_d$  is the normalized fuel burning rate in the

diffusion combustion, and  $\beta$  the fraction of the fuel

injected into the cylinder and participated in the premixed combustion phase.

### 3.3.3. Friction Losses

The friction losses do not only affect the performance, but they also increase the size of the cooling system, and they often represent a good criterion for the engine design. So the friction mean effective pressure is calculated by [2]:

$$fmep = C + (0.005 p_{max}) + 0.162 v_{pis} \quad (11)$$

$P_{max}$  is the maximal cycle pressure [bar], for direct injection diesel engine  $C = 0.130$  bar.

To evaluate the differential equation (4) or (5), all terms of the right side must be found. The most adapted numerical solution method for these equations is the Runge-Kutta method.

### 3.4. Effective Power and Effective Efficiency

The effective power  $b_{power}$  for 4-stroke engine is [14]:

$$b_{power} = bmep V_d N_{cyls} N / 2 \quad (12)$$

$V_d$  is the displacement volume [m<sup>3</sup>],  
 $V_d = \pi D^2 S / 4$ ,  $N_{cyls}$  is the cylinder number.

The effective efficiency  $Reff$  is given by [15]:

$$R_{eff} = Wd / Q_{comb} \quad (13)$$

$Q_{comb}$  is the heat release during combustion [kJ].

## 4. Simulation Programs of Supercharged Diesel Engines

### 4.1. Computing Steps of the Developed Simulation Program

The calculation of the thermodynamic cycle according to the basic equations mentioned above requires an algorithm for solving the differential equations for a large number of equations describing the initial and boundary conditions, the kinematics of the crank mechanism, the engine geometry, the fuel and kinetic data. It is therefore wise to choose a modular form of the computer program. The developed power cycle simulation program includes a main program as an organizational routine, but which incorporates a few technical calculations, and also several subroutines. The computer program calculates in discrete crank angle incremental steps from the start of the compression, combustion and expansion stroke.

The program configuration allows through subroutines to improve the clarity and the flexibility of the program. The basis of any power cycle simulation is above all the knowledge of the combustion process. This can be described using the modified Wiebe function including parameters such as the combustion time and the fraction of the fuel injected into the cylinder. For the closed cycle period, Watson *et al.* recommended the following engine calculation crank angle steps: 10°CA before ignition, 1°CA

at fuel injection timing, 2°CA between ignition and combustion end, and finally 10°CA for expansion [16].

The computer simulation program includes the following parts:

#### • Input engine, turbocharger and intercooler data

Engine geometry ( $D, S, l, r$ ), Engine constant ( $N, \phi, C_r$ ), Turbocharger constant ( $\pi^c, \pi^t, p_{amb}, m, T_{amb}, P_{out,tur}, T_{out,tur}, P_{out,man}, T_{out,man}^{ICE}$ ) and polynomial coefficient of thermodynamic properties of species.

#### • Calculation of intercooler and turbocharger thermodynamic parameters

Compressor outlet pressure  $P_c$ , compressor outlet temperature  $T_c$ , compressor outlet masse flow rate  $\dot{m}_c$ , intercooler outlet pressure  $P_{ic}$ , intercooler outlet temperature  $T_{ic}$ , intercooler outlet masse flow rate  $\dot{m}_{ic}$ , turbine outlet pressure  $P_t$ , turbine outlet temperature  $T_t$ , turbine outlet masse flow rate  $\dot{m}_t$ .

#### • Calculation of engine performance parameters

1. Calculation of the initial thermodynamic data (calorific value of the mixture, state variables to close the inlet valve, compression ratio  $C_r$ ).
2. Calculation of the piston kinematic and heat transfer areas.
3. Main program for calculating the thermodynamic cycle parameters of compression, combustion and expansion stroke.
4. Numerical solution of the differential equation (the first law of thermodynamics) with the Runge-Kutta method.
5. Calculation of the specific heat (specific heat constant pressure  $C_p$  and specific heat at constant volume  $C_v$ ).
6. Calculation of the combustion heat, the heat through walls and the gas inside and outside the open system.
7. Calculation of main engine performance parameters mentioned above.

#### • Output of Data block

Instantaneous cylinder pressure  $P_{cyl}$ , instantaneous cylinder temperature  $T_{cyl}$ , indicated mean effective pressure  $imep$ , friction mean effective pressure  $fmep$ , mean effective pressure  $bmep$ , indicated power  $ipower$ , friction power  $fpower$ , brake power  $bpower$ .

The computer simulation steps of a turbocharged diesel engine are shown in the flowchart in Figure 3. For more details of the theoretical parts, see [16]

### 4.2. Simulation with the GT-Power Software

The GT-Power is a powerful tool for the simulation of internal combustion engines for vehicles, and systems of energy production. Among its advantages is the facility of use and modeling. GT-Power is designed for steady state

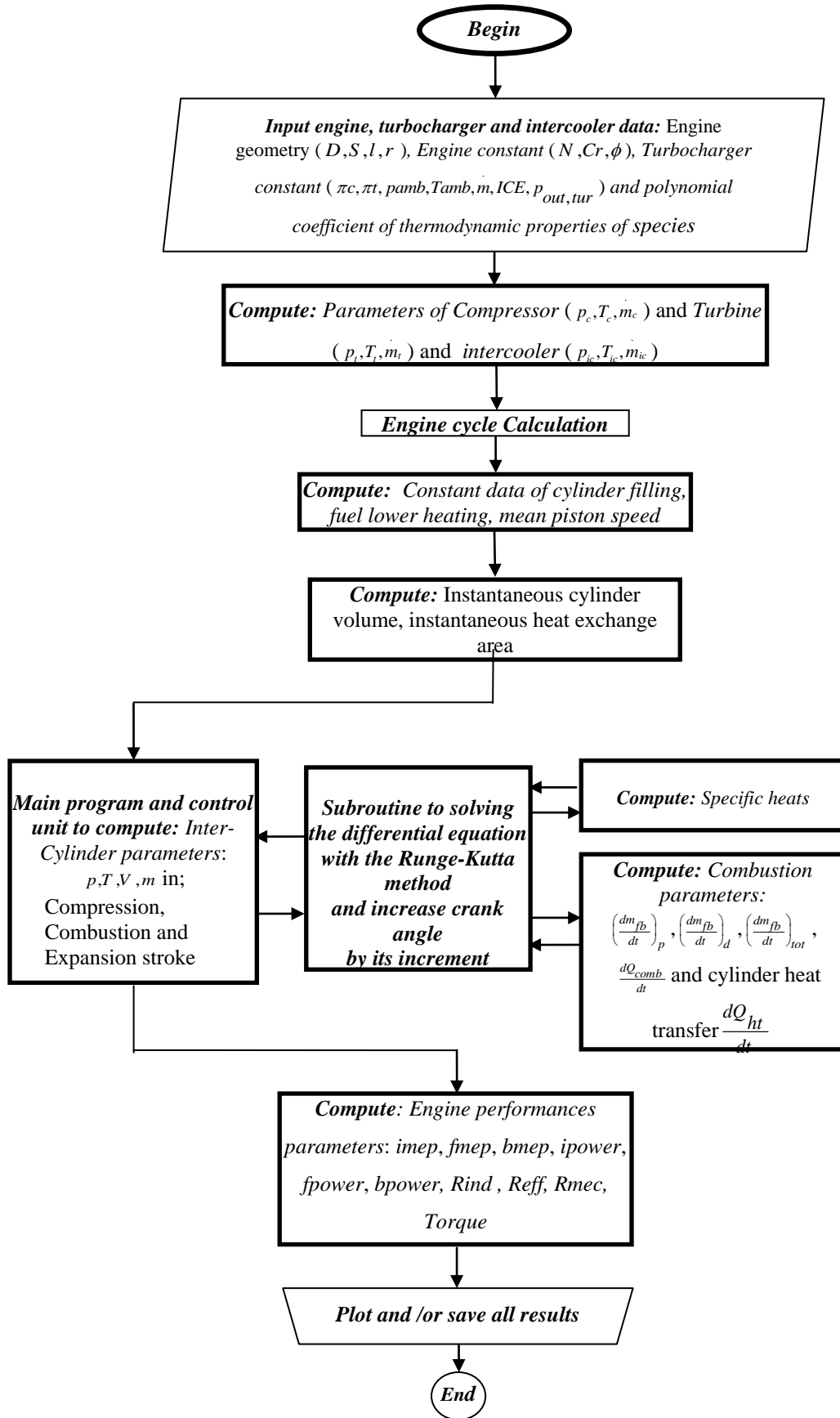


Figure 3. Schematic Flowchart of the developed computer simulation program

and transient simulation and analysis of the power control of the engine. The diesel engine combustion can be modeled using two functions Wiebe [17]. GT-Power is an object-based code, including template library for engine components (pipes, cylinders, crankshaft, compressors, valves, etc.). Figure 4 shows the model of a turbocharged diesel engine with 6 cylinders and intercooler made with GT-Power. In the modelling technique, the engine, turbocharger, intercooler, fuel injection system, intake and exhaust system are considered as components interconnected in series. In the intake manifold, the thermal transfers are negligible in the gas-wall interface; this hypothesis is acceptable since the collector's temperature is near to the one of the gases that it contains. The variation of the mass in the intake manifold depends on the compressor mass flow and the flow through of valves when they are open. In the

modeling view, the line of exhaust manifold of the engine is composed in three volumes; the cylinders are grouped by three and emerge on two independent manifold, component two thermodynamic systems opened of identical volumes, and a third volume smaller assures the junction with the wheel of the turbine. The turbocharger consists of an axial compressor linked with a turbine by a shaft; the compressor is powered by the turbine which is driven by exhaust gas. So more air can be added into the cylinders allowing for increasing the amount of the fuel to be burned, compared to a naturally aspirated engine [18]. The heat exchanger can be assimilated to an intermediate volume between the compressor and the intake manifold; it solves a system of differential equations supplementary identical to the manifold. It appeared to assimilate the heat exchanger as a non-dimensional organ.

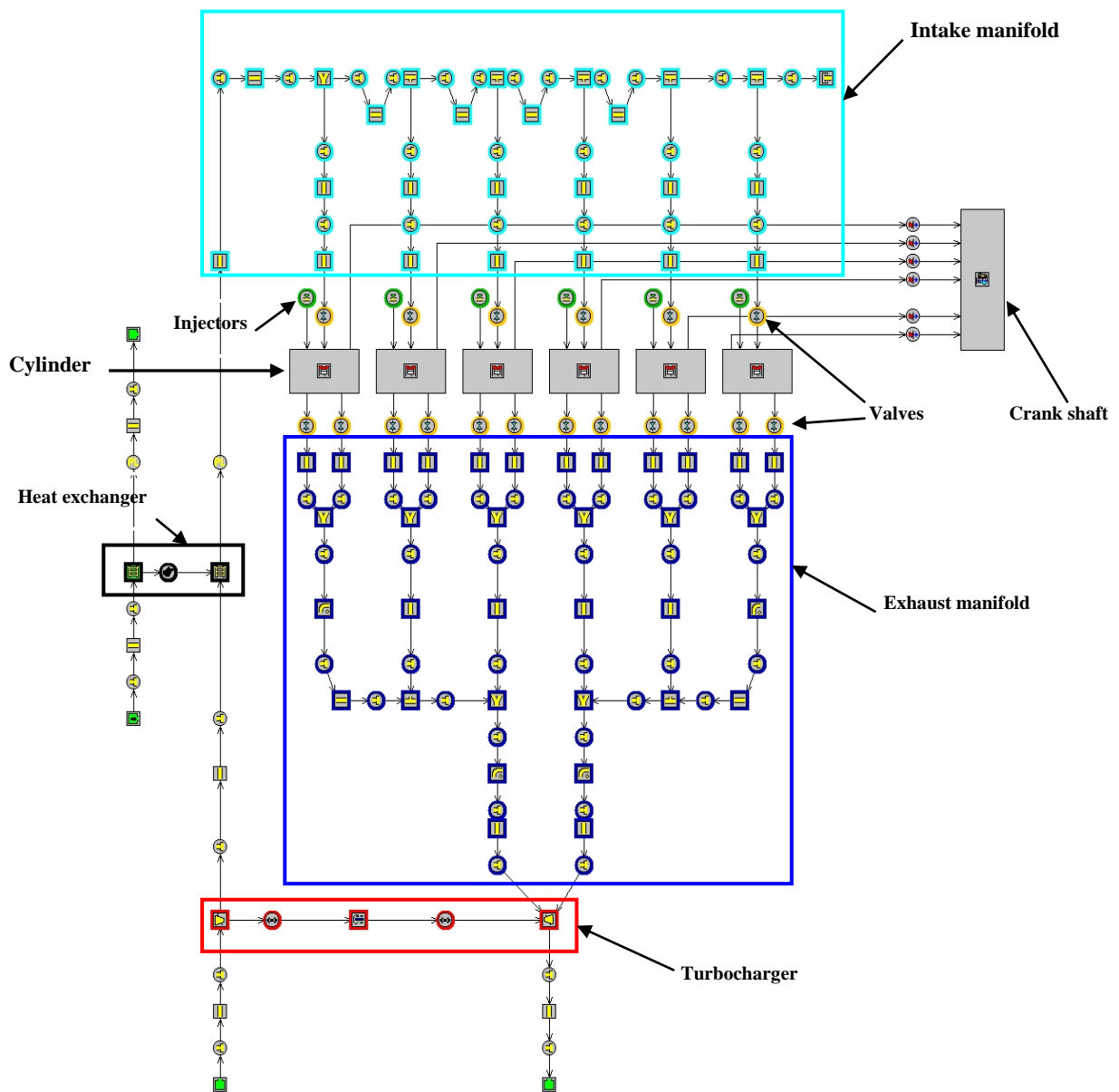


Figure 4. Developed model of the 6-cylinders turbocharged engine using the GT-Power software

**Table 1.** Injection system parameters [17]

Injectors parameters	Values
Injection pressure, (bar)	1000
Start of injection bTDC, (°CA)	15°BTDC
Number of holes per nozzle, (-)	8
Nozzle hole diameter, (mm)	0.25

## 5. Results of Engine Simulation

Thermodynamic and geometric parameters chosen in the present study are:

- *Engine geometry:* compression ratio  $C_r$ , cylinder bore  $D$  and more particularly the stroke-bore ratio  $R_{sb} = \frac{L}{D}$ .
- *Combustion parameters:* injected fuel mass  $m_f$ , crankshaft angle marking the injection timing  $T_{inj}$ , and cylinder wall temperature  $T_{wall}$ .

The following table (Table 2) shows the main parameters of the chosen direct-injection diesel engine [16, 17]:

**Table 2.** Engine specifications [17]

Engine parameters	Values
Bore, D (mm)	120.0
Stroke, S (mm)	175.0
Displacement volume, $V_d$ (cm <sup>3</sup> )	1978.2
Connecting rod length, l (mm)	300.0
Compression ratio, (-)	16.0
Inlet valve diameter, (mm)	60
Exhaust valve diameter, (mm)	38
Inlet Valve Open IVO, (°CA)	314
Inlet Valve Close IVC, (°CA)	-118
Exhaust Valve Open EVO, (°CA)	100
Exhaust Valve Close EVC, (°CA)	400
Injection timing, (°CA)	15° BTDC
Fuel system, (-)	Direct injection
Firing order, (-)	1-5-3-6-2-4

The combination of two curves (brake power versus engine speed and effective efficiency versus engine speed) allows the creation of a third one: the brake power function of the effective efficiency, as shown in Figure 5. The latter highlights two privileged operating points for the engine: a mode of maximum efficiency and another one of maximum power for the same conditions.

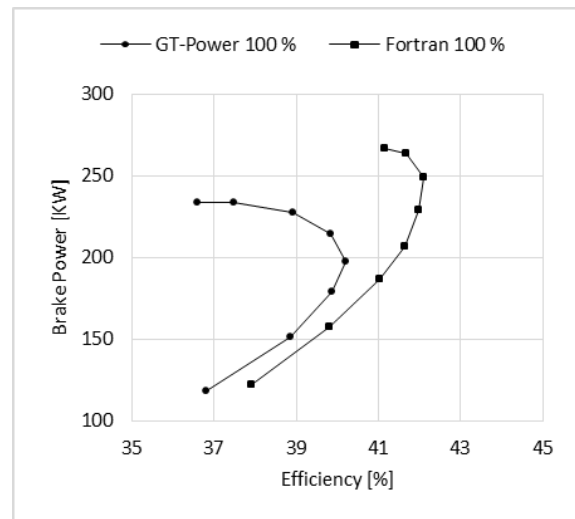


**Figure 5.** Brake power versus effective efficiency for full load,  $T_{inj} = 15^\circ$  bTDC,  $D_{cyl} = 120$  mm,  $C_r = 16:1$ ,  $T_{wall} = 450$  K,  $R_{sb} = 1.5$

### 5.1. Influence of the Geometric Parameters

#### 5.1.1. Influence of the Compression Ratio

In general, increasing the compression ratio improved the performance of the engine [16]. Figure 6 shows the influence of the compression ratio ( $C_r = 16:1$  and  $19:1$ ) on the brake power and effective efficiency at full load, advance for GT-Power and the elaborate software as shown in Figure 7. The brake efficiency increases with the increase of the effective power until its maximum value; it, afterwards, begins to decrease until a maximal value of the effective power. It is also valid for the effective power. For engine speed of 1600 rpm, if the compression ratio increases from 16:1 to 19:1, the maximal efficiency increases at 2% and the maximal power at 1.5% for GT-Power and the elaborate software. The gap between the results obtained with the two programs (FORTRAN and GT-Power) is due to the combustion models used. For the compression ratio  $Cr = 19:1$ , the average deviation does not exceed 9% for the effective power and efficiency.

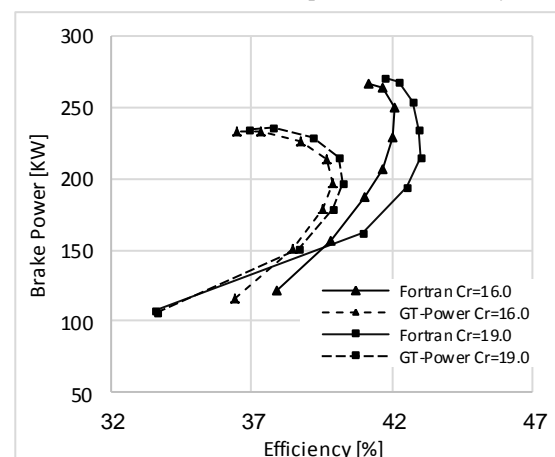


**Figure 6.** Compression ratio influence at 100% load,  $T_{inj} = 15^\circ$  bTDC,  $D_{cyl} = 120$  mm,  $T_{wall} = 450$  °K,  $R_{sb} = 1.5$

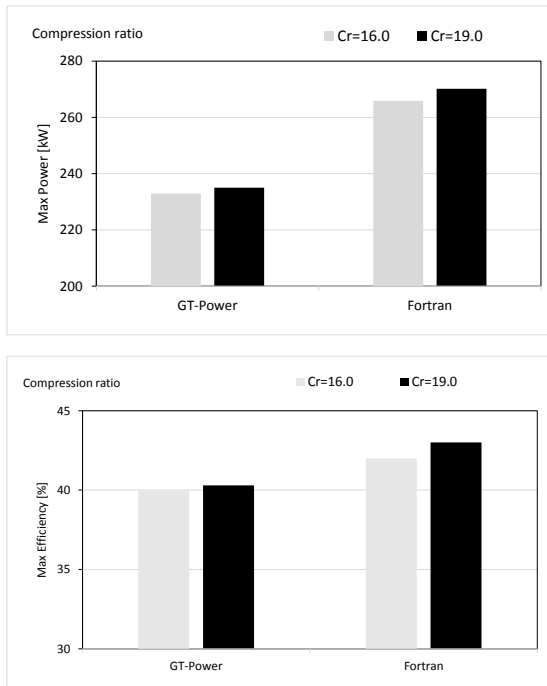


Figure 7. Maximum power and maximum efficiency for different compression ratio.

5.1.2. Influence of the Cylinder Diameter

Figure 8 shows the influence of the cylinder diameter on the effective power at full load 100%, a compression ratio of 16:1 and advance injection of 15° bTDC. The brake efficiency increases with the increase of the effective power until its maximum value, after which it begins to decrease until a maximal value of the effective power. If the cylinder diameter increases by 10 mm (from 130 to 140 mm), the brake efficiency decreases by 2 % and the effective power by 9%.

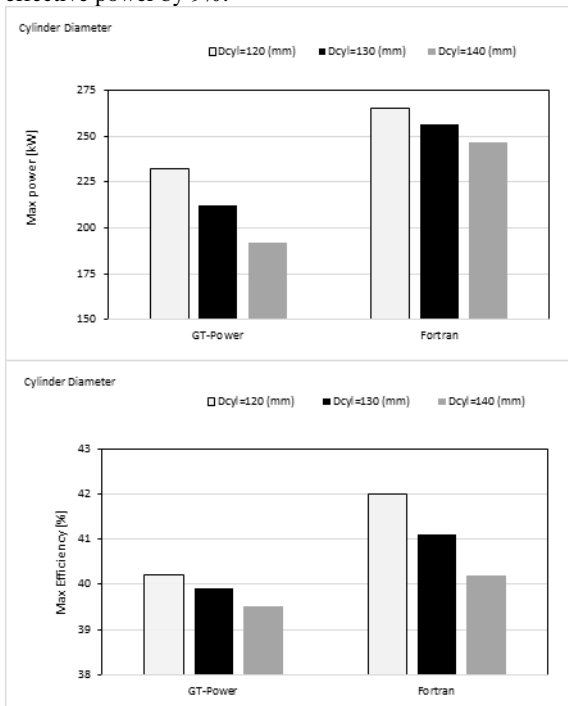


Figure 8. Maximum power and maximum efficiency for different cylinder diameter,  $D_{cyl} = 120, 130$  and  $140$  mm

5.1.3. Influence of the Stroke-Bore Ratio

The stroke-bore ratio is another geometric parameter that influences the performances of a turbocharged diesel engine. The cylinder volume of  $2.0$  l can be obtained in a different manner while varying this parameter; its influence is shown in Figure 9. If the stroke-bore ratio increases, the mean piston speed is greater, and friction losses (Eq.11) need to be considered while increasing the engine speed (Figure 10). The effective power and the brake efficiency decrease with an increase in the stroke-bore ratio. While the stroke-bore ratio increased from 1.5 to 2, the maximum brake efficiency decreased by an average of 3%, and the maximum effective power by 4%

For a stroke-bore ratio  $R_{sb} = 1.0$ , the average difference between the results with two programs is 9% for the effective power and 7% for the effective efficiency at full load.

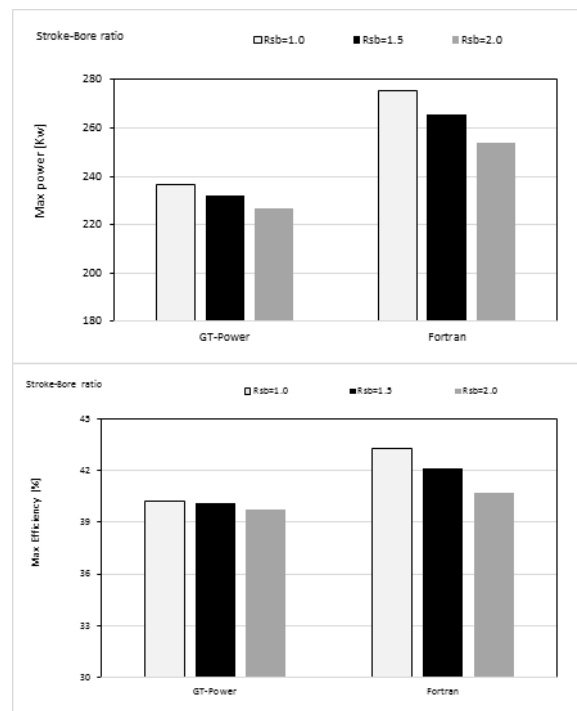


Figure 9. Maximum power and maximum efficiency for different stroke bore ratio,  $R_{sb} = 1.0, 1.5$  and  $2.0$

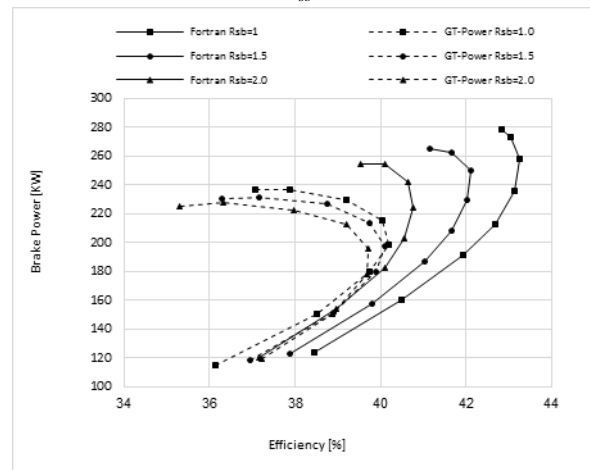


Figure 10. Influence of Stroke bore ratio for 100% load,  $T_{inj} = 15^\circ$  bTDC,  $v_{cyl} = 2.0$  l,  $C_r = 16:1$ ,  $T_{wall} = 450$  K

## 5.2. Influence of the Thermodynamic Parameters

### 5.2.1. Influence of the Wall Temperature

The influence of the cylinder wall temperature is represented in Figures 11 and 12. When the cylinder wall temperature is lower, the brake efficiency improves. From Figure 12, we note that the less the temperature deviation between gas and wall cylinder becomes, the higher the losses by convective exchange become [13]. By increasing the cylinder wall temperature from 350 K to 450 K, the maximum of brake power and effective efficiency decrease, respectively, by about 1%. The maximal operating engine temperature is limited by mechanical, thermal and design constraints. Increasing the temperature of the cylinder walls leads to a reduction in the engine performance. Therefore, it is advantageous to improve the cooling of the hot parts of the engine.

It is observed that with the increase of the engine rotation speed, gaps of the results obtained from both programs become larger. These are due to the pressure losses in the intake pipes and in the inlet of the turbocharger. In the developed program, these losses were expressed by a lower and constant pressure loss coefficient. For this reason, the effective power and efficiency calculated with the developed program are greater than those with GT-Power. At a cylinder wall temperature  $T_{wall} = 550$  K, the average differences between the two programs are in the order of 8% for effective power and efficiency.

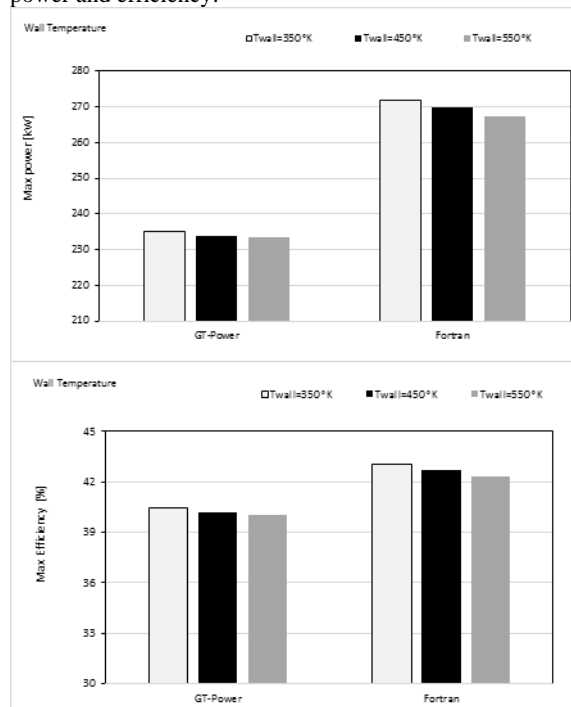


**Figure 11.** Maximum power and maximum efficiency for different cylinder wall temperature

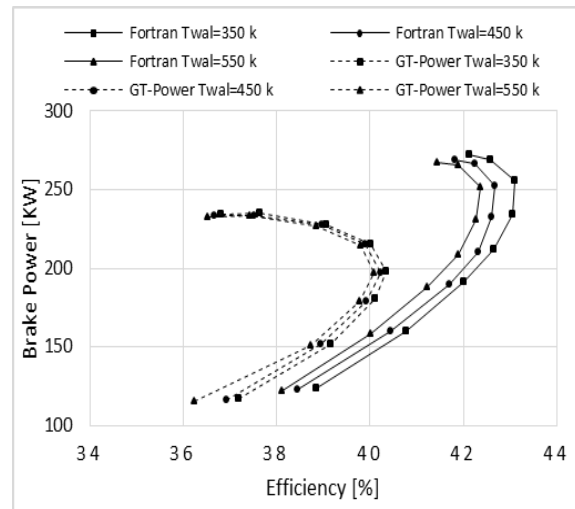


**Figure 12.** Wall temperature influence for 100% load,  $T_{inj} = 15^\circ$  bTDC,  $D_{cyl} = 120$  mm,  $C_r = 16:1$ ,  $R_{sb} = 1.5$

### 5.2.2. Influence of the Advanced Injection

Figure 13 shows the influence of different injection timings on the variation of the maximum brake power versus the maximum effective efficiency for both softwares: Fortran and GT-Power. This parameter has a substantial influence on the brake power and less on the effective efficiency. An injection advance from 5aTDC to  $15^\circ$  before TDC increased the heat flow from fluid to the combustion chamber wall. For an injection timing  $T_{inj} = 15^\circ$  bTDC, the mean gaps between both programs are about 7% for the effective power and effective efficiency.

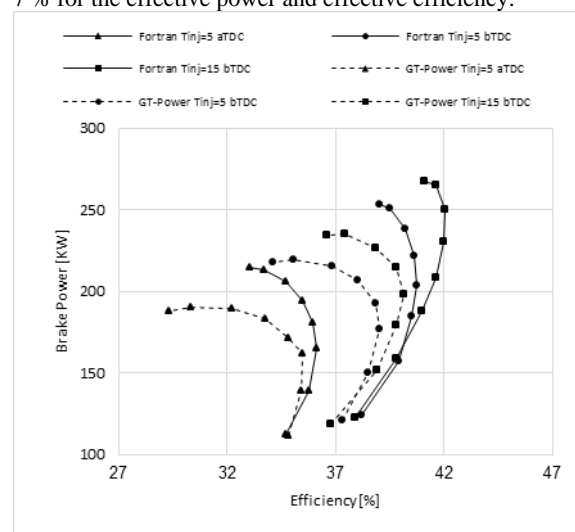


**Figure 13.** Injection timing influence for 100% load,  $D_{cyl} = 120$  mm,  $C_r = 16:1$ ,  $T_{wall} = 450$  K,  $R_{sb} = 1.5$

Figure 14 presents the influence of the injection timing and its impact on the form of the thermodynamic cycle of the pressure and temperature in the cylinder. When the injection starts at  $15^\circ$  before TDC the maximal pressure and temperature are higher, and the temperature at the

exhaust is lower than the case if the injection timing occurs at 5° after the TDC [19, 20]. In this case, the combustion begins whereas the piston starts its descent, the duration of heat exchange losses is lower, and then the exhaust temperature is higher.

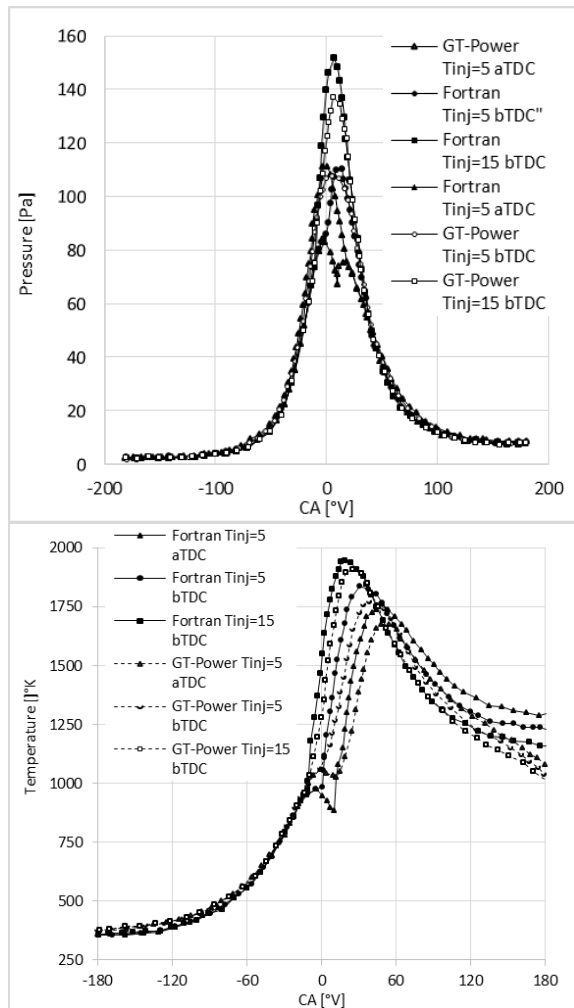


**Figure 14.** Injection timing influence on gas pressure and temperature versus crankshaft for 100% load,  $D_{cyl} = 120$  mm,  $C_r = 16:1$ ,  $T_{wall} = 450$  K,  $R_{sb} = 1.5$ ,  $N = 1400$  rpm

### 5.2.3. Influence of the Masse Fuel Injected

Figures 15 and 16 show the variation of the brake power versus the effective efficiency for different masse fuel injected at advance injection of 15°bTDC, compression ratio of 16:1, and  $N = 1400$  RPM. This parameter has a strong influence on the brake power, heat flux and it has a less influence on the effective efficiency. The brake power and effective efficiency increases with increasing the quantity of the fuel injected. At full load, the average differences of the results obtained with both programs used are 7% for the effective power and 5% for the effective efficiency. With an increase of the mass of the fuel injected of 50%, there is an improvement of the effective efficiency of 3.5% and the brake power of 29% and the heat flux of 15%. This clearly shows the importance of the variation of the quantity of the injected fuel in achieving the effective power and the brake efficiency.

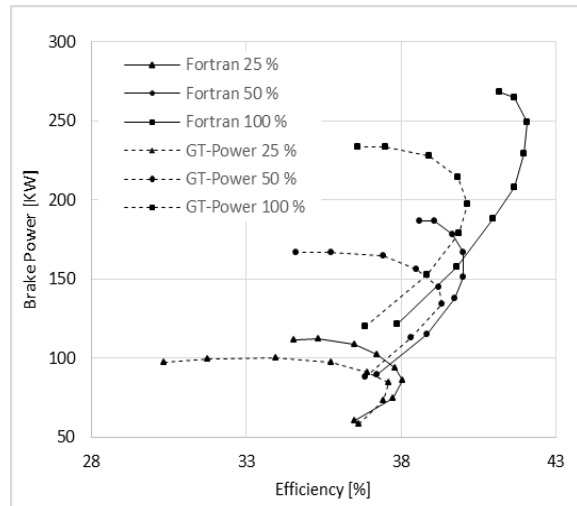


**Figure 15.** Mass fuel injected influence for  $T_{inj} = 15^\circ$  bTDC,  $D_{cyl} = 120$  mm,  $C_r = 16:1$ ,  $T_{wall} = 480$  K

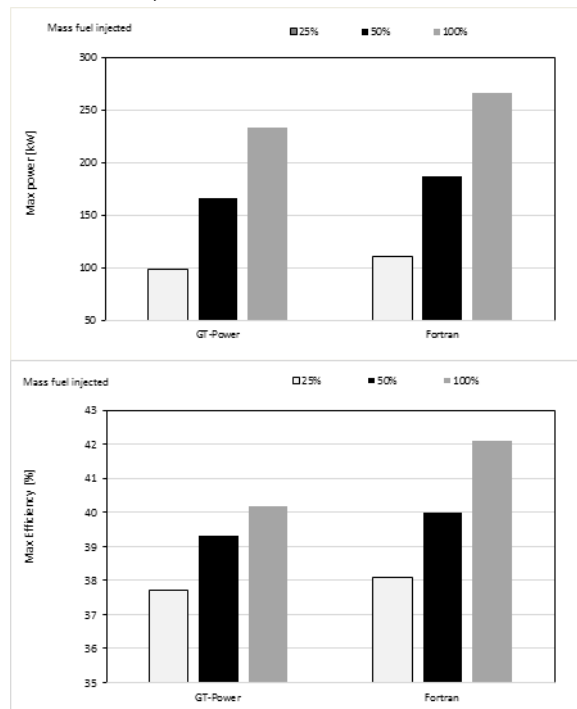


**Figure 16.** Maximum power and maximum efficiency for different mass fuel injected; 25%, 50% and 100%

## 6. Conclusion

The present study describes a turbocharged direct injection compression ignition engine simulator. A great effort was put into building a physical model based on the filling-and-emptying method. The resulting model can predict the engine performances. From the thermodynamic model, we are able to develop an interrelationship between the brake power and the effective efficiency that is related to the corresponding speed for different parameters studied; it results in an existence of a maximum power corresponding to a state for an engine optimal speed and a maximum economy and corresponding optimal speed.

We studied the influence of a certain number of parameters on engine power and efficiency: Parameters,

like stroke-bore ratio and the cylinder wall temperature, have a small influence on the brake power and effective efficiency and heat flux. While the angle of start injection, mass fuel injected, compression ratio have a great influence on the brake power, effective efficiency and heat flux. The engine simulation model, described in the present work, is valid for a quasi-steady state. The developed numerical simulation model was validated with the GT-Power Program by applying of data of a typical turbocharged diesel engine. This model is valid for other diesel engines of a similar configuration respecting the simplifying assumptions. It is quite evident that the GT-Power computer program gives quantitatively different results compared to developed simulation programs. However, under a qualitative aspect, the obtained results with both programs provide a good agreement.

Reducing toxic gas emissions is one of the major design criteria for internal combustion engines. For the prediction of the internal engine performance, it is necessary to use an appropriate multi-dimensional model. In the future work, we will try to focus on the validation of the multi-dimensional model for the prediction of internal and external performance of a turbocharged diesel engine. We will take into account the real pressure losses in the intake pipe, the evacuation process of burned gas, the mixture preparation according to combustion chamber form, the combustion model and the cooling of the cylinder-cylinder head assembly.

## References

- [1] F. Angulo-Brown, J. Fernandez-Betanzos and C.A. Diaz-Pico, "Compression ratio of an optimized Otto-cycle model". *European journal of physics*. Vol. 15 (1994), 38–42.
- [2] L. Chen, J. Lin, J. Lou, F. Sun and C. Wu, "Friction effect on the characteristic performances of Diesel engines". *International Journal of Energy Research*. Vol. 26 (2002), 965–971.
- [3] A. Merabet, M. Feidt and A. Bouchoucha, "Effet du transfert de chaleur sur les performances d'un moteur a combustion interne atmosphérique fonctionnant suivant un cycle mixte". *Termotehnica*. Vol. 2 (2002), 43–46.
- [4] N. Watson, A.D. Pilley and M. Marzouk, "A combustion correlation for diesel engine simulation". In: *SAE Technical Paper* (1980), 1980-800029.
- [5] M. Tarawneh, F. Al-Ghathian, M. A. Nawafleh and N. Al-Kloub. "Numerical Simulation and Performance Evaluation of Stirling Engine Cycle". *Jordan Journal of Mechanical and Industrial Engineering*. Vol.4 (2010), 5, 615-628.
- [6] L. Guzzella and A. Amstutz, "Control of diesel engines". *IEEE Transaction on Control Systems*. Vol. 18 (1998), 53–71.
- [7] Heywood JB. *Internal Combustion Engine Fundamentals*. McGraw-Hill, New York ; 1988.
- [8] Ledger JD and Walmsley S. Computer simulation of a turbocharged diesel engine operating under transient load conditions. *SAE Technical Paper* 1971, 710177.
- [9] Benson RS and Baruah PC. Some further tests on a computer program to simulate internal combustion engine. *SAE Technical Paper* 1973, 730667.
- [10] Winterborne DE, Thiruarooran C and Wellstead PE. A wholly dynamical model of a turbocharged diesel engine for transfer function evaluation. *SAE Technical Paper*, 1977; 770124.
- [11] A. Sakhrieha and E. Abu-Nada, "Computational Thermodynamic Analysis of Compression Ignition Engine". *International Communications in Heat and Mass Transfer*. Vol. 37 (2010), 299–303.
- [12] Hohenberg GF. Advanced approaches for heat transfer calculations. *SAE Technical Paper*. 1979, 1979-790825.
- [13] C.D. Rakopoulos, C.D. Rakopoulos, G.C. Mavropoulos and E.G. Giakoumis, "Experimental and theoretical study of the short-term response temperature transients in the cylinder walls of a diesel engine at various operating conditions". *Applied Thermal Engineering*. Vol. 2 (2004), 679-702.
- [14] R.B. Semin and R. Ismail, "Investigation of Diesel Engine Performance Based on Simulation". *American Journal of Applied Sciences*. Vol. 5 (2008), 610-617.
- [15] J.E. Dec, "Advanced compression ignition engines-understanding the in-cylinder processes". *Proc. Combust. Inst*. Vol. 32 (2009), 2727–2742.
- [16] B. Menacer and M. Bouchetara, "simulation and prediction of the performance of a direct turbocharged diesel engine". *Simulation: Transactions of the Society for Modeling and Simulation International*. Vol. 89 (2013) No. 11, 1355–1368.
- [17] Gamma Technologies, *GT-Power User's Manual*, GT-Suite Version 7.0, 2009.
- [18] J. Galindo, F.J. Arnau, A. Tiseira and P. Piqueras, "Solution of the Turbocompressor Boundary Condition for One-Dimensional Gas-Dynamic Codes". *Mathematical and Computer Modelling*. Vol. 52 (2010), 1288-1297.
- [19] M. Feidt and D. Descieux, "Modelling of a Spark Ignition Engine for Power-Heat Production Optimization". *Oil & Gas Science and Technology – Revue. IFP Energies nouvelles*. Vol. 5 (2011), 737-745.
- [20] R. Ebrahimi, "Performance of an Irreversible Diesel Cycle under Variable Stroke Length and Compression Ratio". *Journal of Ambient Science*. Vol. 7 (2009), 58-64.

# Numerical Simulation and Nonlinear Stability Analysis of Francis Hydraulic Turbine-Seal System

Qianqian Wu<sup>a</sup>, Leike Zhang<sup>b\*</sup> and Zhenyue Ma<sup>a</sup>

<sup>a</sup>Faculty of Infrastructure Engineering, School of Hydraulic Engineering, Dalian University of Technology, Dalian, China.

<sup>b</sup>College of Water Resources Science and Engineering, Taiyuan University of Technology, Taiyuan, China.

Received 28 Dec 2014

Accepted 22 Sep 2015

## Abstract

Hydraulic and electromagnetic forces are main causes of vibrations in a hydraulic generating set. The Unbalanced Magnetic Pull (UMP) and nonlinear sealing force can produce large oscillations which will be dangerous to the shaft system. In the present paper, the kinetic model of a simplified unit shaft system, which mainly considers 6 degrees of freedom of rotor and turbine, under UMP, and Muszynska nonlinear sealing force is established. On this basis, the nonlinear stability of Francis turbine-seal system is emphasized, and the effect of the seal parameters on system stability is also discussed, according to the Lyapunov first approximation theory. The results show that there is very little likelihood of rub-impact phenomenon occurrence between the turbine and seal structure with nonlinear sealing force, if no other external interferences are taken into account. In addition, some suggestions about reducing self-excited vibration by parameters sensitivity analysis are given, which can be beneficial to the safety operation and vibration fault diagnosis for the units.

© 2015 Jordan Journal of Mechanical and Industrial Engineering. All rights reserved

**Keywords:** Hydroelectric Generating Set; Sealing Force; Turbine-Seal System; Critical Instable Speed.

## 1. Introduction

The hydraulic generating set is a typical hydro-mechanical-electrical coupling system; meanwhile, as the key equipment of hydropower plant, it is also the important guarantee of economic and social benefits produced from hydro-connection project eventually. With the rapid development of manufacturing and processing technology, the hydraulic generating set is moving in the direction to large-scale, high-speed and high-power. At the same time, the unit vibration phenomenon has been increasingly prominent that the corresponding stability problem, which is one of the hottest research area in the field of hydropower industry, is concerned extensively by engineering and academic circles.

The hydraulic generating set is mainly affected by hydraulic, mechanical and electromagnetic vibration sources. The mechanical vibration sources, such as mass unbalance, misalignment and bearing's looseness, are widely present in rotary machinery, and related studies have been relatively mature [1]. In contrast, it is difficult to grasp the effect of the hydraulic and electromagnetic vibration sources on the dynamic characteristics of unit,

due to their complexity and uncertainty. In particular, the interactive relationship between the hydraulic vibration source and the turbine; in spite of numerous works done, its influence in the shaft system, cannot be accurately mastered.

The unequal clearance of turbine seal belongs to one of the hydraulic vibration sources. The sealing structure is used to control fluid leakage in turbine with the features including complex device, small clearance as well as the large pressure between front and back device. When the periodic eccentric movement of unit occurs due to some reasons, the pressure pulsations will appear generating the sealing force which has an influence on the stability of the unit. The 8-parameters model [2] was employed for analyzing the rotor-seal structure in the past; however, it is difficult to reflect the nonlinear characteristics of sealing force. The nonlinear model proposed by Muszynska and Bently [3-5] has the milestone meaning. Although the form is simple, it can well embody the effect of rotor disturbance on the movement stiffness, damping and inertia. Meanwhile, the

\* Corresponding author. e-mail: lkzhang@hotmail.com.

nonlinear characteristics of sealing force can be reflected with the confirmation by experiment. This model has currently become the most widely used sealing model.

UMP is the manifestation of electromagnetic vibration source. When the generator runs normally, the rotor rotates in a uniform magnetic field, and the magnetic pull applied on rotor radial points is also uniform. However, the UMP will act on the rotor if the gap between the stator and rotor is not equal, the rotor has eccentricity or the initial deflection of shaft appears [6]. Currently, there are two ways for the complete expression derivation of UMP, the first one is using air-gap potential and permeability to obtain the flux density  $B(a,t)$ , then getting the unit area radial magnetic force of rotor surface or stator inner surface according to the formula  $\sigma = \frac{B^2}{2\mu_0}$ ; here,  $\sigma$  is stress,  $\mu_0$  is air permeance,

finally the expression can be achieved through integration [7-10]. The second one is taking direct derivative of  $x$  and  $y$  displacement according to air-gap magnetic field energy [11-13].

Although there are many studies on sealing force [14-19] and UMP [20-24] on the dynamics of unit; however, most discussions were contributed to the effect of a single vibration source on the system responses, and the stability analyses were insufficient.

In the present paper, the nonlinear dynamical model of shaft system for hydroelectric generating set under both UMP and sealing force is established. On this basis, the dynamic characteristics and stability with different sealing parameters for turbine-seal system are numerically analyzed and compared with other studies. Some different conclusions are also obtained according to the numerical calculation results.

## 2. Dynamic Model of System

### 2.1. Shaft System

The hydroelectric generating set system model consists of upper, lower, water guide bearings, rotor as

$$T = \frac{1}{2} m_1 (\dot{x}_1^2 + \dot{y}_1^2 + e_1^2 \dot{\phi}_1^2 + 2e_1 \dot{\phi}_1 \dot{y}_1 \cos \phi_1 - 2e_1 \dot{\phi}_1 \dot{x}_1 \sin \phi_1) + \frac{1}{2} (J_1 + m_1 e_1^2) \dot{\phi}_1^2 + \frac{1}{2} m_2 (\dot{x}_2^2 + \dot{y}_2^2 + e_2^2 \dot{\phi}_2^2 + 2e_2 \dot{\phi}_2 \dot{y}_2 \cos \phi_2 - 2e_2 \dot{\phi}_2 \dot{x}_2 \sin \phi_2) + \frac{1}{2} (J_2 + m_2 e_2^2) \dot{\phi}_2^2 \tag{1}$$

where  $m_1, e_1, \phi_1 = \omega t, J_1$  are the mass, eccentricity, rotating angle and rotary inertia of rotor, respectively;  $m_2, e_2, \phi_2 = \omega t$  and  $J_2$  are the mass, eccentricity, rotating angle and rotary inertia of turbine, respectively;  $\omega$  is rotating speed,  $(x_1, y_1), (x_2, y_2)$  are the centre coordinates of rotor and turbine, respectively.

In Figure 1,  $B_1, O_1, B_2, B_3$  and  $O_2$  are the geometric centres of upper guide bearing, rotor, lower guide bearing, turbine and water guide bearing, respectively. Denote  $|B_1 O_1|=a, |O_1 B_2|=b, |B_2 B_3|=c,$  and  $|B_3 O_2|=d, r_1$  and  $r_2$  are the radial displacement of rotor and turbine, respectively; then  $r_1 = \sqrt{x_1^2 + y_1^2}, r_2 = \sqrt{x_2^2 + y_2^2}$ . According to the geometrical relationship, expressions of  $r_3, r_4$  and  $r_5$  can be obtained as:

well as turbine components, as seen in Figure 1. Due to the complex vibration characteristics of system under UMP and sealing force, only the lateral vibration of the unit is considered, while the effect of thrust bearing and shaft on the system is ignored.

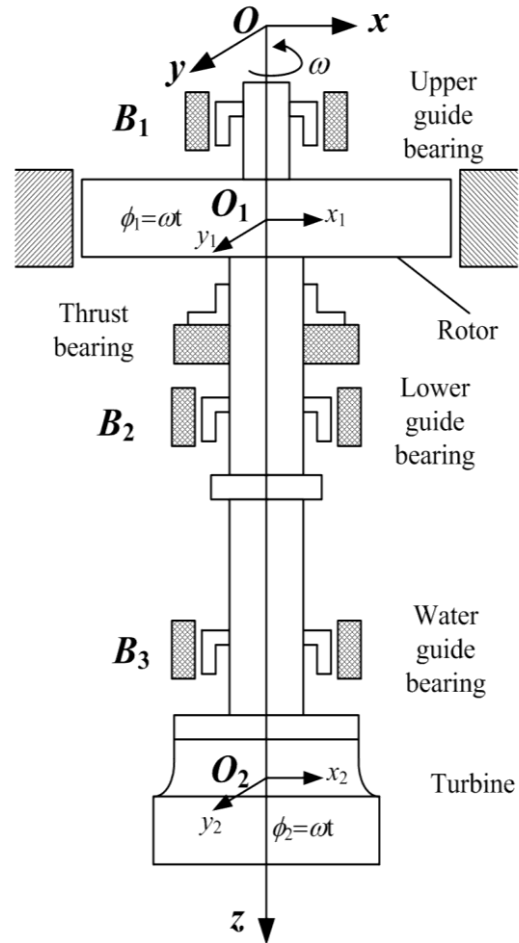


Figure 1 Shaft system of hydroelectric generating unit

The total kinetic energy of the system includes that from generator and that from turbine, namely

$$r_3 = \frac{[(a+b)(b+c+d) - a(c+d)] \cdot r_1 - ab \cdot r_2}{b(b+c+d)} = \frac{A_1 \cdot r_1 - A_2 \cdot r_2}{B} \tag{2}$$

$$r_4 = \frac{(c+d) \cdot r_1 + b \cdot r_2}{b+c+d}$$

$$r_5 = \frac{d \cdot r_1 + (b+c) \cdot r_2}{b+c+d}$$

where  $A_1 = (a+b)(b+c+d), A_2 = ab, B = b(b+c+d)$ .

Without a consideration of the change of gravitational potential energy, assuming that each guide bearing's stiffness including the upper one  $k_1$ , lower one  $k_2$  and water one  $k_3$ , is isotropic, then the elastic potential energy of system can be expressed as follows:

Without a consideration of the change of gravitational potential energy, assuming that each guide bearing's stiffness including the upper one  $k_1$ , lower one  $k_2$  and water one  $k_3$ , is isotropic, then the elastic potential energy of system can be expressed as follows:

$$\begin{aligned}
 U &= \frac{1}{2}(k_1 r_3^2 + k_2 r_4^2 + k_3 r_5^2) \\
 &= \left[ \frac{A_1^2}{B^2} k_1 + \frac{(c+d)^2}{(b+c+d)^2} k_2 + \frac{d^2}{(b+c+d)^2} k_3 \right] \frac{x_1^2 + y_1^2}{2} + \left[ \frac{A_2^2}{B^2} k_1 + \frac{b^2}{(b+c+d)^2} k_2 + \frac{(b+c)^2}{(b+c+d)^2} k_3 \right] \frac{x_2^2 + y_2^2}{2} + \\
 &\left[ -\frac{A_1 A_2}{B^2} k_1 + \frac{b(c+d)}{(b+c+d)^2} k_2 + \frac{d(b+c)}{(b+c+d)^2} k_3 \right] \sqrt{x_1^2 + y_1^2} \sqrt{x_2^2 + y_2^2}
 \end{aligned} \quad (3)$$

It is proposed that the various damping of system is linear, existing in the direction of  $x_1$ ,  $y_1$ ,  $x_2$  and  $y_2$ , considering the UMP acted on rotor and sealing force acted on turbine, the generalized force can be written as follows:

$$\begin{cases}
 Q_{x_1} = -c_1 \dot{x}_1 + F_{x\_ump} \\
 Q_{y_1} = -c_1 \dot{y}_1 + F_{y\_ump} \\
 Q_{x_2} = -c_2 \dot{x}_2 + F_{x\_seal} \\
 Q_{y_2} = -c_2 \dot{y}_2 + F_{y\_seal}
 \end{cases} \quad (4)$$

where  $c_1$  and  $c_2$  are the damping coefficient of rotor and turbine, respectively;  $F_{ump}$  and  $F_{seal}$  are the UMP and nonlinear sealing force, respectively, whose  $x$  and  $y$  direction components are as follows:

$$\begin{bmatrix} F_{x\_ump} \\ F_{y\_ump} \end{bmatrix} = \frac{R_r L_r \pi k_f^2 I_j^2}{4\mu_0} (2\Lambda_0 \Lambda_1 + \Lambda_1 \Lambda_2 + \Lambda_2 \Lambda_3) \begin{bmatrix} \cos \gamma \\ \sin \gamma \end{bmatrix} \quad (5)$$

$$\begin{bmatrix} F_{x\_seal} \\ F_{y\_seal} \end{bmatrix} = - \begin{bmatrix} K - m_f \tau_f^2 \omega^2 & \tau_f \omega D \\ -\tau_f \omega D & K - m_f \tau_f^2 \omega^2 \end{bmatrix} \begin{bmatrix} x \\ y \end{bmatrix} - \begin{bmatrix} D & 2\tau_f m_f \omega \\ -2\tau_f m_f \omega & D \end{bmatrix} \begin{bmatrix} \dot{x} \\ \dot{y} \end{bmatrix} - \begin{bmatrix} m_f & \\ & m_f \end{bmatrix} \begin{bmatrix} \ddot{x} \\ \ddot{y} \end{bmatrix} \quad (6)$$

$$\begin{cases}
 m_1 \ddot{x}_1 + c_1 \dot{x}_1 + \left[ \frac{A_1^2}{B^2} k_1 + \frac{(c+d)^2}{(b+c+d)^2} k_2 + \frac{d^2}{(b+c+d)^2} k_3 \right] x_1 + \left[ -\frac{A_1 A_2}{B^2} k_1 + \frac{b(c+d)}{(b+c+d)^2} k_2 + \frac{d(b+c)}{(b+c+d)^2} k_3 \right] \frac{\sqrt{x_2^2 + y_2^2}}{\sqrt{x_1^2 + y_1^2}} x_1 = \\
 m_1 e_1 \omega^2 \cos \phi + F_{x\_ump} \\
 m_1 \ddot{y}_1 + c_1 \dot{y}_1 + \left[ \frac{A_1^2}{B^2} k_1 + \frac{(c+d)^2}{(b+c+d)^2} k_2 + \frac{d^2}{(b+c+d)^2} k_3 \right] y_1 + \left[ -\frac{A_1 A_2}{B^2} k_1 + \frac{b(c+d)}{(b+c+d)^2} k_2 + \frac{d(b+c)}{(b+c+d)^2} k_3 \right] \frac{\sqrt{x_2^2 + y_2^2}}{\sqrt{x_1^2 + y_1^2}} y_1 = \\
 m_1 e_1 \omega^2 \sin \phi + F_{y\_ump} \\
 m_2 \ddot{x}_2 + c_2 \dot{x}_2 + \left[ \frac{A_2^2}{B^2} k_1 + \frac{b^2}{(b+c+d)^2} k_2 + \frac{(b+c)^2}{(b+c+d)^2} k_3 \right] x_2 + \left[ -\frac{A_1 A_2}{B^2} k_1 + \frac{b(c+d)}{(b+c+d)^2} k_2 + \frac{d(b+c)}{(b+c+d)^2} k_3 \right] \frac{\sqrt{x_1^2 + y_1^2}}{\sqrt{x_2^2 + y_2^2}} x_2 = \\
 m_2 e_2 \omega^2 \cos \phi + F_{x\_seal} \\
 m_2 \ddot{y}_2 + c_2 \dot{y}_2 + \left[ \frac{A_2^2}{B^2} k_1 + \frac{b^2}{(b+c+d)^2} k_2 + \frac{(b+c)^2}{(b+c+d)^2} k_3 \right] y_2 + \left[ -\frac{A_1 A_2}{B^2} k_1 + \frac{b(c+d)}{(b+c+d)^2} k_2 + \frac{d(b+c)}{(b+c+d)^2} k_3 \right] \frac{\sqrt{x_1^2 + y_1^2}}{\sqrt{x_2^2 + y_2^2}} y_2 = \\
 m_2 e_2 \omega^2 \sin \phi + F_{y\_seal}
 \end{cases} \quad (8)$$

For the convenience of calculation, we assume that  $|B_1 O_1| = |O_1 B_2| = |B_3 O_2| = |B_2 B_3|/2$ , and equation (8) can be rewritten as:

In equation (5),  $I_j$  is the excitation current,  $k_f$  is the coefficient of fundamental magnetomotive force,  $R_r$  is the radius of rotor,  $L_r$  is the length of rotor,  $\Lambda_n$  ( $n=0, 1, 2, \dots$ ) are the Fourier coefficients,  $\gamma$  is the rotary angle of rotor. The formula derivation can be found in reference [9].

In equation (6),  $K$ ,  $D$ ,  $m_f$ , respectively, stands for equivalent stiffness, damping and mass of sealing force.  $K$ ,  $D$ ,  $\tau_f$  are nonlinear function of perturbation motion displacement  $X$  and  $Y$ , where:

$$K = K_0 (1 - e^2)^{-n}, \quad D = D_0 (1 - e^2)^{-n} \quad (7)$$

$$\tau_f = \tau_0 (1 - e)^b, \quad n = \frac{1}{2} \sim 3, \quad 0 < b < 1$$

More details about the above expressions can be seen in reference [4].

According to the lagrange function, the differential equations of the shaft system can be obtained:

$$\left\{ \begin{aligned} m_1 \ddot{x}_1 + c_1 \dot{x}_1 + \frac{1}{16} \left[ (25k_1 + 9k_2 + k_3) + (-5k_1 + 3k_2 + 3k_3) \frac{\sqrt{x_2^2 + y_2^2}}{\sqrt{x_1^2 + y_1^2}} \right] x_1 &= m_1 e_1 \omega^2 \cos \phi + F_{x\_ump} \\ m_1 \ddot{y}_1 + c_1 \dot{y}_1 + \frac{1}{16} \left[ (25k_1 + 9k_2 + k_3) + (-5k_1 + 3k_2 + 3k_3) \frac{\sqrt{x_2^2 + y_2^2}}{\sqrt{x_1^2 + y_1^2}} \right] y_1 &= m_1 e_1 \omega^2 \sin \phi + F_{y\_ump} \\ m_2 \ddot{x}_2 + c_2 \dot{x}_2 + \frac{1}{16} \left[ (k_1 + k_2 + 9k_3) + (-5k_1 + 3k_2 + 3k_3) \frac{\sqrt{x_1^2 + y_1^2}}{\sqrt{x_2^2 + y_2^2}} \right] x_2 &= m_2 e_2 \omega^2 \cos \phi + F_{x\_seal} \\ m_2 \ddot{y}_2 + c_2 \dot{y}_2 + \frac{1}{16} \left[ (k_1 + k_2 + 9k_3) + (-5k_1 + 3k_2 + 3k_3) \frac{\sqrt{x_1^2 + y_1^2}}{\sqrt{x_2^2 + y_2^2}} \right] y_2 &= m_2 e_2 \omega^2 \sin \phi + F_{y\_seal} \end{aligned} \right. \tag{9}$$

Define  $T = \omega t$ ,  $X_1 = \frac{x_1}{\delta_0}$ ,  $Y_1 = \frac{y_1}{\delta_0}$ ,  $X_2 = \frac{x_2}{c_0}$ ,  $Y_2 = \frac{y_2}{c_0}$

where  $\delta_0$  is the mean air-gap length when the rotor is centered, then

$$\frac{d}{dt} = \omega \frac{d}{dT}, \quad \frac{d^2}{dt^2} = \omega^2 \frac{d^2}{dT^2}, \quad X' = \frac{dX}{dT}, \quad Y' = \frac{dY}{dT},$$

$$X'' = \frac{d^2 X}{dT^2}, \quad Y'' = \frac{d^2 Y}{dT^2}$$

After the dimensionless transformations, the state equation of (9) can be obtained:

$$\begin{pmatrix} X_1'' \\ Y_1'' \\ X_1' \\ Y_1' \\ X_2'' \\ Y_2'' \\ X_2' \\ Y_2' \end{pmatrix} = \begin{pmatrix} -\frac{c_1}{m_1 \omega} & 0 & -\frac{K_3}{m_1 \omega^2} & 0 \\ 0 & -\frac{c_1}{m_1 \omega} & 0 & -\frac{K_3}{m_1 \omega^2} \\ 1 & 0 & & \\ 0 & 1 & & \\ & & -D_1 & -D_2 & -K_1 & -K_2 \\ & & D_2 & -D_1 & K_2 & -K_1 \\ 1 & 0 & & & & \\ 0 & 1 & & & & \end{pmatrix} \begin{pmatrix} X_1' \\ Y_1' \\ X_1 \\ Y_1 \\ X_2' \\ Y_2' \\ X_2 \\ Y_2 \end{pmatrix} + \begin{pmatrix} \frac{e_1 \cos T}{\delta_0} + \frac{F_{x\_ump}}{m_1 \omega^2 \delta_0} \\ \frac{e_1 \sin T}{\delta_0} + \frac{F_{y\_ump}}{m_1 \omega^2 \delta_0} \\ 0 \\ 0 \\ \frac{m_2 e_2 \cos T}{c_0 M} \\ \frac{m_2 e_2 \sin T}{c_0 M} \\ 0 \\ 0 \end{pmatrix} \tag{10}$$

where

$$K_1 = \frac{K_4 + K - \tau_f^2 \omega^2 m_f}{M \omega^2}, \quad K_2 = \frac{\tau_f D}{M \omega}, \quad D_1 = \frac{c_2 + D}{M \omega},$$

$$D_2 = \frac{2\tau_f m_f}{M}, \quad M = m_2 + m_f,$$

$$K_3 = \frac{1}{16} \left[ (25k_1 + 9k_2 + k_3) + \frac{c_0}{\delta_0} (-5k_1 + 3k_2 + 3k_3) \frac{\sqrt{X_2^2 + Y_2^2}}{\sqrt{X_1^2 + Y_1^2}} \right]$$

$$K_4 = \frac{1}{16} \left[ (k_1 + k_2 + 9k_3) + \frac{\delta_0}{c_0} (-5k_1 + 3k_2 + 3k_3) \frac{\sqrt{X_1^2 + Y_1^2}}{\sqrt{X_2^2 + Y_2^2}} \right]$$

and  $c_0$  is seal clearance.

Order  $e_1=e_2=0$ , when the system (10) is balanced, the acceleration and rotating speed equal zero, namely  $X_1''=Y_1''=X_2''=Y_2''=X_1'=Y_1'=X_2'=Y_2'=0$ .

Substituting

$X_1''=Y_1''=X_2''=Y_2''=X_1'=Y_1'=X_2'=Y_2'=0$  into equation (10) yields:

$$\begin{cases} K_3 - \frac{F_{\_coeffi}}{\delta_0} \left( \frac{1}{2} + \frac{5}{8} (X_1^2 + Y_1^2) \right) = 0 \\ K_3 - \frac{F_{\_coeffi}}{\delta_0} \left( \frac{1}{2} + \frac{5}{8} (X_1^2 + Y_1^2) \right) = 0 \\ K_1 X_2 + K_2 Y_2 = 0 \\ K_2 X_2 - K_1 Y_2 = 0 \end{cases} \tag{11}$$

where  $F_{\_coeffi} = \frac{R_r L_r \pi \mu_0 k_j^2 I_j^2}{\delta_0^2}$  is the constant item

of UMP.

Making use of numerical algorithms, such as iterative method, can solve the complicated equations above. After getting the numerical solutions (the balance points  $(X_{10}, Y_{10}, X_{20}, Y_{20})$ ), substitute them into Jacobian matrix, then determine the stability of system according to the eigenvalues of Jacobian matrix.

However, it is observed that the first two equations in (11) are the same, which means that it is impossible to obtain the numerical results in the absence of other known conditions. Therefore, the determination whether the system is instable cannot be conducted.

Song and Ma [24] discussed the stability of rotor system for hydroelectric generating set considering the UMP. It was pointed out that the main reason behind the system instability can be attributed to the cross items of electromagnetic stiffness and nonlinear oil film force. Only the main diagonal items of UMP model, used in the present paper, are included, while the effect of cross ones is ignored. Hence, from the perspective of rotor model, the instability phenomenon will not happen. In addition, compared to the rotor structure, the turbine-seal system is affected by hydraulic loads, the performance is more complex and the instability condition is more obvious after the occurrence of the self-excited vibration. In light of this, the turbine-seal system is selected to analyze the instability characteristics under sealing force, instead of the whole shaft system in this paper.

2.2. Turbine-Seal Model

For the convenience of analysis and comparison, it is supposed that the turbine is single disc system with two ends simply-supported, and the quality is focused on the middle. The nonlinear sealing force, mainly producing in the gap between crown and head-cover, as well as the shaft seal, is equivalently acted on the disk, as seen in Figure 2, and then the system equation is as follows:

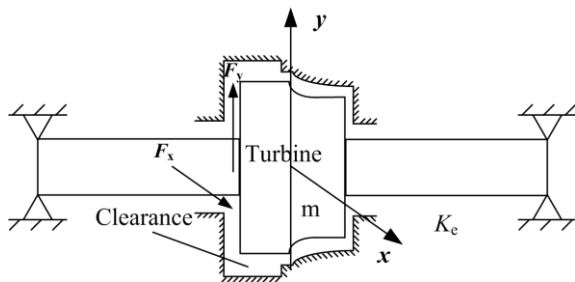


Figure 2 Model of turbine-seal system

$$\begin{bmatrix} m & 0 \\ 0 & m \end{bmatrix} \begin{Bmatrix} \ddot{X} \\ \ddot{Y} \end{Bmatrix} + \begin{bmatrix} D_e & 0 \\ 0 & D_e \end{bmatrix} \begin{Bmatrix} \dot{X} \\ \dot{Y} \end{Bmatrix} + \begin{bmatrix} K_e & 0 \\ 0 & K_e \end{bmatrix} \begin{Bmatrix} X \\ Y \end{Bmatrix} = \begin{Bmatrix} F_x \\ F_y \end{Bmatrix} + \begin{Bmatrix} 0 \\ -mg \end{Bmatrix} \quad (12)$$

where  $m$  is the mass of turbine,  $K_e$  is axis stiffness,  $D_e$  is turbine damping.  $F_x$  and  $F_y$  are the nonlinear sealing force. Substitute equation (6) into equation (12) and define:

$$x = \frac{X}{c_0}, y = \frac{Y}{c_0}, \tau = \omega t, \dot{x} = \frac{dx}{dT},$$

$$x' = \frac{dx}{d\tau} = \frac{1}{\omega} \frac{dx}{dt}, M = m + m_f$$

Then

$$\begin{bmatrix} 1 & 0 \\ 0 & 1 \end{bmatrix} \begin{Bmatrix} x'' \\ y'' \end{Bmatrix} + \begin{bmatrix} D_1 & D_2 \\ -D_2 & D_1 \end{bmatrix} \begin{Bmatrix} x' \\ y' \end{Bmatrix} + \begin{bmatrix} K_1 & K_2 \\ -K_2 & K_1 \end{bmatrix} \begin{Bmatrix} x \\ y \end{Bmatrix} = \begin{Bmatrix} 0 \\ G \end{Bmatrix} \quad (13)$$

where

$$K_1 = \frac{K_e + K - \tau_f^2 \omega^2 m_f}{M \omega^2}, K_2 = \frac{\tau_f D}{M \omega}, D_1 = \frac{D_e + D}{M \omega},$$

$$D_2 = \frac{2\tau_f m_f}{M}, G = -\frac{mg}{M c \omega^2}$$

2.3. Stability Analysis

Equation (13) can be rewritten as the state equation:

$$\begin{Bmatrix} x'' \\ y'' \\ x' \\ y' \end{Bmatrix} = \begin{bmatrix} -D_1 & -D_2 & -K_1 & -K_2 \\ D_2 & -D_1 & -K_2 & -K_1 \\ 1 & 0 & 0 & 0 \\ 0 & 1 & 0 & 0 \end{bmatrix} \begin{Bmatrix} x' \\ y' \\ x \\ y \end{Bmatrix} + \begin{Bmatrix} 0 \\ G \\ 0 \\ 0 \end{Bmatrix} = \begin{Bmatrix} f_1(x', y', x, y, \omega) \\ f_2(x', y', x, y, \omega) \\ f_3(x', y', x, y, \omega) \\ f_4(x', y', x, y, \omega) \end{Bmatrix} \quad (14)$$

When the system is balanced, substituting  $x'' = y'' = x' = y' = 0$  into equation (14) yields:

$$\begin{bmatrix} K_1 & K_2 \\ -K_2 & K_1 \end{bmatrix} \begin{Bmatrix} x \\ y \end{Bmatrix} = \begin{Bmatrix} 0 \\ G \end{Bmatrix} \quad (15)$$

The balance value  $(x_0, y_0)$ , which is related to  $\omega$ , can be solved through iteration method. Expand equation (14) as the first approximation at the balance point  $(x_0, y_0)$ , then yield Jacobian matrix. According to the Lyapunov first approximation theory, nonlinear system stability is determined with the eigenvalues nature of Jacobian matrix. If all of the eigenvalues have negative real part, the system is asymptotically stable. If a pair of eigenvalues with zero real part exist while others whose real parts are nonzero, the system is in a critical state. And the rotating speed calculated for this condition is called critical rotating speed  $\omega_c$ , at this time the system behaves as a pair of conjugate eigenvalues crossing the imaginary axis, losing stability at the balance point with the occurrence of Hopf bifurcation. The amplitude of turbine centre orbit increases as the rotating speed increases, and the impact phenomenon may happen between turbine and seal.

3. Numerical Simulation and Discussion

3.1. System Stability Analysis under Sealing Force

The parameters for linear and nonlinear runner-sealing are listed in Table 1 and Table 2, respectively. The first critical rotating speed of the system is  $\omega_n = \sqrt{\frac{K_e}{m}} = \sqrt{\frac{0.5 \times 10^{10}}{3 \times 10^5}} = 129 \text{ rad/s}$ . In the present paper, the trial and error method is adopted to obtain the critical instable rotating speed  $\omega_c = 240 \text{ rad/s}$  under nonlinear sealing force, with accuracy 1 rad/s. When  $\omega = \omega_c = 240 \text{ rad/s}$ , the balance position is  $(0.1137, -0.2467)$ , the eigenvalues =  $(0.0000 \pm 0.5407i, -0.2754 \pm 0.5219i)$ . When  $\omega = 200 \text{ rad/s}$ , the eigenvalues =  $(-0.0259 \pm 0.6395i, -0.3056 \pm 0.6157i)$ , all of them have negative real part, which signifies the stability of system, as depicted in Figure 4(a). When  $\omega = 300 \text{ rad/s}$ , the eigenvalues =  $(0.0243 \pm 0.4378i, -0.2405 \pm 0.4202i)$ , the

**Table 1.** Parameters of runner linear sealing system

$a_0$	$\rho$ (kg/m <sup>3</sup> )	$\lambda$	$\xi$	$m$ (t)	$R$ (m)	$l$ (m)	$v$ (m/s)	$c$ (mm)	$K_e$ (N/m)	$D_e$ (N.s/m)
1.0	1000	0.1	1.5	300	3.0	0.50	3.0	2.0	$0.5 \times 10^{10}$	$0.5 \times 10^5$

**Table 2.** Parameters of runner nonlinear sealing system

$b$	$n$	$n_0$	$m_0$	$\tau_0$	$\xi$	$m$ (t)	$R$ (m)	$l$ (m)	$v$ (m/s)	$c$ (mm)	$\Delta P$ (pa)	$K_e$ (N/m)	$D_e$ (N.s/m)
0.2	0.5	0.079	-0.25	0.5	1.5	300	3.0	0.50	3.0	2.0	$0.5 \times 10^6$	$0.5 \times 10^{10}$	$0.5 \times 10^5$

emergence of positive real part indicates that the system is instable at the balance point, as seen in Figure 4(b). With the further increase of  $\omega$  the orbit amplitude arises consecutively, being close to the seal clearance size, as shown in Figure 4 (c)-(d).

The critical instable speed  $\omega_{c1}$  under linear sealing force is 261 rad/s. It can be seen from Figure 5 that the system is stable and the orbit is approximated by a point when  $\omega = 200 \text{ rad/s} < \omega_{c1}$ . When  $\omega = 270 \text{ rad/s} > \omega_{c1}$ , the instability occurs as the orbit amplitude increases rapidly, which is obviously larger than the seal clearance. Hence, the rub-impact phenomenon between turbine and seal happens, causing a damage to the system.

In references [14 and 17], the mechanical models of turbine-seal system are established, with almost the same numerical parameters as adopted in the present paper. According to several turbine orbit trends with increasing rotating speed, instead of giving a further calculation verification, it was pointed out that when  $\omega$  increases to a certain extent, the rub-impact phenomenon will appear between the seal device and turbine for the system under nonlinear sealing force, due to the turbine amplitude exceeding seal clearance. However, the calculation results described in Figures 4(e)-(f) demonstrates that even if the rotating speed reaches such a high level like  $\omega = 800 \text{ rad/s}$  (in fact, it is out of question for hydraulic generating set to run at extra high speed), the amplitude is only close to the seal clearance rather than exceeding it.

Gustavsson and Aidanpää [25] took a practical unit in Sweden as an example, analyzing the nonlinear rub-impact dynamic behavior between the turbine and seal structure. It was indicated that the combined effects of turbine eccentricity and hydrodynamic pulsation was the main reason resulting in the rub-impact phenomenon, while the influence of the nonlinear sealing force was not mentioned.

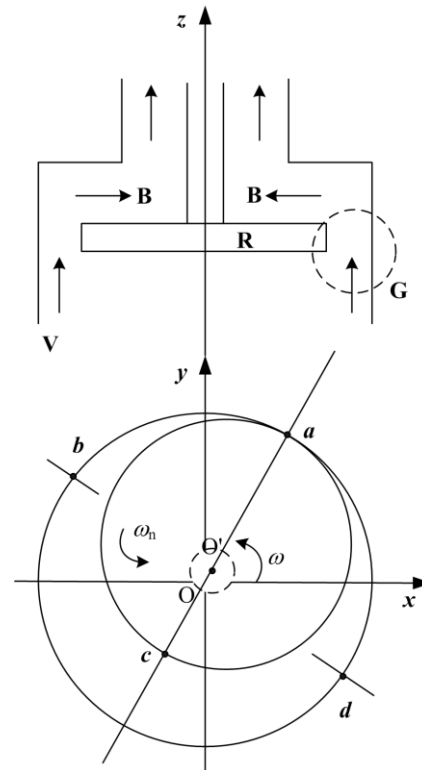
The parameters in linear sealing force are constant, which is different from that in nonlinear sealing force. After the former is acted on the turbine system, the common differential equation of rotor system under external force can be formed. If the values of parameters satisfy the requirement, the similar rub-impact condition between rotary and stationary parts, as described in reference [26], will appear.

In view of this, it is considered in the present paper that the rub-impact between the turbine and seal structure for turbine-seal system under nonlinear sealing force may not happen, due to the increase of the rotating speed, in the absence of other external interferences.

### 3.2. Influence of Seal Parameters in the Dynamic Characteristics of System

Keep other parameters unchanged, choose seal radius  $R$ , seal length  $L$ , axial velocity  $v$ , seal pressure dropping,

seal coefficients  $\tau_0$  and seal clearance  $c_0$  to discuss their effect on the critical instable speed, as shown in Figure 6.

**Figure 3.** Hydraulic turbine simplified model

With the increase of seal radius, seal length and seal pressure dropping, the system critical speed decreases first and then increases, and the effect behaves obvious nonlinear characteristics, as seen in Figures 6 (a, b, d). While the increase of axial velocity and seal parameter  $\tau_0$  reduces  $\omega_c$  continuously, as depicted in Figures 6(c) and 6(e). However, it is found, through comparison, that the effect of axial velocity increased to a certain value on  $\omega_c$  is relatively limited, while that of  $\tau_0$  remains the notably linear trend. The observation of equation (6) signifies that the tangential cycling force formed by cross stiffness  $\tau_f \omega D$  is the main source resulting in instability. The larger the fluid damping ratio is, the more serious the system instability becomes. The stability can be improved by reducing  $\tau$ . It is known from equation (7) that  $\tau$  is proportional to  $\tau_0$  when other parameters remain unchanged, therefore, changing  $\tau_0$ , by means of anti-swirling, setting circumferential retaining piece, is an effective way to affect the critical instable speed. Increasing the seal clearance will raise  $\omega_c$  nonlinearly, as seen in Figure 6(f).

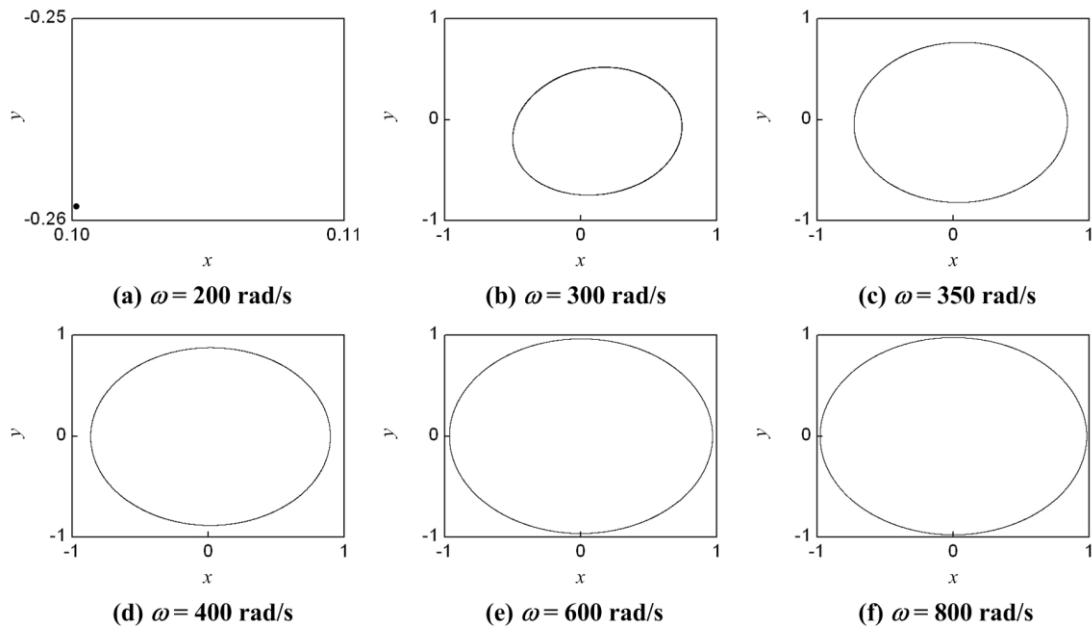


Figure 4 Trajectories of turbine under the nonlinear seal force with different rotational speed

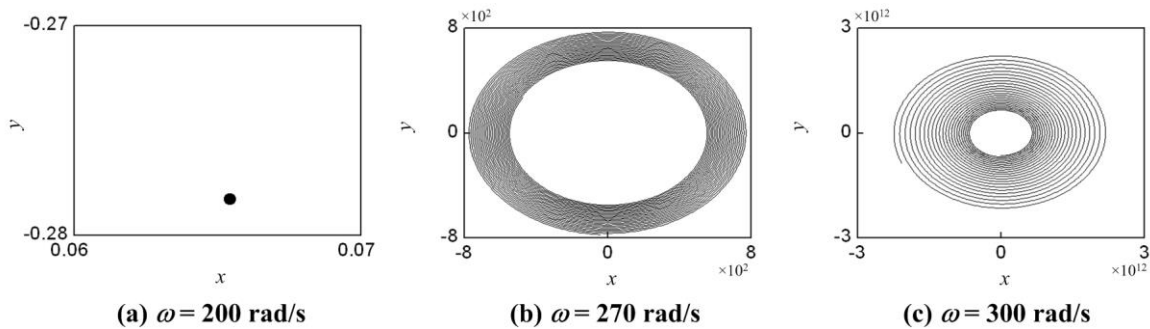


Figure 5 Trajectories of turbine under the linear seal force with different rotational speed

The above analysis shows that the increase of the axial velocity, seal pressure dropping and  $\tau_0$  is disadvantageous to the stability of the system. The seal length, seal radius and seal pressure dropping have a different impact on  $\omega_c$  according to their different values. The increase of the seal clearance can effectively reduce the influence of excited force in system. Nevertheless, it is noted that the increase of the seal clearance will also weaken the ability of seal to prevent fluid leakage, causing adverse effect to unit operation. Every coin has two sides; therefore, adjusting and optimizing the seal structure within a reasonable range of design parameters is the key to protect the stable operation for turbine-seal system.

The poor concentricity between turbine and chamber, and curved shaft axis are likely to induce self-excited vibration. The improvement of manufacturing, installation in order to reduce eccentricity and ensure the quality of barring shaft, is an important prerequisite to avoid the occurrence of self-excited vibration. In the event of instability, supplementary compressed air to cavity back changing axial velocity, and site polish expanding seal clearance are the better ways.

#### 4. Conclusions

Based on the model establishment and analysis of the whole shaft system, the stability and critical instable speed

of turbine-seal system under linear and nonlinear sealing force are emphasized, according to nonlinear vibration theory. Depending on the characteristics of the effect of different seal parameters on critical instable speed, some suggestions about reducing self-excited vibration are given to provide support with dynamic design and stable operation for turbine-seal system of unit. The main conclusions are as follows:

- Either linear or nonlinear seal system, when the rotating speed exceeds a critical instable speed, will lose stability at the balance point. With the increase of  $\omega$ , the turbine orbit amplitude increases drastically and consecutively. Compared to the nonlinear seal structure, the amplitude under linear sealing force is more obvious.
- The critical instable speed, calculated with Muszynska model, is lower than that with 8-parameters model, namely  $\omega_c$  is advanced and closer to the working speed. It is demonstrated that using nonlinear sealing force to analyze the dynamic characteristics of turbine-seal system is more advantageous to the stable operation of unit.
- The rub-impact between the turbine and seal structure for turbine-seal system under nonlinear sealing force may not happen with the increasing rotating speed after losing instability, in the absence of other external interferences.

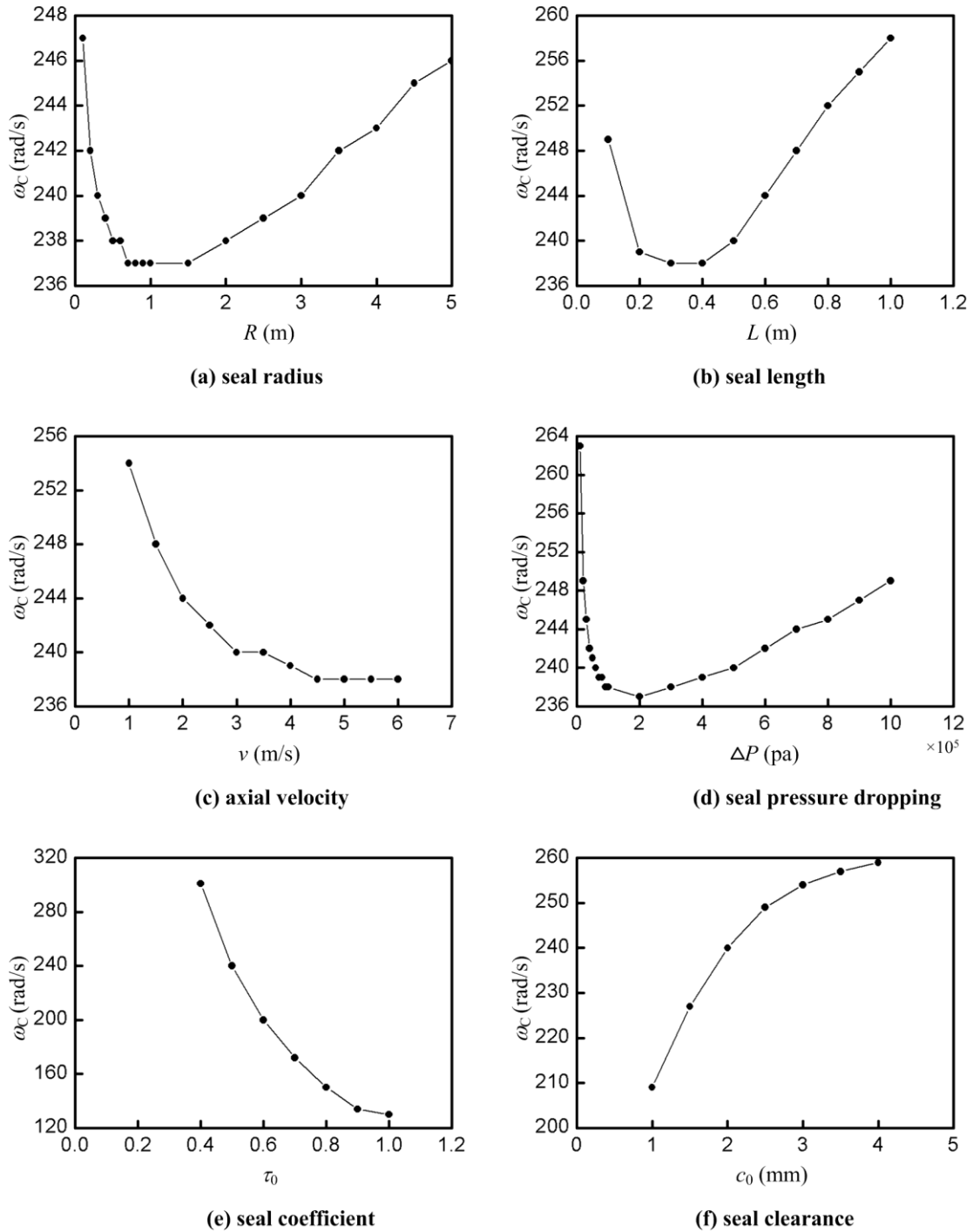


Figure 6. The effect of different sealing parameters on the system critical speed

- The effect of seal radius, seal length and seal pressure dropping on critical instable speed behaves obvious nonlinear characteristics as these parameters are increased,  $\omega_c$  decreases first then increases, and is more sensitive to the change of lower parameters values. The increase of axial velocity and  $\tau_0$  reduces  $\omega_c$ , aggravating the impact of the sealing force on the system vibration. For the seal clearance  $c_0$ , on the one hand, increasing  $c_0$  can improve  $\omega_c$ , which is good for reducing the system vibration. On the other hand, it weakens the ability of the seal to prevent fluid leakage,

which is disadvantageous to the system stability. Therefore, an appropriate adjustment of the seal parameters, based on the actual operation of the unit in order to improve the situation of the dynamic stability of the system, is necessary.

The UMP model, which is applicable to hydraulic generating set, does not include the electromagnetic cross items in the present paper; therefore, the stability analysis for the whole shaft system is not conducted. In fact, the influence of the electromagnetic stiffness in the system response is obvious and cannot be ignored, when UMP

changes. The dynamic characteristics of unit shaft system, under UMP, with consideration of cross electromagnetic items and sealing force, will be more deeply explored in a future work.

### Acknowledgement

This research paper is supported by the National Natural Science Foundation of China (No.51379030).

### References

- [1] Zhang Y. Mechanical Vibration. Beijing: Tsinghua University Press; 2007.
- [2] Ma Z. Dynamic analysis of hydraulic turbine generator set and penstock. Dalian: Dalian University of Technology, 1988.
- [3] D. E. Bently, A. Muszynska. "Role of circumferential flow in the stability of fluid-handling machine rotors". The 5th Workshop on Rotordynamic Instability Problems in High Performance Turbomachinery, A&M University, Texas, United states, 1988.
- [4] A. Muszynska, D. E. Bently, "Frequency-swept rotating input perturbation techniques and identification of the fluid force models in rotor/bearing/seal systems and fluid handling machines". Journal of Sound and Vibration, Vol. 143 (1990) No. 1, 103-124.
- [5] A. Muszynska, "Model testing of rotor /bearing systems". The International Journal of Analytical and Experimental Modal Analysis, Vol. 1 (1996) No. 3, 15-34.
- [6] Ma Z, Dong Y. Dynamics of Water Turbine Generator Set. Dalian: Dalian University of Technology Press; 2003.
- [7] H. Jordan, R. D. Schroeder, H. O. Seinsch, "Zur Berechnung einseitigmagnetischer Zugkräfte in Drehfeldmaschinen". Electrical Engineering (Archiv fur Elektrotechnik), Vol. 63 (1981) No. 2, 117-124.
- [8] H. Ohishi, S. Sakabe, K. Tsumagari, et al, "Radial magnetic pull in salient pole machines with eccentric rotors". IEEE Transactions on Energy Conversion, Vol. EC-2 (1987) No. 3, 439-443.
- [9] D. Guo, F. Chu, D. Chen, "The unbalanced magnetic pull and its effects on vibration in a three-phase generator with eccentric rotor". Journal of Sound and Vibration, Vol. 254 (2002) No. 2, 297-312.
- [10] P. Pennacchi, L. Frosini, "Dynamical behaviour of a three-phase generator due to unbalanced magnetic pull". IEE Proceedings: Electric Power Applications, Vol. 152 (2005) No. 6, 1389-1400.
- [11] Y. F. Wang, L. H. Huang, Y. Li, "Nonlinear vibration and stability of a jeffcott rotor under unbalanced magnetic excitation". International Journal of Nonlinear Sciences and Numerical Simulation, Vol. 8 (2007) No. 3, 375-384.
- [12] Qiu J. Electromechanical Analytical Dynamics. Beijing: Science Press; 1992.
- [13] Y. Wang, L. Huang, J. Hu, "The effect of unbalanced magnetic pull on the motor rotor dynamic characteristics". Mechanics in Engineering, Vol. 18 (1996) No. 4, 32-34.
- [14] Huang Z. Vibration mechanism for hydroelectric generating unit based on nonlinear rotor dynamics. Wuhan: Huazhong University of Science and Technology, 2011.
- [15] W. Ma, W. Liang, H. Nan, et al, "The influence of sealing clearance value of francis runner on the unit stability". Journal of Hydroelectric Engineering, Vol. 29 (2010) No. 4, 219-223.
- [16] Z. Ma, Y. Dong, "The dynamic characteristics on seal of turbine runner and it's effect on the behaviour of free vibration of unit". Large Electric Machine and Hydraulic Turbine, (1987) No. 6, 43-50.
- [17] Yang X. Research on generating set vibration and coupled that and hydropower house vibration in hydropower station. Dalian: Dalian University of Technology, 2006.
- [18] L. Zhang, Z. Ma, B. Song, "Characteristics analysis of hydroelectric generating set under unbalanced magnetic pull and sealing force of runner". Water Resources and Power, Vol. 28 (2010) No. 9, 117-120.
- [19] D. Kong, Z. Li, Y. Jiao, et al, "Models of the rotor-seal system for hydraulic turbine and its nonlinear dynamics analysis". Journal of Hydraulic Engineering, Vol. 44 (2013) No. 4, 462-469.
- [20] Y. Calleecharan, J. Aidanpää, "Dynamics of a hydropower generator subjected to unbalanced magnetic pull ". Proceedings of the Institution of Mechanical Engineers, Part C: Journal of Mechanical Engineering Science, Vol. 225 (2011) No. 9, 2076-2088.
- [21] L. Lundström, R. Gustavsson, J. O. Aidanpää, et al, "Influence on the stability of generator rotors due to radial and tangential magnetic pull force". IET Electric Power Applications, Vol. 1 (2007) No. 1, 1-8.
- [22] Y. Xu, Z. Li, "Computational model for investigating the influence of unbalanced magnetic pull on the radial vibration of large hydro-turbine generators". Journal of Vibration and Acoustics, Vol. 134 (2012) No. 5, 51013-51019.
- [23] Y. Y. Zeng, Y. Zeng, Z. Wu, et al, "Impact of the unbalanced magnetic pull on the shafting vibration of hydro turbine generating sets". Applied Mechanics and Materials, Vol. 644-650 (2014), 406-411.
- [24] Z. Song, Z. Ma, "Nonlinear vibration analysis of an eccentric rotor with unbalance magnetic pull". Journal of Vibration and Shock, Vol. 29 (2010) No. 8, 169-173.
- [25] R. K. Gustavsson, J. O. Aidanpää, "Evaluation of impact dynamics and contact forces in a hydropower rotor due to variations in damping and lateral fluid forces". International Journal of Mechanical Sciences, Vol. 51 (2009) No. 9-10, 653-661.
- [26] F. Chu, Z. Zhang, "Periodic, quasi-periodic and chaotic vibrations of a rub-impact rotor system supported on oil film bearings". International Journal of Engineering Science, Vol. 35 (1997) No. 10-11, 963-973.



# The Effects of a Magnetic Gradient on Lifted Diffusion Flames

Ibrahim Mabrouki <sup>a \*</sup>, Mohamed Ali Merghini <sup>b</sup>, Zied Driss <sup>a</sup> and Mohamed Salah Abid<sup>a</sup>

<sup>a</sup> *Laboratory of Electro-Mechanic Systems, National School of Engineers of SFAX (ENIS), University of SFAX, B.P. 1173, Road SOUKRA km 3.5, 3038 SFAX, TUNISIA*

<sup>b</sup> *Ecole Nationale d'Ingénieurs de Monastir, LESTE, 5019 Monastir, Tunisie*

Received 25 Nov. 2014

Accepted 19 July 2015

## Abstract

Reducing pollution and increasing energy efficiency are two tests extensive studies for combustion. Methane is a fuel of choice; it releases a large amount of heat and its molecular simplicity allows it to produce less pollutants. In many systems, the use of methane combustion takes place by diffusion flame. In the present paper, we developed impact of a magnetic field gradient to develop a laminar flame with an axisymmetric actuator CH<sub>4</sub>/air. Results are explained by the effects of magnetic force, and thermo magnetic convection which involves the thermal variation of magnetic susceptibility. The gradient of a magnetic field reduces the air velocity and the spatial gradient of the mass fraction of methane, which are important effects of reducing the lift-off height and increasing the propagation flame velocity.

© 2015 Jordan Journal of Mechanical and Industrial Engineering. All rights reserved

**Keywords:** *Laminar Diffusion Flames CH<sub>4</sub>/Air, Magnetic Field, Lift-Off Height, Experimental Study, CFD.*

## 1. Introduction

To solve the equations assessments, FLUENT utilizes the finite volume method [1]. This method is to integrate on a control volume balance sheet equations [2]. After these equations were discredited, conditions for defined limits must solve the system of equations. Combustion process control is of a considerable interest at both scientific and economic levels, as it is connected with the problem of energy efficiency and ecological improvement. Among the numerous methods of combustion control, the application of a magnetic field is one of the most promising [3-6]. The authors have shown an increase of the combustion rate only in the specific configuration of combustion of solid propellant in rocket motors. Inducing a Lorentz force opposed to the flow of ionized gaseous products decelerated the flow leading to an increase of the static pressure from which the combustion rate directly depends. However, the amount of ionized species and their velocity are too small in ordinary diffusion flames to take into account the influence of the Lorentz force. Many researchers studied the direct effect of a uniform magnetic field up to 5T on chemical kinetics for a premixed laminar flame of propane/air. If high speed chemical reactions seem not to be affected, nitrogen oxide formation shows a slight difference under magnetic influence [7-12]. Action of the magnetic gradient on the air surrounding the flame

explains the flame deformations and then the the changes of the temperature and the OH radical emissions. In 1996, Wakayama observed that the magnetic gradient promotes the combustion process, attributing this effect to an increase in the oxygen supply at the flame front by magneto convection due to the magnetic susceptibility difference between air and flame products. This shows how the magnetic field can sustain combustion in microgravity environment through this mechanism. A diffusion flame issued from a single jet of fuel in ambient air can have different behavior depending on the injection conditions: attached to the burner, lifted or blown out. The lift-off height is shown depending on both the flow rate and the flame propagation. Concerning the lifted flame, they suggested the triple flame configuration [13]. The flame is composed of three branches along the stoichiometric contour: a rich branch close to the fuel jet, a lean branch and, in the middle, a diffusion flame. These branches are issued from a point called the triple point. The unfastened from the laminar flame burner continue to be studied in order to identify the mechanisms that lead to the detaching (liftoff). In fact, the understanding of the mechanisms of stabilization of the flames jerked is of crucial importance as well for the fundamental studies for practical applications [14-15]. In the past, it was often used in fireworks to minimize or reduce this stall and, especially, in the turbulent flames. To operate this stabilization of flame, its coupling to the burner are used.

\* Corresponding author. e-mail: mabroukiibrahim@hotmail.fr.

Indeed, the flames require a change of the burner geometry, or assistance by plasma, electric field or magnetic field [16-17].

In the present paper, we are interested in the impact of a magnetic field gradient to develop a laminar flame with an axisymmetric actuator  $\text{CH}_4/\text{air}$ . The obtained flame is a laminar flame triple (triple flame) which can be lifted off the burner if the conditions of the speed of the flow are favorable. However, it should be recalled that the goal is not to ensure whether the market model in our simulations is good or bad; the goal is to study the effect of the magnetic field on the flame.

## 2. Geometrical Configuration

The configuration of the burner is schematized in Figure 1. This burner coaxial is composed of an inner tube of internal diameter  $D_i = 6$  mm and of an annular tube of internal diameter of  $D_e = 18$  mm. The inner tube is chamfered on its external part. The inner tube is powered by the methane ( $\text{CH}_4$ ) and the external tube is powered by the air. The configuration of this burner allows us to carry out a study of an axisymmetric actuator around the central axis of the burner.

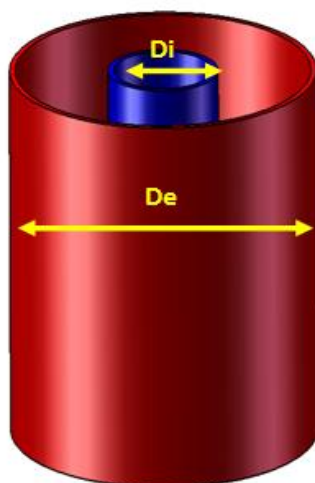


Figure 1. Configuration

The burner is composed of two coaxial jets from two concentric tubes. The center circle contains the jet fuel ( $\text{CH}_4$ ) and the annular jet of air (Figure 2). The influence of the magnetic field, in the present study, was modeled by the addition of a volume equation within the strength of impulse. This strength is modeled on all the height of the object domain which is limited by the total width of the burner. The strength is in every stitch applied. The flow successively passes through a field gradient positive to  $y = 5$  mm and a field gradient to negative 15 mm. The magnetic force is successively positive (pointing to the top according to  $y$ ) then negative on the air.

We chose the following modes:

Quad: the mesh is structured by quadrilateral elements only.

Map: the mesh is regular.

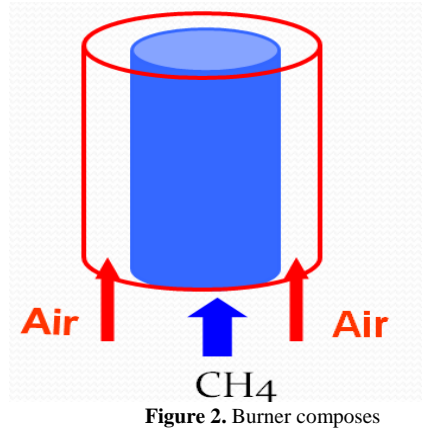


Figure 2. Burner composes

The selected interval is equal to 0.0072 m. The number of mesh is 5004 (Figure 3).

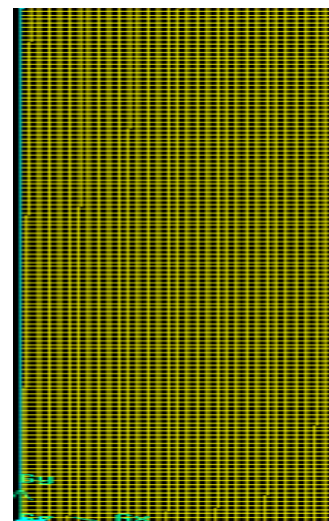


Figure 3. Geometry mesh

## 3. Numerical results

### 3.1. Current Lines

The current lines presented in Figures 4 and 5 provide the following information. In fact, we found the wake left by the inner wall of the burner and the Poiseuille flow conditions. The two jets are little changed. In fact, the current lines are slightly more spaced with field than without. The magnetic impact depends on the direction of the gradient. For  $0 < y < 10$  mm, the current lines are more inclined and more tightened. For  $y > 10$  mm, the gap between the lines increases, and the slope is lesser. In the first gradient, which the maximum is at  $y = 5$  mm, the jet of air is accelerated. Indeed, it was observed that the lines are more inclined and more tightened. For  $y > 10$  mm, the gap between the lines increases, and the slope is lesser.

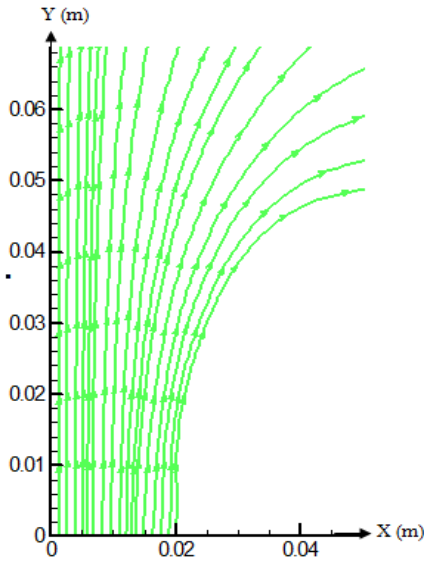


Figure 4. Current lines without magnetic field

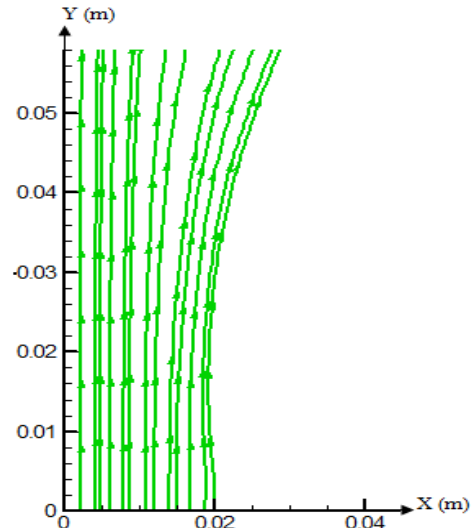


Figure 5. Current lines with magnetic field

### 3.2. Evolution Axial

Figure 6 presents a comparison between the evolution of the speed on the axial axis of symmetry with and without a magnetic field. The third areas of the flow are always presented. On the first area in the field, the least of the speed drop is noted, and on the second and third boxes, the velocity is low compared with the case without field. These comments are attributed to the fact that the magnetic force acts on the air, thereby slowing the annular jet and, thus, allowing the central jet to be less embarrassed by the annular jet. The annular jet reaches the pin with a lower speed cause by the action of the magnetic field.

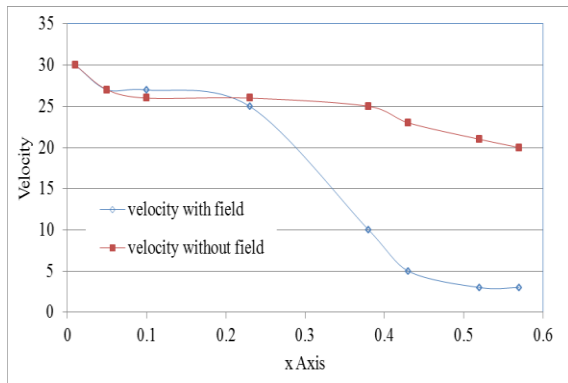


Figure 6. Variation of axial velocity

### 3.3. Evolution of Temperature

Figure 7 presents the variation of the temperature, according to these results. It was noted that, in the case of  $y = 0$  mm, the magnetic field had a great effect on the evolution of the temperature. The temperature decreased with the presence of the magnetic field and allowed us to show that the height of the detaching decreased due to

the magnetic field. Indeed, it was noted that the maximum temperature was equal to 2800 K. without field. The maximum temperature with the magnetic field was equal to 2400 K.

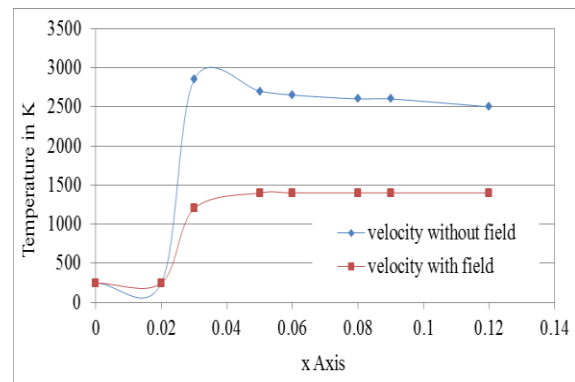


Figure 7. Variation of temperature

### 3.4. Evolution of the Radial Velocity

Figures 8, 9, 10 and 11 curves present the evolution of the radial velocity. According to the results, it was noted that the slope of the radial velocity was not changed by the magnetic field but the values were low. The magnetic field was observed in the area of the low velocity due to the wall of the injector. Indeed, it was noted that the slope of the speed was not changed by the magnetic field. In fact, the values were low, the magnetic field had an effect on the area of the low speed due to the injector wall. For  $y = 0$  mm and  $y = 20$  mm, the curves showed the effect of the magnetic field helping the annular jet by increasing its speed and disrupting the curve the mixed layer air/air. For  $y=100$ , the magnetic field opposed the mixture. For  $y=300$ , the magnetic field's effect on the mixed layer was by reducing velocity.

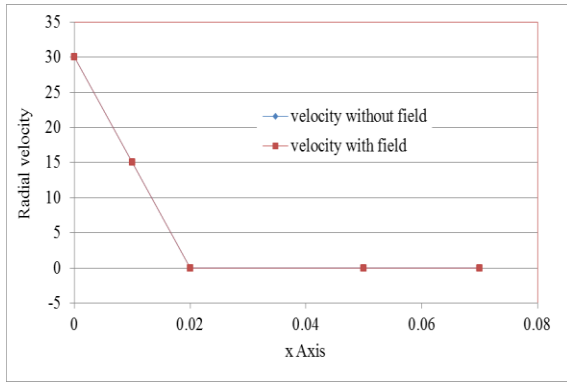


Figure 8 Radial velocity for y=0 mm

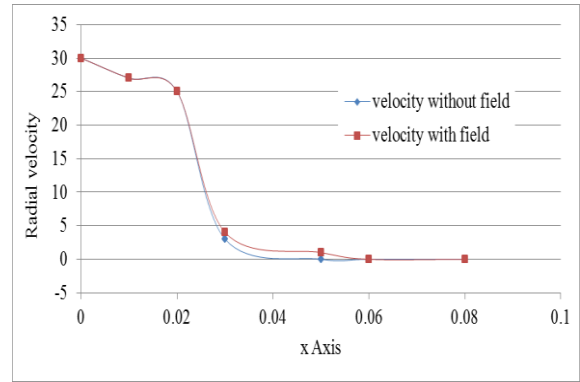


Figure 9 Radial velocity for y=20 mm

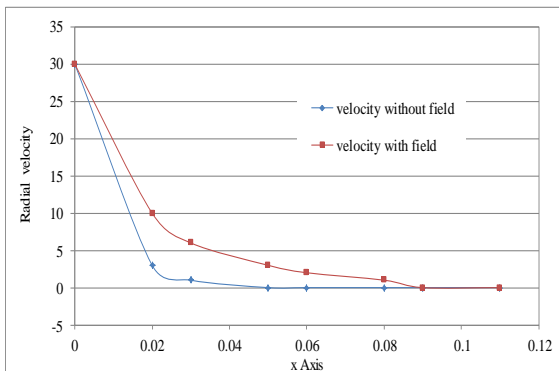


Figure 10 Radial velocity for y=100 mm

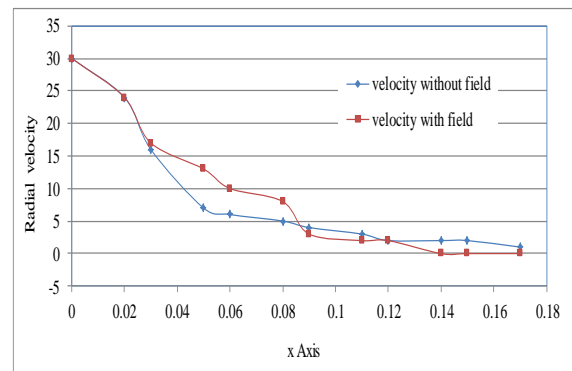


Figure 11 Radial velocity for y=200 mm

3.5. Species Distribution

Figure 12 shows the species distribution with and without magnetic field. According to these results, it was noted that the CO<sub>2</sub> was more important in the case without the magnetic field. Particularly, the CO<sub>2</sub> was formed mainly at the level of the flame.

Figure 13 shows the species distribution with and without magnetic field. According to these results, it was noted that the N<sub>2</sub> was more important in the case without the magnetic field. Particularly, the N<sub>2</sub> was formed mainly at the level of the flame.

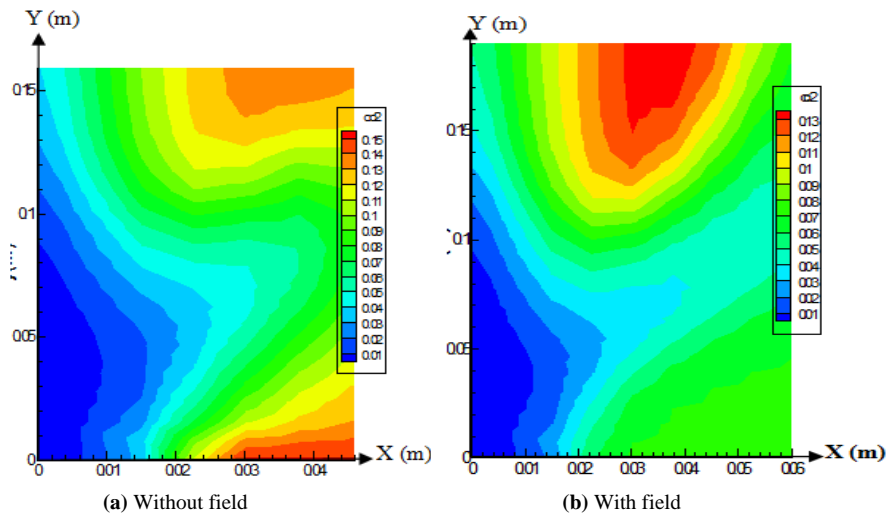


Figure 12 The distribution with and without magnetic field of CO<sub>2</sub>

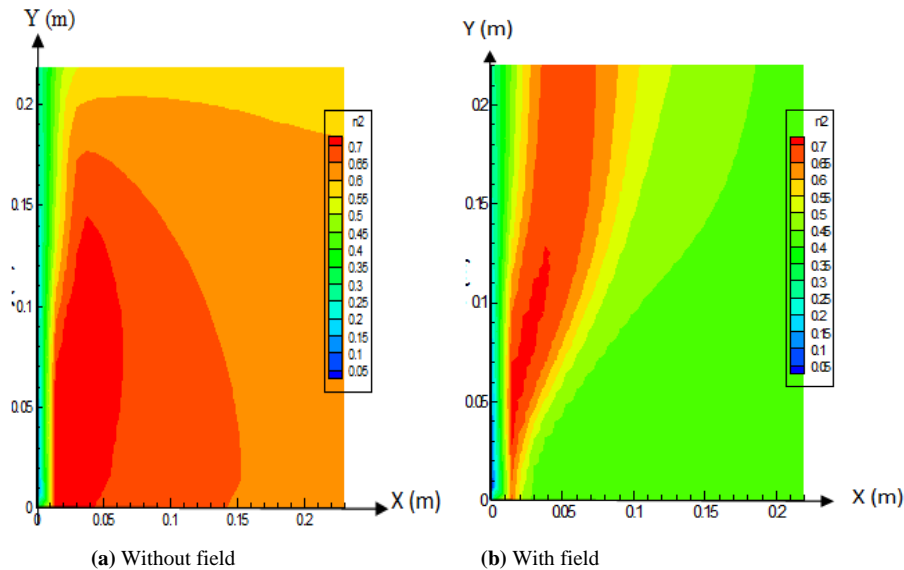


Figure 13 The distribution with and without magnetic field of  $N_2$

#### 4. Validation

We showed that the temperature decreased with the presence of the magnetic field, allowing us to show that the height of detaching declined due to the magnetic field, as described in the article by Baker *et al.*, for a low velocity. Air the flame is shorter with flame attached broader and bluer. The action of a magnet permanent place at the output of the burner to two different vertical positions shows that the height of lift is reduced by the action of magnetic field gradient which leads to an increase in the stability area. In fact, the air flows and methane, necessary for the extinction, are higher.

We have shown that the magnetic force acts on the air, thereby slowing the annular jet and, thus, allowing the central jet to be the least bothered by the annular jet. According to Wakayama *et al.*, it is possible to control the combustion on the flames of dissemination from a magnetic field. They deduced that the application of the magnetic field allows changing the dynamics of the ambient air, which have an effect on the dissemination flame.

#### 5. Conclusion

A numerical study was carried out on the effects of a magnetic field gradient on lifted diffusion flames. The effects of a magnetic field gradient were considered to see the relevant physical aspects of the magnetic field and to validate the present numerical results when compared to other numerical data. The different laws that govern the system have been developed and the various changes made to the solver shown. The magnetic force and the dynamic equations have been established in the two dimensional stationary case. We have demonstrated that the application of the magnetic field allows reducing the velocity of the playground and the spatial gradient of mass fraction of methane; it also led to a decrease in the height of detaching and an increase in the speed of propagation of the flame.

#### Acknowledgements

The authors would like to thank the Laboratory of Electro-Mechanic Systems (LASEM) members for the financial assistance they provided.

#### References

- [1] M. Ibrahim, Z. Driss, M.S. Abid, "Numerical Study of the Hydrodynamic Structure of a Water Savonius Rotor in a Test Section". Jordan Journal of Mechanical and Industrial Engineering, Vol. 8 (2014), No. 3, 127-136.
- [2] N.I. Wakayama, M. Sugie, "Magnetic promotion of combustion in diffusion flames". Physica B: Condensed Matter, Vol. 216 (1996), 403-405.
- [3] M. Houshiar, F. Zebhi, Z.J. Razi, A. Alidoust, Z. Askari, "Synthesis of cobalt ferrite ( $CoFe_2O_4$ ) nanoparticles using combustion, coprecipitation, and precipitation methods: A comparison study of size structural, and magnetic properties", Journal of Magnetism and Magnetic Materials, Vol. 371 (2014), 43-48.
- [4] Manikandan, R. Sridhar, S.A. Antony, R. Seeram, "A simple aloe vera plant-extracted microwave and conventional combustion synthesis: Morphological, optical, magnetic and catalytic properties of  $CoFe_2O_4$  nanostructures". Journal of Molecular Structure, Vol. 1076 (2014), 188-200.
- [5] V.M Khot, A.B Salunkhe, N.D Thorat, M.R Phadatar, S.H Pawar, "Induction heating studies of combustion synthesized  $MgFe_2O_4$  nanoparticles for hyperthermia applications". Journal of Magnetism and Magnetic Materials, Vol. 332, (2013), 48-51.
- [6] Y. Kang, Q. Wang, X. Lu, X. Ji, S. Miao, H. Wang, Q. Guo, H.H. He, J. Xu, "Experimental and theoretical study on the flow, mixing, and combustion characteristics of dimethyl ether, methane, and LPG jet diffusion flames". Fuel Processing Technology, Vol. 129, (2015), 98-112.
- [7] M.R. Charest, Ö.L. Gülder, C.P.T Groth, "Numerical and experimental study of soot formation in laminar diffusion flames burning simulated biogas fuels at elevated pressures". Combustion and Flame, Vol. 161 (2014), 2678-2691.
- [8] Q. Wang, L. Hu, M. Zhang, F. Tang, X. Zhang, S. Lu, "Lift-off of jet diffusion flame in sub-atmospheric pressures: An

- experimental investigation and interpretation based on laminar flame speed". *Combustion and Flame*, Vol. 161 (2014), 1125-1130.
- [9] Cuoci, A. Frassoldati, T. Faravelli, H. Jin, Y. Wang, K. Zhang, P. Glarborg, F. Qi, "Experimental and detailed kinetic modeling study of PAH formation in laminar co-flow methane diffusion flames". *Proceedings of the Combustion Institute*, Vol. 34 (2013), 1811-1818.
- [10] Wu, K. Chen, "Characterization of hydrogen triple flame propagation in vitiated laminar coaxial flow". *International Journal of Hydrogen Energy*, Vol. 39 (2014), 14109-14119.
- [11] M. Mansour, A.M. Elbaz, M. Samy, "The stabilization mechanism of highly stabilized partially premixed flames in a concentric flow conical nozzle burner". *Experimental Thermal and Fluid Science*, Vol. 43 (2012), 55-62.
- [12] M.S. Mansour, A. Elbaz, M. Samy, "The stabilization mechanism of highly stabilized partially premixed flames in a concentric flow conical nozzle burner". *Experimental Thermal and Fluid Science*, Vol. 43 (2012), 55-62.
- [13] K. Kedia, A. Ghoniem, "Mechanisms of stabilization and blow off of a premixed flame downstream of a heat-conducting perforated plate". *Combustion and Flame*, Vol. 159 (2012), 1055-1069.
- [14] K. Nogenmyr, P. Petersson, X. Bai, C. Fureby, R. Collin, A. Lantz, M. Linne, M. Aldén, "Structure and stabilization mechanism of a stratified premixed low swirl flame". *Proceedings of the Combustion Institute*, Vol. 33 (2011), 1567-1574.
- [15] Chen, Y. Chao, T. Cheng, G. Chen, C. Wu, "Structure and stabilization mechanism of a microjet methane diffusion flame near extinction". *Proceedings of the Combustion Institute*, Vol. 31 (2007), 3301-3308.
- [16] R. Catapan, A. Oliveira, M. Costa, "Non-uniform velocity profile mechanism for flame stabilization in a porous radiant burner". *Experimental Thermal and Fluid Science*, Vol. 35 (2011), 172-179.
- [17] T. Yazan, "CFD Simulations of Drag and Separation Flow Around Ellipsoids". *Jordan Journal of Mechanical and Industrial Engineering*, Vol. 5 (2011), No. 2, 129-132.

# The Effect of the Couple Stress Fluid Flow on MHD Peristaltic Motion with Uniform Porous Medium in the Presence of Slip Effect

Dr. S. Ravi Kumar \*

Department of Mathematics, NBKR Institute of Science and Technology (An Autonomous Institution, Accredited by NBA and 'A'- Grade of NAAC, ISO 9001:2008 Certified), Vidyanagar, SPSR Nellore, Andhra Pradesh, India. Pin-524413

Received 16 Feb 2015

Accepted 22 Aug 2015

## Abstract

The present paper investigates the effects of the couple stress fluid flow on the magnetohydrodynamic peristaltic motion with a uniform porous medium in the presence of slip effect. The analysis is carried out under the assumption of long wavelength approximations. Expressions of the axial velocity, transverse velocity, pressure gradient, volume flow rate, average volume flow rate, pressure rise and shear stress are all obtained. The effects of various emerging axial velocity, transverse velocity, pressure gradient shear stress are discussed through graphs. It was observed that the velocity distribution ( $u$ ) decreased by increasing the couple stress parameter ( $S$ ) with  $\beta \geq 0.2$ ; we also noticed that the transverse velocity increased by increasing the couple stress parameter ( $S$ )  $\beta \geq 0.2$ . We noticed that the pressure gradient decreased by increasing the slip parameter ( $\beta$ ).

© 2015 Jordan Journal of Mechanical and Industrial Engineering. All rights reserved

**Keywords:** Peristaltic Fluid Flow, Porous Medium, Magnetic Field, Slip Condition, Couple Stress.

## 1. Introduction

Peristaltic motion is now well-known to the physiologists as one of the major mechanisms for fluid transport in many biological systems and it is also an important research topic due to its great amount of applications in engineering. A fluid transport induced by a progressive wave of area contraction or expansion along the length of a distensible tube containing fluid is called peristaltic transport. It is an automatic and vital process that moves food through the digestive tract, urine from the kidneys through the ureters into the bladder, and bile from the gallbladder into the duodenum and transport of blood through the artery with mild stenosis. In addition, peristaltic pumping occurs in many practical applications involving biomechanical systems. This mechanism also has many applications in roller and finger pumps, some bio-mechanical instruments (e.g., heart-lung machine, blood pump machine and dialysis machine). Thus, peristaltic transport has been the core interest of many recent studies of researchers/scientists owing to the above-mentioned applications in bio-mechanical engineering and bio-medical technology. Latham [1] first initiated the concept of peristaltic mechanism. Later, this mechanism became an important topic of research owing to the above-mentioned applications in biomechanical engineering and biomedical technology.

Researchers have considered different geometries and fluids to understand the mechanism of peristalsis under different assumptions. Some recent investigations on this topic have been reported in Refs. [2 - 13]. Magnetohydrodynamic (MHD) is the science which deals with the motion of highly conducting fluids in the presence of a magnetic field. The motion of the conducting fluid across the magnetic field generates electric currents which change the magnetic field; the action of the magnetic field on these currents gives rise to mechanical forces which modify the flow of the fluid [14]. As early as 1937, this was due to the fact that such studies were useful, particularly for getting a proper understanding of the functioning of different machines used by clinicians for pumping blood (Misra *et al.* [15]). Misra *et al.* [16] surveyed the theoretical studies with the aim of exploring the effect of the magnetic field on the flow of blood in atherosclerotic vessels; they also found an application in a blood pump used by cardiac surgeons during the surgical procedure. The MHD principles may be used to reaccelerate the flow of blood in a human artery system and thereby they found it useful in the treatment of certain cardiovascular disorders [17] and in the diseases with an accelerated blood circulation like hemorrhages and hypertension, etc.

MHD heat and mass transfer free convection flow near the lower stagnation point of an isothermal cylinder imbedded in porous domain with the presence of radiation

\* Corresponding author. e-mail: : drsravikumar1979@gmail.com.

was studied by ziya uddin [18]. Static and dynamic analysis of hydrodynamic four-lobe journal bearing with couple stress lubricants was studied by boualem chetti [19].

The couple stress fluid is a special case of the non-newtonian fluids where these fluids consist of rigid randomly oriented particles suspended in a viscous medium and their sizes are taken into account. This model can be used to describe the human and animal blood, infected urine from a diseased kidney and liquid crystals. There have been only few attempts for studying the peristaltic flow of couple stress fluids, first discussed by Stokes [20]. From the recent attempts dealing with the couple stress model, we referred to Mekheimer [21], as he investigated the problem of the peristaltic transport of couple stress fluids in a uniform and non-uniform channel. Also, Nadeem and Akram [22] investigated the peristaltic flow of couple stress fluids under the effect of induced magnetic field in an asymmetric channel. Similarly, Sobh [23] studied the effect of slip velocity on peristaltic flow of couple stress fluids in uniform and non-uniform channels. The peristaltic fluid flow, through channels with flexible walls, was studied by Ravi Kumar *et al.* [24-31].

Flow through porous media has been of a considerable interest in the recent years due to its potential application in all fields of Engineering, Geo-fluid dynamics and Biomechanics. The study of flow through porous media is immensely vital for understanding the transport process in lungs, kidneys, gallbladder with stones, the movement of small blood vessels and tissues, cartilage and bones, etc. Most of the tissues in the body (e.g., bone, cartilage, muscle) are deformable porous media. The proper functioning of such materials depends crucially on the flow of blood, nutrients and so forth through them. Porous-medium models are used to understand various medical conditions (such as tumor growth) and treatments (such as injections). One class contains the rarefied gases (Kwang and Fang [32]), while the other fluids have much more an elastic character. In such fluids, some slippage occurs under a large tangential traction. It was claimed that the slippage can occur in non-Newtonian fluids, concentrated polymer solution, and molten polymer. Furthermore, in the flow of dilute suspensions of particles, a clear layer is sometimes observed next to the wall. Poiseuille, in a work that won a prize in experimental physiology, observed such a layer with a microscope in the flow of blood through capillary vessels [33]. The effects of the induced magnetic field and the slip condition on peristaltic transport with heat and mass transfer in a non-uniform channel were studied by Najma Saleem *et al.* [34]. Peristaltic Transport of Visco-Elasto-Plastic Fluids in a Planar Channel was investigated by Zaheer Asghar *et al.* [35]. Slip Effects on Peristaltic Transport of a Particle-Fluid Suspension in a Planar Channel was studied by Mohammed H. Kamel *et al.* [36].

To the best of our knowledge, no attempt has yet been reported to discuss the effects of couple stress fluid flow on MHD peristaltic motion with uniform porous medium in the presence of slip effect. The aim of the present study is to investigate the effects of couple stress fluid flow on magnetohydrodynamic peristaltic motion with uniform porous while taking into consideration of slip effect during this work. This investigation may have an application in

many clinical applications such as endoscopes problem. Since the present study was carried out for a situation when the human body is subjected to an external magnetic field, it bears the promise of a significant application in magnetic or electromagnetic therapy, which has gained a considerable popularity. The present study is also useful for evaluating the role of porosity and slip condition when the body is subjected to magnetic resonance imaging (MRI).

## 2. Mathematical Formulation and Solution

We considered the unsteady hydromagnetic flow of a viscous, incompressible and electrically conducting couple-stress fluid through a two-dimensional channel of non-uniform thickness with a sinusoidal wave travelling down its wall. The plates of the channel were assumed to be electrically insulated. We chose a rectangular coordinate system for the channel with  $x$  along centerline in the direction of wave propagation and  $y$  transverse to it.

The geometry of the wall surface is defined as:

$$h(x, t) = a(x) + b \sin \frac{2\pi}{\lambda} (x - ct) \quad (1)$$

with  $a(x) = a_0 + kx$

where  $a(x)$  is the half-width of the channel at any axial distance  $x$  from inlet,  $a_0$  is the half-width at inlet,  $k(\ll 1)$  is a constant whose magnitude depends on the length of the channel and inlet dimensions,  $b$  is the wave amplitude,  $\lambda$  is the wave length,  $c$  is the propagation velocity and  $t$  is the time.

The constitutive equations and equations of motion for a couple stress fluids are (Stocks, 1966):

$$T_{ji,j} + \rho f_i = \rho \frac{\partial v_i}{\partial t}$$

$$e_{ijk} + T_{jk}^A + M_{ji,j} + \rho C_i = 0$$

$$\tau_{ij} = -p' \delta_{ij} + 2\mu d_{ij}$$

$$\mu_{ij} = 4\eta \omega_{j,i} + 4\eta' \omega_{j,i}$$

Where  $f_i$  is the body force vector per unit mass,  $C_i$  is the body moment per unit mass,  $v_i$  is the velocity vector,  $\tau_{ij}$  and  $T_{jk}^A$  are the symmetric and anti-symmetric parts of the stress tensor  $T_{jk}$  respectively,  $M_{ij}$  is the couple stress tensor,  $\mu_{ij}$  is the deviatoric part of  $M_{ij}$ ,  $\omega_i$  is the vorticity vector,  $d_{ij}$  is the symmetric part of the velocity gradient,  $\eta$  and  $\eta'$  are constants associated with the couple stress,  $p'$  is the pressure, and the other terms have their usual meaning from tensor analysis.

We introduced a wave frame of reference  $(x, y)$  moving with velocity  $c$  in which the motion became independent of time when the channel length was an integral multiple of the wavelength and the pressure difference at the ends of the channel was a constant [38]. The transformation from the fixed frame of reference  $(X, Y)$  to the wave frame of reference  $(x, y)$  is given by:

$$x = X - ct, y = Y, u = U - c, v = V \text{ and } p(x) = P(X, t),$$

where  $(u, v)$  and  $(U, V)$  are the velocity components,  $p$  and  $P$  are pressures in the wave and fixed frames of reference, respectively.

Neglecting the body force and the body couples, the

continuity equations and equations of motion are [37]:

$$\frac{\partial u}{\partial x} + \frac{\partial v}{\partial y} = 0 \tag{2}$$

$$\rho \left[ \frac{\partial u}{\partial t} + u \frac{\partial u}{\partial x} + v \frac{\partial u}{\partial y} \right] = - \frac{\partial p}{\partial x} + \mu \left[ \frac{\partial^2 u}{\partial x^2} + \frac{\partial^2 u}{\partial y^2} \right] - \left[ \sigma B_0^2 \right] u - \left[ \frac{\mu}{k_1} \right] u - \eta \nabla^4 u \tag{3}$$

$$\rho \left[ \frac{\partial v}{\partial t} + u \frac{\partial v}{\partial x} + v \frac{\partial v}{\partial y} \right] = - \frac{\partial p}{\partial y} + \mu \left[ \frac{\partial^2 v}{\partial x^2} + \frac{\partial^2 v}{\partial y^2} \right] - \left[ \sigma B_0^2 \right] v - \left[ \frac{\mu}{k_1} \right] v \tag{4}$$

$u$  and  $v$  are the velocity components in the corresponding coordinates  $p$  is the fluid pressure,  $\rho$  is the density of the fluid,  $\mu$  is the coefficient of the viscosity,  $\eta$  is the coefficient of couple stress,  $k_1$  is the permeability of the porous medium and  $k$  is the thermal conductivity.

Since it is presumed that the couple stress is caused by the presence of the suspending particles, obviously the clear fluid cannot support the couple stress at the boundary, hence we tactically assumed that the components of the couple stress tensor at the wall vanishes.

Using the following the non-dimensional variables:

$$x^* = \frac{x}{\lambda} \quad y^* = \frac{y}{a_0} \quad u^* = \frac{u}{c} \quad v^* = \frac{\lambda v}{a_0 c}$$

$$p^* = \frac{a_0^2 p}{\lambda \mu c} \quad t^* = \frac{ct}{\lambda} \quad Re = \frac{\rho c a_0}{\mu}$$

$$M = \sqrt{\frac{\sigma}{\mu}} B_0 a_0 \quad S = \frac{a_0^2 \eta}{4 \mu a_0}$$

$$\delta = \frac{a_0}{\lambda} h = 1 + \frac{\lambda k x}{a_0} + \phi \sin \{ 2\pi (x - t) \}$$

here  $\phi$  (amplitude ratio) =  $\frac{b}{a_0} < 1$

Equations of motion and boundary conditions in the dimensionless form become:

$$\frac{\partial u}{\partial x} + \frac{\partial v}{\partial y} = 0 \tag{5}$$

$$Re \delta \left[ \frac{\partial u}{\partial t} + u \frac{\partial u}{\partial x} + v \frac{\partial u}{\partial y} \right] = - \frac{\partial p}{\partial x} + \delta^2 \frac{\partial^2 u}{\partial x^2} + \frac{\partial^2 u}{\partial y^2} - s \delta^4 \frac{\partial^4 u}{\partial x^4} - s \frac{\partial^4 u}{\partial y^4} - 2s \delta^2 \frac{\partial^2 u}{\partial x^2 \partial y^2} - \frac{1}{D} u - M^2 u \tag{6}$$

$$Re \delta \left[ \frac{\partial v}{\partial t} + u \frac{\partial v}{\partial x} + v \frac{\partial v}{\partial y} \right] = - \frac{\partial p}{\partial y} + \delta^4 \frac{\partial^2 v}{\partial y^2} + \delta^4 \frac{\partial^2 v}{\partial y^2} + \delta^2 \frac{\partial^2 v}{\partial y^2} - \delta^2 \frac{1}{D} v - \delta^2 M^2 v \tag{7}$$

Using long wavelength (i.e.,  $\delta \ll 1$ ) and negligible inertia (i.e.,  $Re \rightarrow 0$ ) approximations, we have:

$$S \frac{\partial^4 u}{\partial y^4} - \frac{\partial^2 u}{\partial y^2} + A u = - \frac{\partial p}{\partial x} \tag{8}$$

where  $A = \left[ M^2 + \frac{1}{D} \right]$  (9)

$$\frac{\partial p}{\partial y} = 0$$

The associated boundary conditions are:

Slip condition:  $u = -\beta \frac{\partial u}{\partial y}$  at  $y = h$  (10)

where  $\beta$  is the slip parameter.

Regularity condition:  $\frac{\partial u}{\partial y} = 0$  at  $y = 0$  (11)

Vanishing of couple stresses,  $\frac{\partial^2 u}{\partial y^2} = 0$  at  $y = h$

$$\frac{\partial^3 u}{\partial y^3} = 0 \text{ at } y = 0 \tag{12}$$

Solving equation (8) using the boundary conditions (10 and 12), we get

$$u = -B N_1 \text{Cosh}[a y] + B N_2 \text{Cosh}[b y] - B \tag{13}$$

where  $a = \sqrt{\frac{1 + \sqrt{1 - 4S(M^2 + \frac{1}{D})}}{2S}}$   $b = \sqrt{\frac{1 - \sqrt{1 - 4S(M^2 + \frac{1}{D})}}{2S}}$   $B = \frac{\frac{\partial p}{\partial x}}{(M^2 + \frac{1}{D})}$

$$N_1 = \left[ \frac{-Bb^2 \text{Cosh}[bh]}{a^2 \text{Cosh}[ah] [\text{Cosh}[bh] + \beta b \text{Sinh}[bh]] - b^2 \text{Cosh}[bh] [\text{Cosh}[ah] + \beta a \text{Sinh}[ah]]} \right]$$

$$N_2 = \left[ \frac{Ba^2 \text{Cosh}[ah]}{a^2 \text{Cosh}[ah] [\text{Cosh}[bh] + \beta b \text{Sinh}[bh]] - b^2 \text{Cosh}[bh] [\text{Cosh}[ah] + \beta a \text{Sinh}[ah]]} \right]$$

From equation (5)

$$v = C \text{Sinh}[ay] - D \text{Sinh}[by] \tag{14}$$

where  $C = \frac{BN_3}{a}$   $D = \frac{BN_4}{b}$   $N_3 = \frac{a_1 (b^3 \text{Sinh}[bh]) - (b^2 \text{Cosh}[bh]) (a_2 - a_3)}{a_1^2}$

$$N_4 = \frac{a_1 (a^3 \text{Sinh}[ah]) - (a^2 \text{Cosh}[ah]) (a_2 - a_3)}{a_1^2}$$

$$a_1 = a^2 \text{Cosh}[ah] [\text{Cosh}[bh] + \beta b \text{Sinh}[bh]] - b^2 \text{Cosh}[bh] [\text{Cosh}[ah] + \beta a \text{Sinh}[ah]]$$

$$a_2 = a^2 \text{Cosh}[ah] [b \text{Sinh}[bh] + \beta b^2 \text{Cosh}[bh]] + [\text{Cosh}[bh] + \beta b \text{Sinh}[bh]] [a^3 \text{Sinh}[ah]]$$

$$a_3 = b^2 \text{Cosh}[bh] [a \text{Sinh}[ah] + \beta a^2 \text{Cosh}[ah]] + [\text{Cosh}[ah] + \beta a \text{Sinh}[ah]] [b^3 \text{Sinh}[bh]]$$

**3. Shear Stress, Pressure Gradient and Pressure Rise**

The shear stress at the upper wall  $y = h(x)$ , in the dimensional form is given by:

$$T = \frac{\frac{1}{2} \left[ \frac{\partial u}{\partial y} + \frac{\partial v}{\partial x} \right] \left[ 1 - \left( \frac{dh}{dx} \right)^2 \right] + \left[ \frac{\partial v}{\partial y} - \frac{\partial u}{\partial x} \right] \left( \frac{dh}{dx} \right)}{\left[ 1 + \left( \frac{dh}{dx} \right)^2 \right]}$$

and its solution is given by:

$$\tau = \frac{\left( \frac{E + F}{2} \right) (1 - h'^2) + (G - H) h'}{(1 + h'^2)} \tag{15}$$

Where

$$E = a_4 \text{Sinh}[ay] + a_5 \text{Sinh}[by]$$

$$F = a_6 \left[ \left( \frac{\partial}{\partial x} N_3 \right) \text{Sinh}[ay] \right] - a_7 \left[ \left( \frac{\partial}{\partial x} N_4 \right) \text{Sinh}[by] \right]$$

$$G = a_8 \text{Cosh}[ay] - a_9 \text{Cosh}[by]$$

$$H = -B \left[ \left( \frac{\partial}{\partial x} N_1 \right) \text{Cosh}[ay] \right] + B \left[ \left( \frac{\partial}{\partial x} N_2 \right) \text{Cosh}[by] \right]$$

$$a_4 = -BN_1 a \quad a_5 = BN_2 b \quad a_6 = \frac{B}{a}$$

$$a_7 = \frac{B}{b} \quad a_8 = BN_3 \quad a_9 = BN_4$$

The rate of volume flow 'q' through each section is a constant (independent of both x and t). It is given by:

$$q = \int_0^h u dy = a_{10} \text{Sinh}[bh] - a_{11} \text{Sinh}[ah] - Bh \tag{16}$$

where  $a_{10} = \frac{BN_2}{b}$   $a_{11} = \frac{BN_1}{a}$

Hence the flux at any axial station in the fixed frame is found to be given by:

$$Q(x, t) = \int_0^h (u + 1) dy = q + h \tag{17}$$

while the expression for the time-averaged volumetric flow rate over one period  $T \left( = \frac{\lambda}{c} \right)$  of the peristaltic wave is obtained as:

$$\bar{Q} = \frac{1}{T} \int_0^T Q dt = q + 1 \tag{18}$$

The pressure gradient obtained from equation (18) can be expressed as:

$$\frac{dp}{dx} = \frac{B(\bar{Q} - 1)}{\left[ \frac{N_2}{b} \text{Sinh}[bh] - \frac{N_1}{a} \text{Sinh}[ah] - h \right]} \tag{19}$$

The pressure rise  $\Delta p_L$  (at the wall) in the channel of length L, non-dimensional form is given by:

$$\Delta p = \int_0^1 \frac{dp}{dx} dx$$

$$\Delta p = \int_0^1 \left[ \frac{B(\bar{Q} - 1)}{\left[ \frac{N_2}{b} \text{Sinh}[bh] - \frac{N_1}{a} \text{Sinh}[ah] - h \right]} \right] dx$$

#### 4. Numerical Results and Discussion

The analytical expressions for the axial velocity, transverse velocity, shear stress, pressure gradient and pressure rise are derived in the last section. The numerical

and computational results are discussed through the graphical illustration. Mathematica software is used to find out numerical results. The axial and transverse velocities are shown in the Figures 1 - 4 for various governing parameters, like couple stress parameter (S), porous parameter (D), magnetic field (M) and slip parameter ( $\beta$ ). Figures 1 - 2 reveal the axial velocity distribution (u) decreases by increasing the couple stress parameter (S) with  $\beta \geq 0.2$  for fixed  $D = 10, M = 0.2, dp/dx = 0.5, \varnothing = 0.7, x = t = \pi/4, \lambda = 10, k = 0.0005, a_0 = 0.01$ .

The transverse velocity distribution (v) with couple stress parameter (S) as depicted in figures (3) to (4) with  $\beta \geq 0.2$ . We notice that the transverse velocity increases by increasing the couple stress parameter (S) for fixed  $D = 10, M = 0.2, dp/dx = 0.5, \varnothing = 0.7, x = t = \pi/4, \lambda = 10, k = 0.0005, a_0 = 0.01$ . Figures 5-6 illustrate the variations of  $dp/dx$  with  $\beta$ . It is interesting to note that the pressure gradient decreases by increasing the slip parameter ( $\beta$ ). We observed that through the region  $x \in (0.3, 0.7)$ , i.e., narrowing part of the channel, the flow cannot pass easily. Therefore, it required a large pressure gradient to maintain the same flux to pass it in the narrow part of the channel. Figures 7 and 8 illustrate the influence of time t on pressure gradient  $dp/dx$ . From these Figures, it can be seen that the axial pressure gradient decreases with the increase in time t. It is interesting to note that the pressure gradient is maximum at  $x = 0.3$ . Figures 9 - 10 corresponds to the behavior of the shear stress in a cycle of oscillations at different points of wave length for various governing parameters S, D, M and  $\beta$ . We notice that no separation occurs in the flow field for  $S = 0.2, M = 0.2, D = 10, \beta \geq 0.2, \varnothing = 0.7, \lambda = 10, k = 0.0005, a_0 = 0.01, y = 1.0043$ .

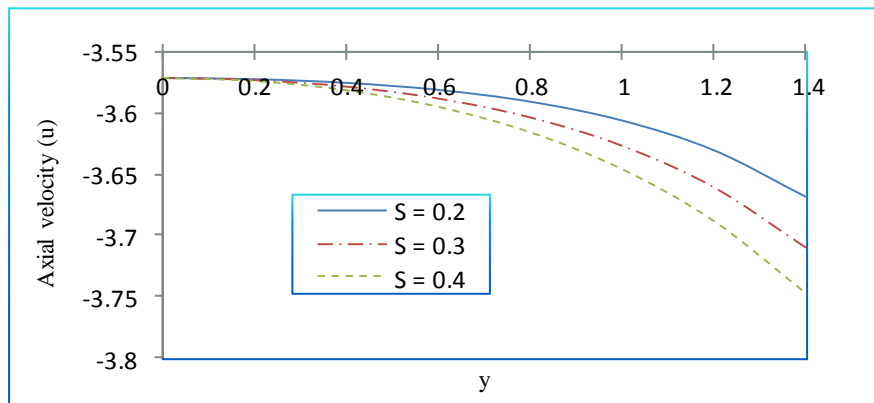


**Figure 1.** Distribution of axial velocity for different values of S with fixed  $D = 10, M = 0.2, \beta = 0.2, dp/dx = 0.5, \varnothing = 0.7, x = t = \pi/4, \lambda = 10, k = 0.0005, a_0 = 0.01$

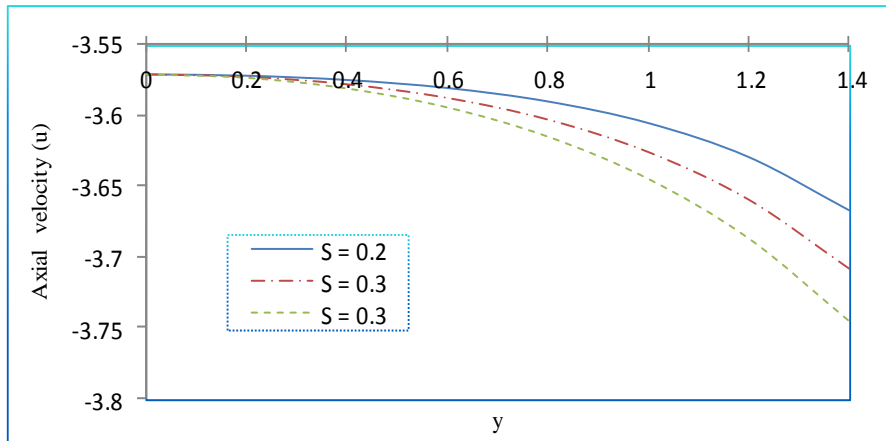


**Figure 2.** Distribution of axial velocity for different values of  $S$  with fixed  $D = 10$ ,  $M = 0.2$ ,  $\beta = 0.3$ ,  $dp/dx = 0.5$ ,  $\varnothing = 0.7$ ,  $x = t = \pi/4$ ,  $\lambda = 10$ ,  $k = 0.0005$ ,  $a_0 = 0.01$

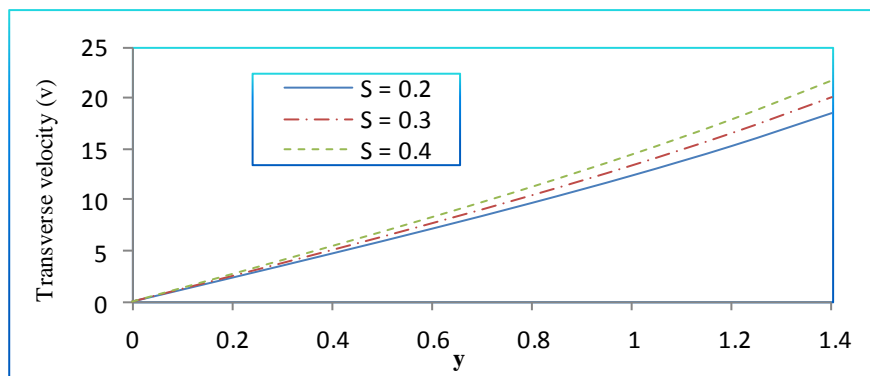


**Figure 3.** Distribution of transverse velocity for different values of  $S$  with fixed  $D = 10$ ,  $M = 0.2$ ,  $\beta = 0.2$ ,  $dp/dx = 0.5$ ,  $\varnothing = 0.7$ ,  $x = t = \pi/4$ ,  $\lambda = 10$ ,  $k = 0.0005$ ,  $a_0 = 0.01$

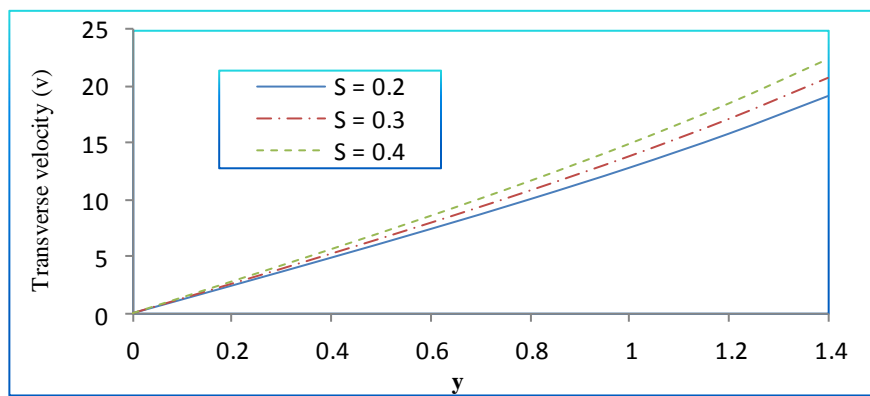


**Figure 4.** Distribution of transverse velocity for different values of  $S$  with fixed  $D = 10$ ,  $M = 0.2$ ,  $\beta = 0.3$ ,  $dp/dx = 0.5$ ,  $\varnothing = 0.7$ ,  $x = t = \pi/4$ ,  $\lambda = 10$ ,  $k = 0.0005$ ,  $a_0 = 0.01$

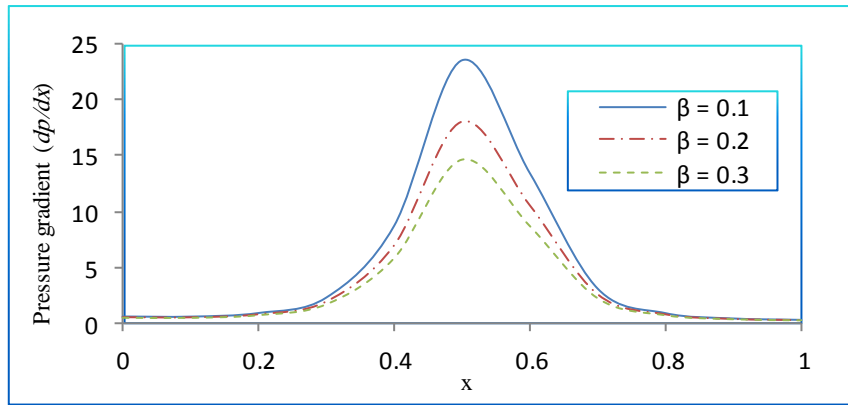


**Figure 5.** Distribution of Pressure gradient versus  $x$  with  $\beta$  for fixed  $D = 10$ ,  $M = 0.1$ ,  $S = 0.2$ ,  $\bar{Q} = 0.2$ ,  $\bar{\varnothing} = 0.7$ ,  $t = \pi/4$ ,  $\lambda = 10$ ,  $k = 0.0005$ ,  $a_0 = 0.01$

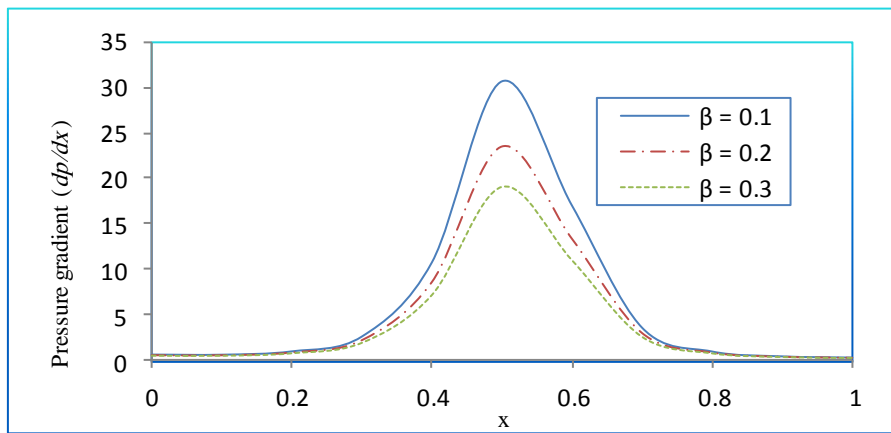


**Figure 6.** Distribution of Pressure gradient versus  $x$  with  $\beta$  for fixed  $D = 10$ ,  $M = 0.1$ ,  $S = 0.3$ ,  $\bar{Q} = 0.2$ ,  $\bar{\varnothing} = 0.7$ ,  $t = \pi/4$ ,  $\lambda = 10$ ,  $k = 0.0005$ ,  $a_0 = 0.01$

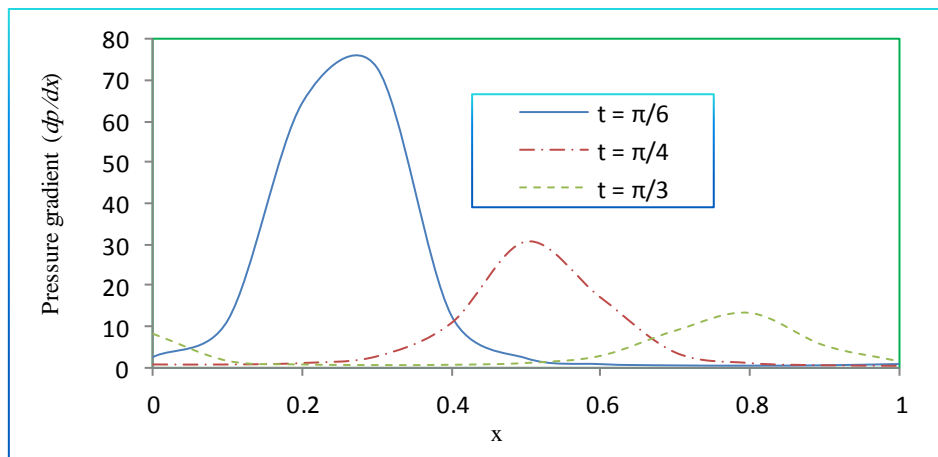


**Figure 7.** Distribution of Pressure gradient versus  $x$  with  $t$  for fixed  $D = 10$ ,  $M = 0.1$ ,  $\beta = 0.1$ ,  $S = 0.3$ ,  $\bar{Q} = 0.2$ ,  $\bar{\varnothing} = 0.7$ ,  $\lambda = 10$ ,  $k = 0.0005$ ,  $a_0 = 0.01$

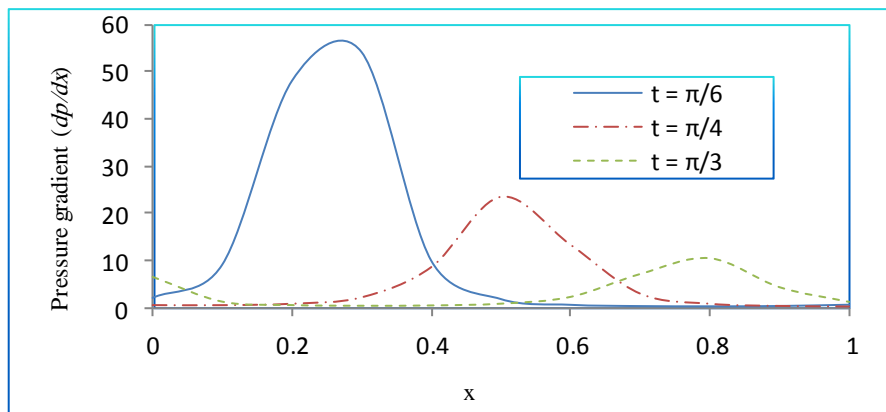


**Figure 8.** Distribution of Pressure gradient versus  $x$  with  $t$  for fixed  $D = 10$ ,  $M = 0.1$ ,  $\beta = 0.2$ ,  $S = 0.3$ ,  $\bar{Q} = 0.2$ ,  $\varnothing = 0.7$ ,  $\lambda = 10$ ,  $k = 0.0005$ ,  $a_0 = 0.01$

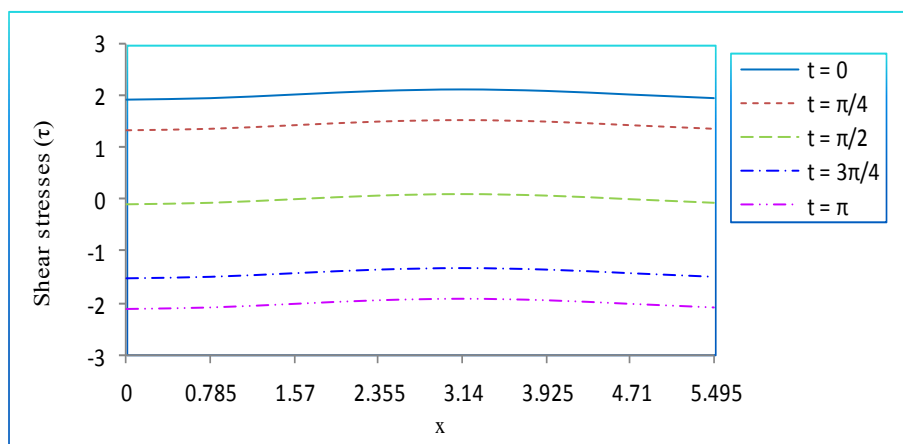


**Figure 9.** Distribution of Shear stresses  $\tau$  for  $S = 0.2$ ,  $M = 0.2$ ,  $D = 10$ ,  $\beta = 0.2$ ,  $\varnothing = 0.7$ ,  $\lambda = 10$ ,  $k = 0.0005$ ,  $a_0 = 0.01$ ,  $y = 1.0043$

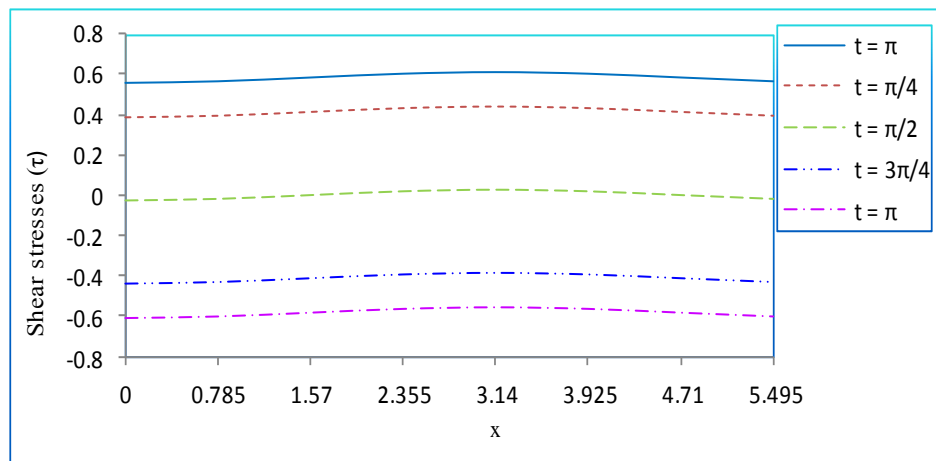


**Figure 10.** Distribution of Shear stresses  $\tau$  for  $S = 0.2$ ,  $M = 0.2$ ,  $D = 10$ ,  $\beta = 0.3$ ,  $\varnothing = 0.7$ ,  $\lambda = 10$ ,  $k = 0.0005$ ,  $a_0 = 0.01$ ,  $y = 1.0043$

#### 4. Conclusions

The effect of the couple stress fluid flow on magnetohydrodynamic peristaltic flow of blood with a uniform porous medium in the presence of slip effect is investigated under the assumption of long wavelength approximation. Moreover, the effect of the various values of parameters on axial velocity, transverse velocity,

pressure gradient and shear stress were computed numerically and explained graphically. We conclude the following observations:

- The axial velocity ( $u$ ) decreases with the increase in the couple stress parameter ( $S$ ) with  $\beta \geq 0.2$  for fixed  $D = 10$ ,  $M = 0.2$ ,  $dp/dx = 0.5$ ,  $\varnothing = 0.7$ ,  $x = t = \pi/4$ ,  $\lambda = 10$ ,  $k = 0.0005$ ,  $a_0 = 0.01$ .
- The transverse velocity ( $v$ ) increases with the increase in the couple stress parameter ( $S$ ) for fixed  $D = 10$ ,  $M =$

$$0.2, dp/dx = 0.5, \varnothing = 0.7, x = t = \pi/4, \lambda = 10, k = 0.0005, a_0 = 0.01.$$

- The axial pressure gradient ( $dp/dx$ ) decreases with the increase in the slip parameter  $\beta$ .
- We notice that the pressure gradient ( $dp/dx$ ) cannot pass easily through the region  $x \in (0.3, 0.7)$ , i.e., the narrowing part of the channel (Figs. 5 and 6).
- The behavior of the shear stress in a cycle of oscillations at different points of wave length for various governing parameters  $S$ ,  $D$ ,  $M$  and  $\beta$ . We notice that no separation occurs in the flow field.

### Acknowledgement

We would like to thank the reviewers and editors for their encouraging comments and constructive suggestions in improving the manuscript of the present study.

### References

- [1] T.W.Lathem, "Fluid motion in a peristaltic pump". Master's thesis, Massachusetts, MIT, Cambridge, 1966.
- [2] S. Srinivas, V. Pushparaj, "Non-linear peristaltic transport in an inclined asymmetric channel". Commun Nonlinear SciNumerSimul. Vol.13 (2008), 1782–1795.
- [3] T.Hayat, M.U.Qureshi, N.Ali, "The influence of slip on the peristaltic motion of a third order fluid in an asymmetric channel". PhysLett A, Vol. 372 (2008), 2653–2664.
- [4] T.Hayat, S.Noreen, N.Ali, "Effect of induced magnetic field on the peristaltic motion of Phan–Thien–Tanner fluid (PTT) fluid". ZNA, Vol. 65a (2010), 665–676.
- [5] M.H.Haroun, "Non-linear peristaltic flow of a fourth grade fluid in an inclined asymmetric channel". Comput Mater Sci., Vol. 39 (2007), 333.
- [6] Kh.S. Mekheimer, Y.A. Elmaboud, "Peristaltic flow of a couple stress fluid in an annulus: application of an endoscope". Physica A, Vol. 387 (2008), 2403–2015.
- [7] M.H.Haroun, "Effect of Deborah number and phase deference on peristaltic transport of a third grade fluid in an asymmetric channel". Commun Nonlinear SciNumerSimul. Vol. 12 (2007), 1464–1480.
- [8] S.Srinivas, M. Kothandapani, "Peristaltic transport in an asymmetric channel with heat transfer - a note". IntCommun Heat and Mass Transf., Vol. 35 (2008), 514–522.
- [9] T.Hayat, N. Alvi, N. Ali, "Peristaltic mechanism of a Maxwell fluid in an asymmetric channel". Nonlinear Anal Real World Appl., Vol. 9 (2008), 1474–1490.
- [10] P. Hariharan, V. Seshadri, R.K.Banerjee, "Peristaltic transport of non-Newtonian fluid in a diverging tube with different wave forms". Math Comput Model, Vol. 48 (2008), 998–1017.
- [11] S. Nadeem, S. Akram, "Peristaltic flow of a Williamson fluid in an asymmetric channel". Commun Nonlinear SciNumerSimul., Vol. 15 (2010), 1705–1716.
- [12] T. Hayat, N. Ali, "Effects of an endoscope on the peristaltic flow of a micro polar fluid". Math Comput Model., Vol. 48 (2008), 721–733.
- [13] K. Vajravelu, S. Sreenadh, V.R. Babu, "Peristaltic pumping of a Herschel–Bulkley fluid in a channel". Appl Math Comput., Vol. 7 (2005) 26– 35.
- [14] Kh.S. Mekheimer, "Peristaltic Flow of a Magneto-Micro polar Fluid: Effect of Induced Magnetic Field". Journal of Applied Mathematics, Article Id 570825 (2008).
- [15] J.C. Misra, S. Chakravarty, "Flow in arteries in the presence of stenosis". Journal of Biomech., Vol. 19 (1986), 907–918.
- [16] J. C. Misra, S. Maiti, G. C. Shit, "Peristaltic Transport of a Physiological Fluid in an Asymmetric Porous Channel in the Presence of an External Magnetic Field". Journal of Mechanics in Medicine and Biology, Vol. 8 (2008), 507–525.
- [17] E.M. Korchevskii, L.S.Marochunik, "Magneto-hydrodynamic version of movements of blood". Biophysics, Vol. 10 (1965), 411–413.
- [18] Ziya Uddin, Manoj Kumari, "MHD Heat and Mass Transfer Free Convection Flow near The Lower Stagnation Point of an Isothermal Cylinder Imbedded in Porous Domain with the Presence of Radiation". Jordan Journal of Mechanical and Industrial Engineering, Vol. 5 (2011) No 5,419-423.
- [19] Boualem Chetti, "Static and Dynamic Analysis of Hydrodynamic Four-lobe Journal Bearing with Couple Stress Lubricants". Jordan Journal of Mechanical and Industrial Engineering, Vol. 5(2011) No 1,23-28
- [20] V.K.Stokes, "Couple stresses in fluids". Phys. Fluids, Vol. 9 (1996), 1709-1715.
- [21] Kh.S. Mekheimer, "Peristaltic transport of a couple stress fluid in a uniform and non-uniform channels". Biorheology, Vol. 39 (2002), 755-765.
- [22] S. Nadeem, S. Akram, "Peristaltic flow of a couple stress fluid under the effect of induced magnetic field in an asymmetric channel". Arch. Appl. Mech., Vol. 81 (2011), 97-109.
- [23] A.M. Sobh, "Interaction of couple stresses and slip flow on peristaltic transport in uniform and non-uniform channels". Turkish J. Eng. Env. Sci., Vol. 32 (2008), 117-123.
- [24] S. Ravikumar, G. Prabhakara Rao, R. Siva Prasad, "Peristaltic flow of a couple stress fluid flows in a flexible channel under an oscillatory flux". Int. J. of Appl. Math and Mech., Vol. 6 (13) (2010), 58-71.
- [25] S. Ravikumar, R. Siva Prasad, "Interaction of pulsatile flow on the peristaltic motion of couple stress fluid through porous medium in a flexible channel". Eur. J. Pure Appl. Math., Vol. 3 (2010), 213-226.
- [26] S. Ravikumar, "Peristaltic fluid flow through magnetic field at low Reynolds Number in a flexible channel under an oscillatory flux". International journal of Mathematical Archive, Vol. 4(1) (2013), 36-52.
- [27] S. Ravikumar, G. PrabhakaraRao, R. Siva Prasad, "Peristaltic flow of a second order fluid in a flexible channel". Int. J. of Appl. Math and Mech., Vol. 6 (18) (2010), 13-32.
- [28] S. Ravikumar, "Peristaltic transportation with effect of magnetic field in a flexible channel under an oscillatory flux". Journal of Global Research in Mathematical Archives, Vol. 1 (2013), 5, 53-62.
- [29] S. Ravikumar, "Hydromagnetic Peristaltic Flow of Blood with Effect of Porous Medium through coaxial vertical Channel: A Theoretical Study". International Journal of Engineering Sciences & Research Technology, Vol. 2 (2013), 10, 2863-2871.
- [30] S. Ravikumar, G. PrabhakaraRao, R. Siva Prasad, "Hydromagnetic two-phase viscous ideal fluid flow in a parallel plate channel under a pulsatile pressure gradient". International Journal of Fluid mechanics Research, Vol. 39 (2012), 4, 291-300.
- [31] S. Ravikumar, Ashfar Ahmed, "Magneto-hydrodynamic couple Stress Peristaltic flow of blood Through Porous medium in a Flexible Channel at low Reynolds number". Online International Interdisciplinary Research Journal, Volume-III, Issue-VI (2013), 157-166.
- [32] W. Kwang-Hua Chu, J. Fang, "Peristaltic Transport in a Slip Flow". European Physical Journal B, Vol. 16 (2000), 543-547.
- [33] B.D. Coleman, H. Markovitz, W. Noll, "Viscometric Flows of Non-Newtonian Fluids". Springer-Verlag, Berlin, Heidelberg, New York, 1966.
- [34] NajmaSaleem, T. Hayat, A. Alsaedi, "Effects of induced magnetic field and slip condition on peristaltic transport with heat and mass transfer in a non-uniform channel".

- International Journal of the Physical Sciences, Vol. 7 (2012), 2, pp. 191 – 204.
- [35] Zaheer Asghar, Nasir Ali, “Peristaltic Transport of Visco-Elasto-Plastic Fluids in a Planar Channel”. Zeitschrift fur Naturforschung A, Vol. 70 (2015) No 8, 593.
- [36] H. Mohammed Kamel, M. Islam Eldesoky, M. Bilal Maher, M. Ramzy, Abumandour, “Slip Effects on Peristaltic Transport of a Particle-Fluid Suspension in a Planar Channel”. Applied Bionics and Biomechanics, Vol. 2015 (2015) Article ID 703574, -14.
- [37] Kh.S. Mekheimer, “Peristaltic Transport of a Couple Stress Fluid in a Uniform and Non-Uniform Channels”. Biorheology, Vol. 39 (2002) 755-765.
- [38] A.M. Shapiro, M.Y. Jaffrin and S.L. Weinberg, “Peristaltic pumping with long wavelengths at low Reynolds number”, J. Fluid Mech., Vol. 37 (1969), 799-825.

# The Effect of Chemical Reaction and Double Stratification on MHD Free Convection in a Micropolar Fluid with Heat Generation and Ohmic Heating

Khilap Singh\* and Manoj Kumar

*Department of Mathematics, Statistics and Computer Science, G.B. Pant University of Agriculture and Technology, Pantnagar, Uttarakhand, India*

Received 28 Jan 2015

Accepted 24 Jul 2015

## Abstract

The present paper deals with the study of flow, heat and mass transfer characteristics of the free convection on a vertical plate in porous media with variable wall temperature and concentration in a doubly stratified and viscous dissipating micropolar fluid in presence of chemical reaction, heat generation and Ohmic heating. A uniform magnetic field is applied normal to the plate. The governing non-linear partial differential equations are transformed into a system of non-linear ordinary differential equations using similarity transformations and, then, solved numerically using the Runge-Kutta-Fehlberg method with a shooting technique. The non-dimensional velocity, microrotation, temperature and concentration are presented graphically for various values of magnetic parameter, coupling number, thermal stratification parameter, solutal stratification parameter and chemical reaction parameter. The skin-friction coefficient, the wall couple stress coefficient, the Nusselt number and the Sherwood number are shown in a tabular form.

© 2015 Jordan Journal of Mechanical and Industrial Engineering. All rights reserved

**Keywords:** *Chemical Reaction, Double Stratification, Natural Convection, MHD, Micropolar Fluids, Porous Media, Heat Generation, Ohmic Heating.*

## 1. Introduction

The study of free convective flow, heat transfer in non-Newtonian fluid in porous media has been an active field of research as it plays an important role in diverse applications, for example, thermal insulation, extraction of crude oil and chemical catalytic reactors, the thermal designing of industrial equipment dealing with molten plastic, polymeric liquids, foodstuffs, etc. Many transport processes occurring both in nature and in industries involve fluid flows with the combined heat and mass transfer. Such flows are driven by the multiple buoyancy effects arising from the density variations caused by the variations in temperature as well as species concentrations. Convective flows in porous media were extensively examined during the last several decades due to many practical applications which can be modeled or approximated as transport phenomena in porous media. Eringen [1-3] introduced the micropolar fluids theory that is capable to describe those fluids by taking into account the effect arising from local structure and micromotions of the fluid element. The mathematical theory of equations of micropolar fluids and applications of these fluids in the

theory and in the theory of porous media are presented by Lukaszewicz [4]. J. Wright and W. Shyy [5] investigated the time-dependent development of convective intrusions in a thermohaline stratification using a composite grid method with local refinement. Ching-Yang Cheng [6,7] studied the effects of thermal stratification and mass stratification on the coupled heat and mass transfer through a vertical wavy plate with constant wall temperature and concentration in porous media saturated with non-Newtonian power law fluids. The thermal and solutal gradients and fluid flow velocities, increasing the thermal and concentration boundary layer thicknesses, and decreasing the dimensionless total heat and mass transfer rates between the fluid and the wall. Moreover, increasing the thermal stratification parameter or concentration stratification parameter leads to a smaller fluctuation of the local Nusselt number and the local Sherwood number with the stream wise coordinate. Srinivasacharya and Ram Reddy [8] analysed the natural convection heat and mass transfer along a vertical plate embedded in a doubly stratified micropolar fluid saturated by non-Darcy porous medium and found that an increase in the both thermal and solutal stratification parameters, the velocity, skin friction parameter and non-dimensional heat and mass transfer

\* Corresponding author. e-mail: : singh.khilap8@gmail.com.

coefficients were decreasing but the wall couple stress was increasing. Ibrahim and Makinde [9] studied the boundary layer analysis for free convection flow in a doubly stratified nanofluid over a vertical plate with uniform surface and mass flux conditions and they got an increase in solutal stratification parameter increases both the local Nusslet number and local Sherwood number. Murthy *et al.* [10] studied the effect of magnetic field on free convection in a thermally stratified non-Darcy porous medium saturated with nanofluid with convective boundary condition. Upendar and Srinivasacharya [11] investigated the flow and heat and mass transfer characteristics of the natural convection on a vertical plate with variable wall temperature and concentration in a doubly stratified MHD micropolar fluid and founded that an increase coupling number reduce velocity but enhance the temperature and concentration distributions. An increase in the magnetic parameter decreases the velocity, skin friction coefficient and heat and mass transfer rates. An increase in the thermal (solutal) stratification parameter reduces the velocity, temperature (concentration), skin friction, heat and mass transfer rates but enhances the concentration (temperature) and wall couple stress. Das [12] investigated the effect of the first order chemical reaction and the thermal radiation on hydro-magnetic free convection heat and mass transfer flow of a micropolar fluid through a porous medium. Naraya *et al.* [13] investigated the effects of Hall current and radiation absorption on MHD free convection mass transfer flow of a micropolar fluid in a rotating frame of reference. Hayat and Qasim [14] investigated the magneto hydrodynamic two-dimensional flow with heat and mass transfer over a stretching sheet in the presence of Joule heating and thermophoresis. Mahmoud and Waheed [15] presented the effect of slip velocity on the flow and heat transfer for an electrically conducting micropolar fluid through a permeable stretching surface with variable heat flux in the presence of heat generation (absorption) and a transverse magnetic field. They found that the local Nusselt number decreased as the heat generation parameter is increased with an increase in the absolute value of the heat absorption parameter. Bataller [16] proposed the effects of viscous dissipation, work due to deformation, internal heat generation (absorption) and thermal radiation. It was shown that internal heat generation/absorption enhances or damps the heat transformation. Ravikumar *et al.* [17] studied unsteady, two-dimensional, laminar, boundary-layer flow of a viscous, incompressible, electrically conducting and heat-absorbing, Rivlin–Erickson flow fluid along a semi-infinite vertical permeable moving plate in the presence of a uniform transverse magnetic field and thermal buoyancy effect. They observed that the heat absorption coefficient increase results in a decrease in the velocity and temperature. Chien-Hsin Chen [18] presented the problem of combined heat and mass transfer in buoyancy-induced MHD natural convection flow of an electrically conducting fluid along a vertical plate is investigated with Ohmic and viscous heating. Narayana and Sravanthi [19] studied the simultaneous effects of

soret and ohmic heating on MHD free convective heat and mass transfer flow for a micro polar fluid bounded by a vertical infinite surface. Kumar [20] analysed the problem of MHD mixed convective flow of a micropolar fluid with the effect of Ohmic heating, radiation and viscous dissipation over a chemically reacting porous plate with constant heat flux. Tamayol and Bahrami [21] reported that porous materials can be used to enhance the heat transfer rate from stretching surfaces to improve processes such as hot rolling and composite fabrication. Sharma and Gupta [22] studied the effect of medium permeability on thermal convection in micropolar fluids and found that the presence of coupling between thermal and micropolar effects may introduce oscillatory motions in the system.

By the same token, Raptis [23] investigated the boundary layer flow of a micropolar fluid through a porous medium. The unsteady MHD boundary layer flow of a micropolar fluid near the stagnation point of a two-dimensional plane surface through a porous medium was studied by Nadeem *et al.* [24]. Rashad [25] proposed the effect of thermal radiation with a regular three-parameter perturbation analysis in some free convection flows of Newtonian fluid in saturated porous medium. El-Aziz [26] studied the unsteady mixed convection flow of a viscous incompressible micropolar through a heated vertical surface in the presence of viscous dissipation and buoyancy force. El-Hakim [27] presented an analysis for the effect of thermal dispersion, viscous and Joule heating on the flow of an electrically conducting and viscous incompressible micropolar fluid past a semi-infinite plate whose temperature varies linearly with the distance from the leading edge in the presence of uniform transverse magnetic field. The skin friction factor and the rate of heat transfer decrease with the magnetic parameter and the micropolar parameter and they increase with the thermal dispersion parameter increase. Oahimire and Olajuwon [28] studied heat and mass transfer effects on an unsteady flow of a chemically reacting MHD micropolar fluid through an infinite vertical porous plate in porous medium with hall effect and thermal radiation. Hussain *et al.* [29] reported on the radiation effects on the unsteady boundary layer flow of a micropolar fluid over a stretching sheet. The sheet is considered to be permeable and the problem is non-dimensionalized by using similarity transformations. They found that temperature increases for radiation parameter, however it decreases for stagnation point.

The aim of the present work is to investigate the effects of transverse magnetic field, thermal and solutal stratification on the MHD free convection heat and mass transfer from a vertical plate embedded in micropolar fluid in porous medium with viscous dissipation, heat generation and Ohmic heating. The equations thus obtained were solved numerically using Runge–Kutta–Fehlberg fourth fifth order method with shooting technique. The effects of different parameters on velocity, microrotation, temperature and concentration are presented graphically. The skin friction coefficient, wall couple stress coefficient, Nusselt number and Sherwood number are tabulated.

## 2. Mathematical formulation

The graphical model of the problem is given along with the flow configuration and coordinate system, Figure 1. The system deals with a steady, laminar, incompressible, two-dimensional free convective heat and mass transfer along a semi-infinite vertical plate in porous media embedded in a doubly stratified, electrically conducting micropolar fluid. The heat generation, as well as viscous dissipation and Ohmic heating terms, was retained in the energy equation. Choosing the coordinate system, such that  $x$  axis, is along the vertical plate and  $y$  axis normal to the plate. The plate is maintained at temperature  $T_w(x)$  and concentration  $C_w(x)$ . The temperature and the mass concentration of the ambient fluid are assumed to be linearly stratified in the form  $T_\infty(x) = T_{\infty,0} + A_1 x$  and  $C_\infty(x) = C_{\infty,0} + B_1 x$ , respectively, where  $A_1$  and  $B_1$  are constants and varied to alter the intensity of stratification in the medium and  $T_{\infty,0}$  and  $C_{\infty,0}$  are the beginning ambient temperature and concentration at  $x = 0$ , respectively. A uniform magnetic field of magnitude  $B_0$  is applied normal to the plate. The magnetic Reynolds number is assumed to be small so that the induced magnetic field can be neglected in comparison with the applied magnetic field; neglecting the Hall current effect, electrically non-conducting wall, local thermal equilibrium between fluid and solid.

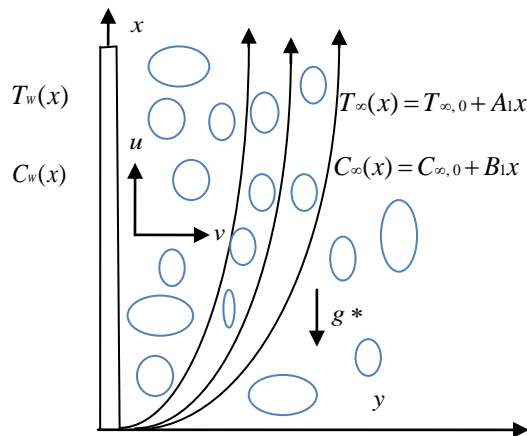


Figure 1. Physical model and coordinate

Using the Boussinesq boundary layer approximations, the governing equations for the micropolar fluid are given by:

$$u \frac{\partial u}{\partial x} + v \frac{\partial v}{\partial y} = 0 \tag{1}$$

$$u \frac{\partial u}{\partial x} + v \frac{\partial u}{\partial y} = \left( \frac{\mu + \kappa}{\rho} \right) \frac{\partial^2 u}{\partial y^2} + \frac{\kappa}{\rho} \frac{\partial \omega}{\partial y} + g^* (B_T (T - T_\infty) + B_C (C - C_\infty)) - \frac{\sigma B_0^2}{\rho} u + \frac{\mu \varepsilon}{\rho k_1} u \tag{2}$$

$$u \frac{\partial \omega}{\partial x} + v \frac{\partial \omega}{\partial y} = \frac{\gamma}{\rho j} \frac{\partial^2 \omega}{\partial y^2} - \frac{\kappa}{\rho j} \left( 2\omega + \frac{\partial u}{\partial y} \right) \tag{3}$$

$$u \frac{\partial T}{\partial x} + v \frac{\partial T}{\partial y} = \alpha \frac{\partial^2 T}{\partial y^2} + \frac{(\mu + \kappa)}{\rho c_p} \left( \frac{\partial u}{\partial y} \right)^2 + \frac{\sigma B_0^2}{\rho c_p} u^2 + \frac{\theta_0}{\rho c_p} (T - T_\infty) \tag{4}$$

$$u \frac{\partial C}{\partial x} + v \frac{\partial C}{\partial y} = D \frac{\partial^2 C}{\partial y^2} - R_r (C - C_\infty) \tag{5}$$

where  $u$  and  $v$  are the component of velocity along  $x$  and  $y$  directions, respectively,  $\omega$  is the component of microrotation whose direction of rotation lies in the  $xy$  - plane,  $g^*$  is the gravitational acceleration,  $\rho$  is fluid density,  $T$  is the temperature,  $C$  is the concentration,  $B_T$  is the coefficient of thermal expansions,  $B_C$  is the coefficient of solutal expansions,  $B_o$  is the coefficient of the magnetic field,  $\varepsilon$  is porosity of porous media,  $k_1$  is permeability of porous media,  $\mu$  is the dynamic coefficient of viscosity of the fluid,  $\kappa$  is the vortex viscosity,  $j$  is the micro-inertia density,  $\gamma$  is the spin-gradient viscosity,  $\sigma$  is the magnetic permeability of the fluid,  $\nu$  is the kinematic viscosity,  $\alpha$  is the thermal diffusivity,  $k$  is the thermal conductivity of the fluid and  $D$  is the molecular diffusivity,  $C_p$  is the specific heat,  $\theta_0$  is the internal heating,  $R_r$  is the chemical reaction rate constant.

The boundary conditions are:

$$\begin{aligned} \text{at } y = 0 \quad & u = 0, \quad v = 0, \quad \omega = 0, \\ & T = T_w(x), \quad C = C_w(x), \\ \text{as } y \rightarrow \infty \quad & u \rightarrow 0, \quad \omega \rightarrow 0, \\ & T \rightarrow T_\infty(x), \quad C \rightarrow C_\infty(x) \end{aligned} \tag{6}$$

where the subscripts  $w$  and  $\infty$  indicate the conditions at wall and at the outer edge of the boundary layer, respectively.

The continuity equation (1) is satisfied by introducing the stream function  $\psi$  such that

$$u = \frac{\partial \psi}{\partial y}, \quad v = -\frac{\partial \psi}{\partial x} \tag{7}$$

Equations 2, 3, 4 and 5 can be transformed into a set of nonlinear ordinary differential equations by using the following similarity variables:

$$\psi = A x f(\eta),$$

$$\eta = B y,$$

$$\omega = E x g(\eta)$$

$$\theta(\eta) = \frac{T - T_{\infty,0}}{\Delta T} - \frac{A_1 x}{\Delta T}, \tag{8}$$

$$\Delta T = T_w(x) - T_{\infty,0} = M_1(x)$$

$$\Delta C = \frac{C - C_{\infty,0}}{\Delta C} - \frac{B_1 x}{\Delta C},$$

$$\Delta C = C_w(x) - C_{\infty,0} = N_1(x)$$

where the constants  $A$ ,  $B$ ,  $E$ ,  $M_1$  and  $N_1$  have, respectively, the dimension of velocity, reciprocal of length, the reciprocal of the product of length and time, the ratio of temperature and length and the ratio of concentration and length.

The transformed ordinary differential equations are:

$$\left( \frac{1}{1-N} \right) f''' + f f'' + \left( \frac{N}{1-N} \right) g' - (f')^2 + \theta + L\theta - M f' + \Lambda f' = 0 \tag{9}$$

$$\lambda g'' - \left( \frac{N}{1-N} \right) \varepsilon (2g + f'') + f g' - f' g = 0 \tag{10}$$

$$\frac{1}{Pr} \theta'' + f\theta' - f'\theta + H\theta + MEcf'^2 + \left(\frac{1}{1-N}\right) Ec f''^2 - \varepsilon_1 f' = 0 \tag{11}$$

$$\frac{1}{Sc} \phi'' + f\phi' - f'\phi - R\phi - \varepsilon_2 \phi = 0 \tag{12}$$

where primes denotes differentiation with respect to similarity variable  $\eta$ ,  $Pr = \nu/\alpha$  is Prandtl number,  $Sc = \nu/D$  is the Schmidt number,  $\xi = I/(j b^2)$  is the micro-inertia density,  $N = \kappa/\mu + \kappa$  ( $0 \leq N < 1$ ) is the Coupling number,  $\lambda = \gamma/j\rho\nu$  is the spin – gradient viscosity,  $L = \frac{B_c \Delta C}{B_T \Delta B}$  is the buoyancy parameter,  $M = \frac{\sigma B_0^2}{\mu B^2}$  is the magnetic field parameter,  $\Lambda = \frac{\varepsilon}{k_1 B^2}$  is the porous parameter,  $H = \frac{\theta_0}{\mu C_p B^2}$  is the heat generation parameter,  $Ec = \frac{(\nu x B^2)^2}{C_p \Delta T}$  is the Eckert number,  $R = \frac{R_r}{\nu B^2}$  is the chemical reaction parameter,  $\varepsilon_1 = \frac{x}{\Delta T} \frac{d}{dx} [T_\infty(x)]$  is the thermal stratification parameter and  $\varepsilon_2 = \frac{x}{\Delta C} \frac{d}{dx} [C_\infty(x)]$  is the solutal stratification parameter.

The boundary conditions (6) in terms of  $f, g, \theta$  and  $\phi$  become:

$$\begin{aligned} \text{at } \eta=0 \quad & f(0) = 0, f'(0) = 0, g(0) = 0, \\ & \theta(0) = 1 - \varepsilon_1, \phi(0) = 1 - \varepsilon_2 \\ \text{as } \eta \rightarrow \infty \quad & f(\infty) \rightarrow 0, g(\infty) \rightarrow 0, \theta(\infty) \rightarrow 0, \\ & \phi(\infty) \rightarrow 0 \end{aligned} \tag{13}$$

The physical parameters of interest are the skin friction coefficient  $C_f$ , the Couple stress coefficient  $M_w$ , the local Nusselt number  $Nu_x$  and the Sherwood number  $Sh$  which are defined as

$$C_f = \frac{2\tau_w}{\rho A^2}, \quad M_w = \frac{B}{\rho A^2} m_w, \quad Nu_x = \frac{q_w}{B k (T_w - T_\infty)} \tag{14}$$

and  $Sh = \frac{q_m}{D B [C_w - C_\infty]}$

Where  $\tau_w, m_w, q_w$  and  $q_m$  are the wall shear stress, the wall couple stress, the wall heat flux and the wall mass flux, respectively, are given by:

$$\begin{aligned} \tau_w &= \left[ (\mu + \kappa) \left( \frac{\partial u}{\partial y} \right) + \kappa \omega \right]_{y=0}, \quad m_w = \gamma \left( \frac{\partial \omega}{\partial y} \right)_{y=0}, \\ q_w &= -k \left( \frac{\partial T}{\partial y} \right)_{y=0} \quad \text{and} \quad q_m = -D \left( \frac{\partial C}{\partial y} \right)_{y=0} \end{aligned} \tag{15}$$

Hence using (8), we get:

$$C_f = \left( \frac{2}{1-N} \right) f''(0) \bar{x}, \quad M_w = \frac{\lambda}{\xi} g'(0) \bar{x}, \tag{16}$$

$$Nu_x = -\theta'(0) \quad \text{and} \quad Sh = -\phi'(0)$$

where  $\bar{x} = B x$ .

### 3. Method of Solution

The non-linear ordinary differential equations (9)-(12) subject to the boundary condition (13) were solved using the Runge-Kutta-Fehlbe fourth fifth order method along with shooting technique. This method is based on the discretization of the problem domain and the calculation of unknown boundary conditions. The domain of the problem is discredited and the boundary conditions for  $\eta_\infty$  are replaced by  $f'(\eta_\infty) = 0, g(\eta_\infty) = 0, \theta(\eta_\infty) = 0,$  and  $\phi(\eta_\infty) = 0$ , where  $\eta_\infty$  is sufficiently large value of  $\eta$  at which boundary conditions (13) for  $f(\eta)$  are satisfied. We ran the computer code written in MATLAB for  $\eta_\infty = 4$  and step size  $\Delta\eta = 0.01$ . To solve the problem the non-linear equations, (9) - (12) were converted into nine first orders linear ordinary differential equations. There are five conditions at boundary  $\eta = 0$  and four conditions at boundary  $\eta = \infty$ . To find the solution of the problem, one will need four more conditions  $f''(0), g'(0), \theta'(0)$  and  $\phi'(0)$  at  $\eta = 0$ . These conditions were found by the shooting technique. Finally, the problem was solved by the Runge-Kutta-Fehlberg fourth fifth method along with calculated boundary conditions.

### 4. Results and discussion

In order to study the effects of the coupling number  $N$ , magnetic field parameter  $M$ , thermal stratification parameter  $\varepsilon_1$ , solutal stratification parameter  $\varepsilon_2$  and chemical reaction parameter  $R$  on the physical quantities of the flow, the other parameters were fixed as  $Ec = 0.01, H = 0.2, \Lambda = 0.3, L = 1, Pr = 1, Sc = 0.2, \lambda = 1$  and  $\xi = 0.1$ . The values of micropolar parameter  $\lambda$  and  $\xi$  were chosen so as to satisfy the thermodynamic restrictions on the material parameters given by Eringen [1].

To validate the results obtained, the authors compared the results in the absence porous parameter  $\Lambda$ , heat generation parameter  $H$ , Eckert number  $Ec$ , chemical reaction parameter  $R$  with reported by Srinivasacharya and Upendar [11] and found that they were in good agreement, as shown in Table1.

The non-dimensional velocity, microrotation, temperature and concentration profiles for various values of magnetic parameter  $M$  are illustrated in Figures 2-5 with  $N=0.5, \varepsilon_1 = 0.1, \varepsilon_2 = 0.2$  and  $R = 0.3$ . It is depicted from Figure 2 that the velocity decreases as the magnetic parameter ( $M$ ) increases. This is due to the transverse magnetic field, normal to the flow direction, has a tendency to generate the drag known as the Lorentz force which tends to resist the flow. Hence, the horizontal velocity decreases as the magnetic parameter  $M$  increases. Figure 3 depicts that the microrotation component increases near the plate and decreases far away from the plate for increasing values of  $M$ . It is clear from Figure 4 that the temperature increases with the increasing values of magnetic parameter. The transverse magnetic field gives rise to a resistive force known as the Lorentz force of an electrically conducting fluid. This force makes the fluid experience a resistance by increasing the friction between its layers and so increases its temperature and concentration.

**Table 1.** Comparison between  $f''(0)$  and  $-\theta'(0)$  calculated by the present method and Ref. [11] for  $A = R = H = Ec = 0, Pr = 1$  and  $Sc = 0.2$

N	M	$\epsilon_1$	$\epsilon_2$	Ref. [11]		Present	
				$f''(0)$	$-\theta'(0)$	$f''(0)$	$-\theta'(0)$
0.0	1.0	1.0	2.0	0.97648	0.62178	0.97649	0.62178
0.3	1.0	1.0	2.0	0.78120	0.58833	0.78120	0.58833
0.5	2.0	1.0	2.0	0.55448	0.51043	0.55449	0.51042
0.5	1.0	2.0	2.0	0.59187	0.52654	0.59187	0.52653
0.5	1.0	1.0	4.0	0.55160	0.52112	0.55161	0.52111

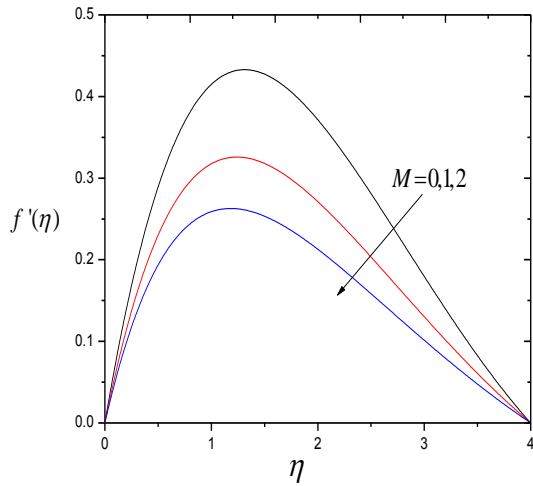


**Figure 2.** Velocity profile for various values of magnetic parameter M.

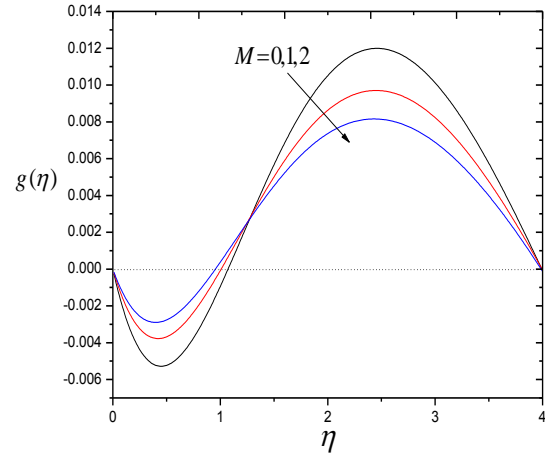


**Figure 3.** Microrotation profile for various values of magnetic parameter M.

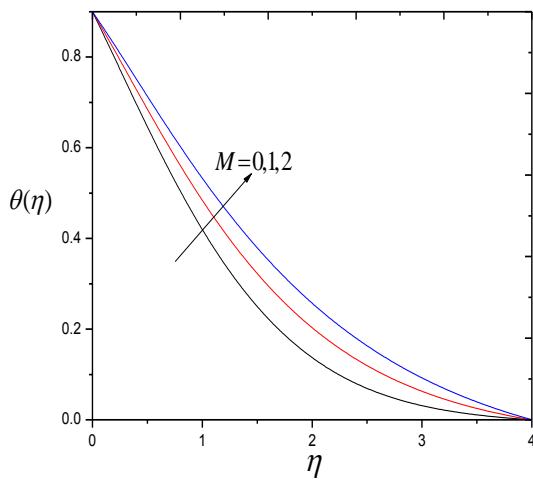


**Figure 4.** Temperature profile for various values of magnetic parameter M.

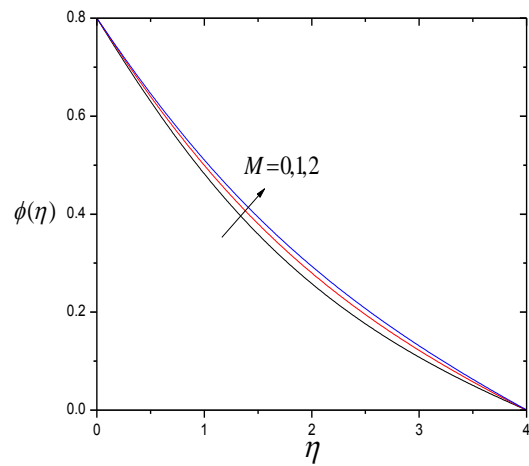


**Figure 5.** Concentration profile for various values of magnetic parameter M

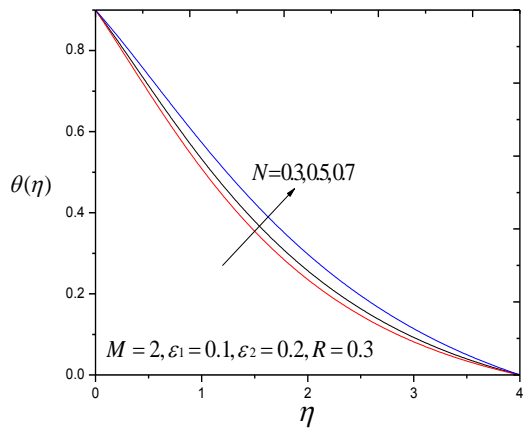


**Figure 8.** Temperature profile for various values of coupling number  $N$ .

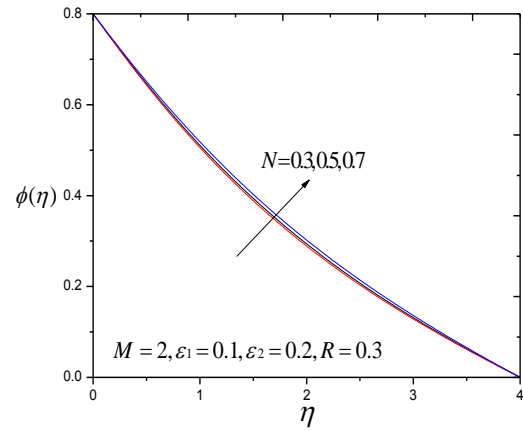


**Figure 9.** Concentration profile for various values of coupling number  $N$ .

Figures 10-13 depict the variation of thermal stratification parameter  $\epsilon_1$  on the non-dimensional velocity, microrotation, temperature and concentration with  $M = 2$ ,  $N = 0.5$ ,  $\epsilon_2 = 0.2$  and  $R = 0.3$ . It is seen from Figure 10 that the velocity decreases with the increasing value of thermal stratification  $\epsilon_1$ . This is because the thermal stratification reduces the effective convective potential between the heated plate and the ambient fluid in the medium. Hence, the thermal stratification effect reduces the velocity in the boundary layer. It is noticed from Figure 11 that the values of microrotation changes sign from negative to positive within boundary layer. Also, it is observed that the

magnitude of the microrotation increases with the increasing value of thermal stratification parameter  $\epsilon_1$ . Figure 12 demonstrates that the non-dimensional temperature of the fluid decrease with the increasing value of thermal stratification parameter. When the thermal stratification effect is taken into consideration, the effective temperature difference between the plate and the free boundary fluid will decrease; hence, the thermal boundary layer is thickened and the temperature is reduced. It is observed from Figure 13 that the concentration of the fluid increases with the increasing value of the thermal stratification parameter.

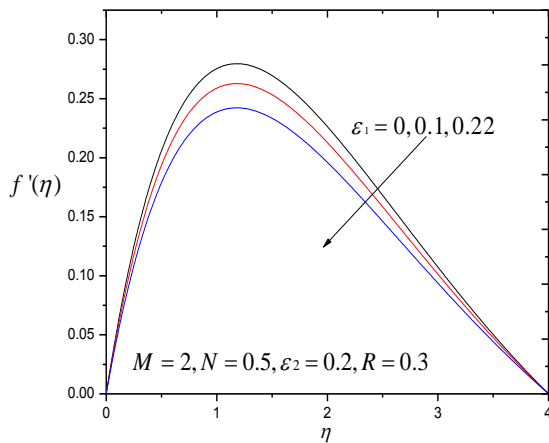


**Figure 10.** Velocity profile for various values of thermal stratification parameter  $\epsilon_1$ .

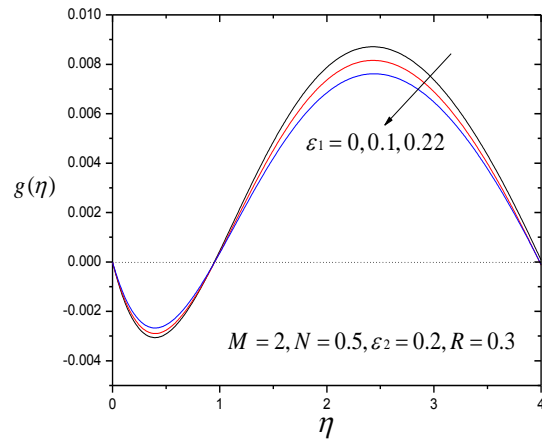


**Figure 11.** Microrotation profile for various values of thermal stratification parameter  $\epsilon_1$ .

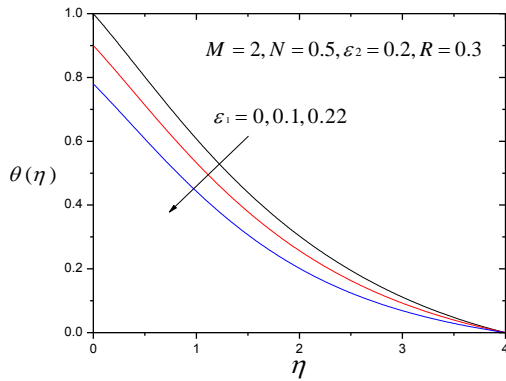


**Figure 12.** Temperature profile for various values of thermal stratification parameter  $\epsilon_1$ .

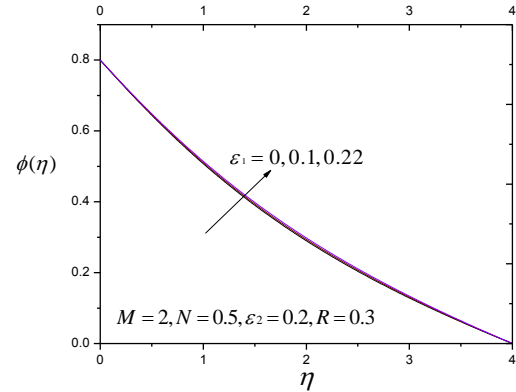


**Figure 13.** Concentration profile for various values of thermal stratification parameter  $\epsilon_1$ .

The effect of the solutal stratification parameter on the non-dimensional velocity component, microrotation, temperature, and concentration is shown in Figures 14-17 with  $M = 2, N = 0.5, \epsilon_1 = 0.1$  and  $R = 0.3$ . It is clear from Figure 14 that the velocity of the fluid decreases with the increase in the solutal stratification parameter. It is noticed from Figure 15 that the microrotation values changed from negative to positive within the boundary layer. Also,

it is observed that the magnitude of the microrotation increases with the increase in the solutal stratification parameter. From Figure 16, we observe that the temperature increases with the increasing value of solutal stratification parameter. It is seen from Figure 17 that the concentration of the fluid decreases with the increase of the thermal stratification parameter.

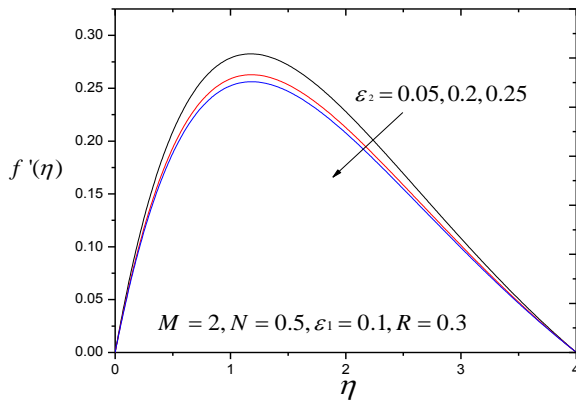


**Figure 14.** Velocity profile for various values of solutal stratification parameter  $\epsilon_2$ .

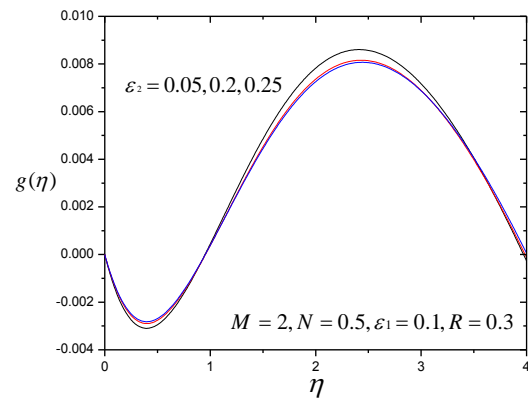


**Figure 15.** Microrotation profile for various values of solutal stratification parameter  $\epsilon_2$ .

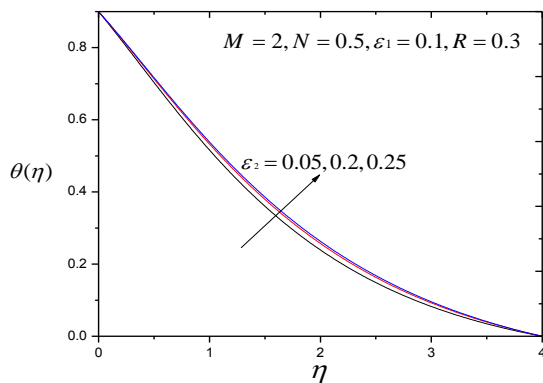


**Figure 16.** Temperature profile for various values of solutal stratification parameter  $\epsilon_2$ .

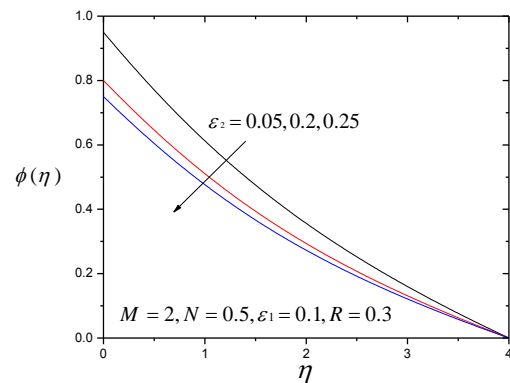


**Figure 17.** Concentration profile for various values of solutal stratification parameter  $\epsilon_2$ .

The effect of the chemical reaction parameter on the non-dimensional velocity component, microrotation, temperature, and concentration with  $M = 2$ ,  $N = 0.5$ ,  $\varepsilon_1 = 0.1$  and  $\varepsilon_2 = 0.2$  are depicted in Figures 18-21. It is clear from Figure 18 that the velocity of the fluid decreases with increasing value of chemical reaction parameter  $R$ . It is seen from Figure 19 that the microrotation values changed from negative to positive within the boundary layer. Also, it is clear that the magnitude of the microrotation increases with an increase in the chemical reaction parameter  $R$ . From Figure 20, we observed that temperature increases with the increasing value of the chemical reaction parameter  $R$ . It is noticed from Figure 21 that the concentration of the fluid decreases with the increasing values of the chemical reaction parameter  $R$ .

Table 2 shows the effects of the magnetic parameter  $M$ , coupling number  $N$ , thermal stratification parameter  $\varepsilon_1$ , solutal stratification parameter  $\varepsilon_2$  and chemical reaction parameter  $R$  on the skin friction coefficient  $C_f$ , couple stress coefficient  $M_w$ , local Nusselt number  $Nu$  and Sherwood number  $Sh$ . It is clear from this table that the

skin friction, Nusselt number and Sherwood number decrease and the wall couple stress increases as  $M$  increases. It demonstrates that the skin friction coefficient, Nusselt number, Sherwood number and wall couple stress decrease with the increasing value of the coupling number  $N$ . For increasing the value of  $N$ , the effect of microstructure becomes significant; hence, the wall couple stress decreases. The effect of the thermal stratification parameter  $\varepsilon_1$  is to decrease the skin friction coefficient, Nusselt number and Sherwood number whereas it increases the wall couple stress. It is seen that the skin friction coefficient, Nusselt number and Sherwood number decrease and the wall couple stress increases as  $\varepsilon_2$  increases. The skin friction coefficient decreases and the wall couple stress increases with the increasing value of the chemical reaction parameter  $R$ , and it is interesting to note that the opposite situation occurs in the case of heat and mass transfer coefficient, i.e., the Nusselt number decreases whereas the Sherwood number increases as the chemical reaction parameter  $R$  increases.

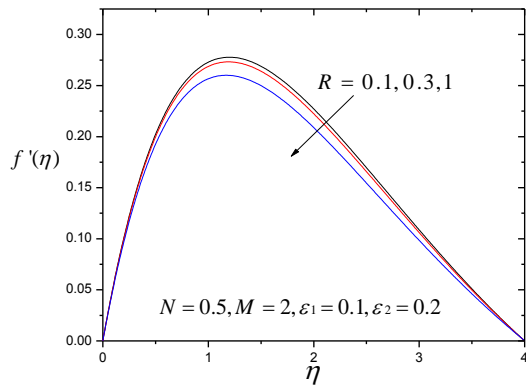


Figure 18. Velocity profile for various values of chemical reaction parameter  $R$

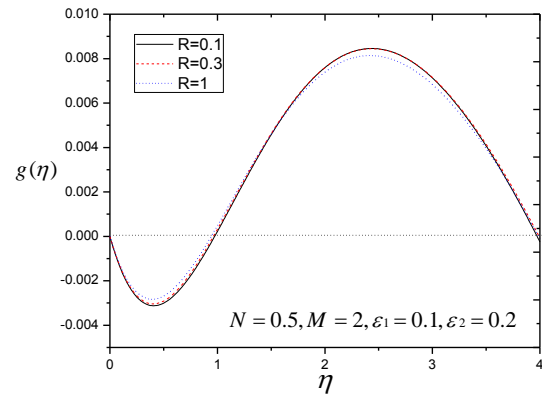


Figure 19. Micro rotation profile for various values of chemical reaction parameter  $R$ .

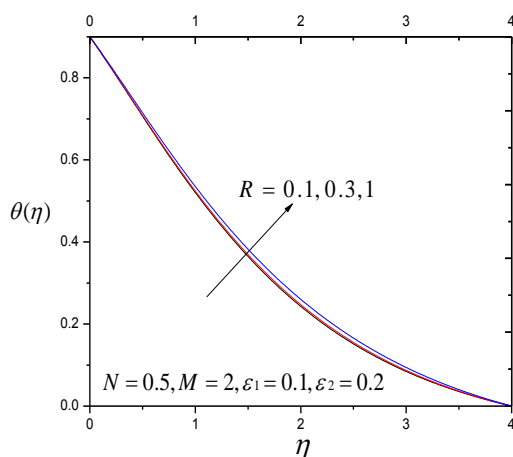


Figure 20. Temperature profile for various values of chemical reaction parameter  $R$ .

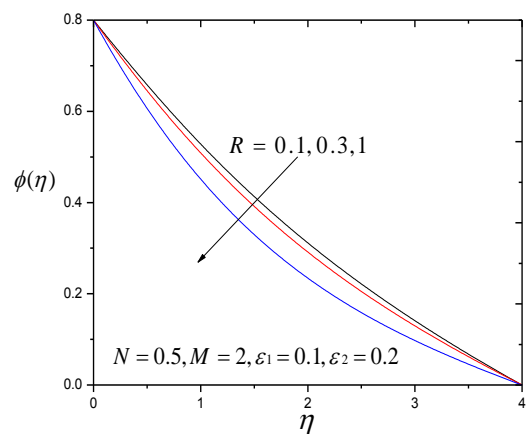


Figure 21. Concentration profile for various values of chemical reaction parameter  $R$ .

**Table 2.** Values of  $f''(0)$ ,  $-\theta'(0)$ ,  $Nu$  and  $Sh$  for various values of  $M$ ,  $N$ ,  $\varepsilon_1$ ,  $\varepsilon_2$ , and  $R$ .

$M$	$N$	$\varepsilon_1$	$\varepsilon_2$	$R$	$f''(0)$	$-\theta'(0)$	$Nu$	$Sh$
0	0.5	0.1	0.2	0.3	0.77428	0.02626	0.49192	0.35622
1	0.5	0.1	0.2	0.3	0.64684	0.02016	0.40952	0.33552
2	0.3	0.1	0.2	0.3	0.70211	0.00760	0.38490	0.38490
2	0.5	0.1	0.2	0.3	0.56721	0.01646	0.34932	0.32250
2	0.7	0.1	0.2	0.3	0.40492	0.03242	0.29280	0.31185
2	0.5	0.0	0.2	0.3	0.60251	0.01745	0.36882	0.32630
2	0.5	0.22	0.2	0.3	0.52459	0.01520	0.32585	0.31800
2	0.5	0.1	0.05	0.3	0.61349	0.01770	0.37095	0.37530
2	0.5	0.1	0.25	0.3	0.55174	0.01602	0.34199	0.30496
2	0.5	0.1	0.2	0.1	0.58597	0.01738	0.36440	0.29162
2	0.5	0.1	0.2	1.0	0.56535	0.01626	0.34655	0.42755

## 5. Conclusions

Free convection heat and mass transfer in an electronically conducting and viscous dissipating micropolar fluid over a vertical plate with magnetic, thermal and solutal stratification and chemical reaction effects are considered. The non-linear partial differential equations are transformed into a system of coupled non-linear ordinary differential equations by using similarity variables and then solved numerically using the Runge-Kutta fourth-fifth order method along with the shooting method. From the numerical calculations of the skin friction coefficient, couple stress coefficient, Nusselt number and Sherwood number it is concluded that:

- An increase in magnetic parameter decreases the velocity, skin friction coefficient, heat and mass transfer rates but enhances the temperature, concentration and wall couple stress.
- An increase in the coupling number decreases the velocity, skin friction coefficient, couple stress coefficient, heat and mass transfer rates but increases the temperature and concentration distributions.
- The higher value of the thermal (solutal) stratification parameter results in lower velocity, temperature (concentration), skin friction and heat and mass transfer rate but higher concentration (temperature) and wall couple stress.
- It is also found that the microrotation changes sign from negative to positive values within the boundary layer in the presence of stratification.
- An increase in the chemical reaction parameter decreases the velocity, concentration, skin friction coefficient and heat transfer rate but enhances the temperature, wall couple stress and mass transfer rate.

## References

- [1] A. C. Eringen, "Theory of micropolar fluid". Jour of mathematics and Mechanics, Vol. 16 (1966), 1-18.
- [2] A. C. Eringen, "Theory of Thermomicrofluids". Journal of mathematical analysis and application, Vol. 38 (1972), 480 – 496.
- [3] A. C. Eringen, "Simple micropolar fluids". International Journal of Engineering Science, Vol. 2 (1964), 205-217.
- [4] Lukaszewicz G. Micropolar fluids: theory and application. Basel: Birkhäuser; 1999.
- [5] J. Wright, W. Shyy, "Numerical simulation of unsteady convective intrusions in thermohaline stratification". Int. J. Heat Mass Transfer, Vol. 39 (1996), 1183-1201.
- [6] Ching-Yang Cheng, "Combined heat and mass transfer in natural convection flow from a vertical wavy surface in a power-law fluid saturated porous medium with thermal and mass stratification". International Communications in Heat and Mass Transfer, Vol. 36 (2009), 351–356.
- [7] Ching-Yang Cheng, "Double-diffusive natural convection along a vertical wavy truncated cone in non-Newtonian fluid saturated porous media with thermal and mass stratification". Int Communications in Heat and Mass Transfer, Vol. 35 (2008), 985–990.
- [8] D. Srinivasacharya, C. RamReddy, "Heat and mass transfer by natural convection in a doubly stratified non-Darcy micropolar fluid". International Communications in Heat and Mass Transfer, Vol. 37 (2010), 873–880.
- [9] W. Ibrahim, O.D. Makinde, "The effect of double stratification on boundary-layer flow and heat transfer of nanofluid over a vertical plate". Computers & Fluids, Vol. 86 (2013), 433–441.
- [10] P.V.S.N Murthy, Ch. Ram Reddy, A.J. Chamkha, A.M. Rashad, "Magnetic effect on thermally stratified nanofluid saturated non-Darcy porous medium under convective boundary condition". International Communications in Heat and Mass Transfer, Vol. 47 (2013), 41–48.
- [11] D. Srinivasacharya, M. Upendar, "Effect of double stratification on MHD free convection in a micropolar fluid". Journal of the Egyptian Mathematical Society, Vol. 21 (2013), 370–378.
- [12] K. Das, "Effect of chemical reaction and thermal radiation on heat and mass transfer flow of MHD micropolar fluid in a rotating frame of reference". Int Jour of Heat and Mass Transfer, Vol. 54 (2001), 3505-3513.
- [13] Satya Narayan P.V, Venkateswarlu B, Venkataramana S, Effects of Hall current and radiation absorption on MHD micropolar fluid in a rotating system, Ain Shams Engineering Jour 4 (2003) 843-854.
- [14] T. Hayat, M. Qasim, "Influence of thermal radiation and Joule heating on MHD flow of a Maxwell fluid in the presence of thermophoresis". International Journal of Heat and Mass Transfer, Vol. 53 (2010), 4780–4788.
- [15] M.A.A. Mahmoud, "Waheed S. E, MHD flow and heat transfer of a micropolar fluid over a stretching surface with heat generation (absorption) and slip velocity". Journal of the Egyptian Mathematical Society, Vol. 12 (2012), 20–27.

- [16] R.C. Bataller, "Effects of heat source / sink, radiation and work done by deformation on flow and heat transfer of a viscoelastic fluid over a stretching sheet". *Computers and Mathematics with Applications*, Vol. 53 (2007), 305–316.
- [17] V. Ravikumar, M.C. Raju, G.S.S. Raju, "Combined effects of heat absorption and MHD on convective Rivlin-Ericksen flow past a semi-infinite vertical porous plate with variable temperature and suction". *Ain Shams Engineering Journal*, Vol. 5 (2014), 867-875.
- [18] Chien-Hsin Chen, "Combined heat and mass transfer in MHD free convection from a vertical surface with Ohmic heating and viscous dissipation". *International Journal of Engineering Science*, Vol. 42 (2004), 699–713.
- [19] P.V. Satya Narayana, C.S. Sravanthi, "Simultaneous effects of sores and ohmic heating on MHD free convective heat and mass transfer flow of micropolar fluid with porous medium". *Elixir Appl. Math*, Vol. 48 (2012), 9379-9386.
- [20] H. Kumar, "Mixed convective magnetohydrodynamic (MHD) flow of a micropolar fluid with ohmic heating radiation and viscous dissipation over a chemically reacting porous plate subjected to a constant heat flux and concentration gradient". *J. Serb. Chem. Soc.* Vol. 78 (2013), 1–17.
- [21] A. Tamayol, M. Bahrami, "Analytical determination of viscous permeability of fibrous porous media". *International Journal of Heat and Mass Transfer*, Vol. 52 (2009), 2407–2414.
- [22] R.C. Sharma, U. Gupta, "Thermal convection in micropolar fluids in porous medium". *International Journal of Engineering Science*, Vol. 33 (1995), 1887–1892.
- [23] A. Raptis, "Boundary layer flow of a micropolar fluid through a porous medium". *Journal of Porous Media*, Vol. 3 (2000), 95–97.
- [24] S. Nadeem, M. Hussain, M. Naz, "MHD stagnation flow of a micropolar fluid through a porous medium". *Meccanica*, Vol. 45 (2010), 869–880.
- [25] A.M. Rashad, "Perturbation analysis of radiative effect on free convection flows in porous medium in the presence of pressure work and viscous dissipation". *Communications in Nonlinear Science and Numerical Simulation*, Vol. 14 (2009), 140–153.
- [26] M. A. El-Aziz, "Mixed convection flow of a micropolar fluid from an unsteady stretching surface with viscous dissipation". *Journal of the Egyptian Mathematical Society*, Vol. 21 (2013), 385–394.
- [27] M.A. El-Hakim, "Viscous dissipation effects on MHD free convection flow over a non-isothermal surface in a micropolar fluid". *Int. Comm. Heat Mass Transfer*, Vol. 27 (2000), 581-590.
- [28] J. I. Oahimire, B. I. Olajuwon, "Effect of Hall current and thermal radiation on heat and mass transfer of a chemically reacting MHD flow of a micropolar fluid through a porous medium". *Journal of King Saud University – Engineering Sciences*, Vol. 26 (2014), 112–121.
- [29] M. Hussain, M. Ashraf, S. Nadeem, M. Khan, "Radiation effects on the thermal boundary layer flow of a micropolar fluid towards a permeable stretching sheet". *Journal of the Franklin Institute*, Vol. 350 (2013), 194–210.

# Thermodynamic Analysis of R152a and Dimethylether Refrigerant Mixtures in Refrigeration System

Ayyalusamy Baskaran<sup>a</sup> \* and Koshy Mathews<sup>b</sup>

<sup>a</sup> Department of Mechanical Engineering, P. A. College of Engineering and Technology, Pollachi 642002, India

<sup>b</sup> Department of Mechanical Engineering, Kalavani College of Technology, Coimbatore 641105, India

Received 17 Dec 2014

Accepted 6 Aug 2015

## Abstract

R-134a is currently used as the refrigerant in refrigerator replacing the ozone depleting refrigerant R-12. Although R-134a has no Ozone Depletion Potential (ODP), it has a relatively larger Global Warming Potential (GWP) of 1300. In an effort to reduce greenhouse gas emissions, R-152a (difluoroethane) (GWP 130) and Hydrocarbons (GWP 20) are being considered as a replacement for R-134a. HC blend has a zero ODP and a negligible GWP. The only drawback of HC blend is the temperature glide. The drawbacks of using R-152a and HC blend with respect to GWP and temperature glide can be overcome by the refrigerant DME. The present paper presents the results of a thermodynamic study of new eco-friendly refrigerant blends of R-152a and DME. It was carried out for a single-stage vapor compression refrigeration system. These new refrigerants are generally azeotropic. Some of these new mixtures have better thermodynamic properties than those of pure R-152a. RefProp software has been used to determine the thermodynamic properties of the refrigerant blends. In this analysis, experimental validation of the new refrigerant mixture (60% DME + 40% R-152a) is carried out in domestic refrigerator. The results are better than those of R-152a and R-134a.

© 2015 Jordan Journal of Mechanical and Industrial Engineering. All rights reserved

**Keywords:** R152a, DME, Azeotropic Blends, Vapor Compression Refrigeration System, Coefficient of Performance.

## 1. Introduction

For the past half century, chlorofluorocarbons (CFCs) have been extensively used in the field of refrigeration due to their favorable characteristics. In particular, CFC-12 has been predominantly used for small refrigeration units including domestic refrigerator/freezers. Since the advent of the Montreal Protocol, however, the refrigeration industry has been trying to find out the best substitutes for ozone depleting substances [1].

In 1997, the Kyoto protocol was agreed on by many nations calling for the reduction in the emissions of greenhouse gases including HFCs [2]. Since the GWP of HFC-134a is relatively high (GWP1300) and also expensive, the production and use of HFC-134a will be terminated in the near future.

B. O. Bolaji, M. A. Akintunde and T. O. Falade investigated experimentally the performance of three ozone friendly HFC refrigerants (R-32, R-134a and R-152a) in a vapor compression refrigerator and compared the results obtained. The results show that the COP of R-152a was 2.5% higher than those of R-134a and 14.7% higher than that of R-32 [3].

Dimethylether (RE-170, DME) makes a better refrigerant than R-290 / R-600a blends as it has no temperature glide and does not separate during leakage. It has been extensively adopted by the aerosol industry as the most cost effective replacement for R-134a in propellant applications [4].

Valentine Apostol *et al.* [5] conducted a comparative thermodynamic study considering a single-stage Vapor-Compression Refrigeration System (VCRS) using, as working fluids, DME, R-717, R-12, R-134A, R-22 (pure substances) and R-404A, R-407C (zeotropic mixtures), respectively. The result of their study was that DME could be used as a refrigerant and that DME could be a good substitute for R-12 and R-134a.

A. Baskaran *et al.* [7] analyzed the performance of a vapor compression refrigeration system with various refrigerants mixture of HFC-152a, HC-290, HC-600a and RE-170 and their results were compared with R-134a as a possible alternative replacement. The results showed that the refrigerant blend RE-170 / R-152a (80/20 by wt %) was found to be a replacement for R-134a and also the COP of this blend is 5.7% higher than that of R-134a.

Choedaeseong, Dangsoo Jung [8] presented an experimental study on the application of R-435A (mixture

\* Corresponding author. e-mail: boss120367@gmail.com.

of DME and R-152a) to replace HFC-134a in domestic water purifiers. Test results showed that the energy consumption and discharge temperature were 12.7% and 3.7°C lower than that of HFC-134a.

Jung, Dong-Soo *et al.* [9] examined, both numerically and experimentally, in an effort to replace HFC-134a used in the refrigeration system of domestic water purifiers. Test results showed that the system performance with R-435A was greatly influenced by the amount of the charge due to the small internal volume of the refrigeration system of the domestic water purifiers. With the optimum amount of charge of 21 to 22grams, about 50% of HFC-134a, the energy consumption of R-435A was 11.8% lower than that of HFC-134a. The compressor discharge temperature of R-435A is 8°C lower than that of HFC-134a at the optimum charge. Overall, R-435A, a new long-term environmentally safe refrigerant, is a good alternative for HFC-134a requiring a little change in the refrigeration system of the domestic water purifiers.

A. Baskaran and Koshy Mathews [10] conducted the thermal analysis of vapor compression refrigeration system with R-152a and its blends R-429A, R-430A, R-431A and R-435A. In their analysis, the effects of the main parameters of the performance was analyzed for various evaporating temperatures. The results showed that the refrigerant R435A consumed 1.098% less compressor power than that of R152a. The COP, refrigerating effect for R-435A was 1.229%, 32.198% higher than R-152a, respectively. The refrigerant mass flow decreased by 24.353% while using R-435A substitute to R-152a. Other results obtained from their analysis showed a positive indication of using R-435A as a refrigerant in vapor compression refrigeration system substitute to R-152a.

A. Baskaran *et al.* [13] analyzed the performance on a vapor compression refrigeration system with various eco-friendly refrigerants of HFC-152a, HFC-32, HC-290, HC-1270, HC-600a and RE170 and their results were compared with R-134a as a possible alternative replacement. The results showed that the refrigerants RE-170, R-152a and R-600a had a higher COP than R-134a and RE-170 was found to be a replacement for R-134a [13].

A. Baskaran *et al.* [14] studied the performance characteristics of domestic refrigerator over a wide range of evaporation temperatures (-30°C to 30°C) and condensation temperatures (30°C, 40°C, 50°C) for working fluids R134a and refrigerant mixtures RE-170/R-600a. Their study was carried out by comparing parameters such as pressure ratio, refrigerating effect, isentropic work, coefficient of performance, compressor power, volumetric cooling capacity discharge temperature and mass flow rate. Their results indicated a drop in replacement for R-134a with blend (RE-170/R-600a) with the mass fractions of 80%/20%.

The present study presents a method for reducing the refrigerant charge and for increasing the security by replacing R-152a with a blend of dimethylether (DME).

## 2. Dimethyl Ether as Refrigerant

The dimethylether (DME, C<sub>2</sub>H<sub>6</sub>O) possesses a range of desirable properties as a replacement for R-134a. These

include better heat transfer characteristics than R-134a, a pressure/temperature relationship very close to R-134a, compatibility with mineral oils, compatibility with residual R-134a contamination, low cost and ready availability. It is also very environment-friendly. The ODP of DME is zero, and the GWP is 3 due to its very short atmospheric lifetime, only 6 days [6]. It is suitable for being used with ferrous metals, copper and copper-based alloys, and aluminum. The pressure-temperature relationship at saturation is very close to R-134a, as shown in Table 1. The basic physical properties of RE-170 and HFC refrigerants are shown in Table 2.

**Table 1.** Saturation pressure/temperature relationships of R-134a and DME

Temperature (°C)	Pressure(kPa) R-134a	Pressure (kPa) RE-170
-40	51.209	50.316
-20	132.73	124.24
0	292.80	265.18
20	571.71	505.99
40	1016.6	884.68
60	1681.8	1443.8

**Table 2.** Basic physical properties of eco-friendly refrigerants

Physical properties	R-134a	R-152a	RE-170
Molar Mass kg/kmole	102.03	66.051	46.07
Triple Temperature °C	-103.3	-118.59	-141.5
Boiling Point °C	-26.07	-24.023	-24.84
Critical Temperature °C	101.06	113.26	126.95
Critical Pressure , MPa	4.06	4.52	5.37
Critical Density kg/m <sup>3</sup>	511.9	368	270.99
Assentric factor	0.327	0.2752	0.2007
Diapole at NBP	2.058	2.262	1.301
Miscibility with Oil	Nil	Good	Good

As a result of previously comparative studies, analyzing the advantages and disadvantages of using R-152a and DME in vapor compression refrigeration systems as well as their reciprocal compatibility, the idea, which is the ground of this thermodynamic study, emerges; i.e., to reduce the disadvantages of R-152a (relatively high density, low refrigerating capacity, high compressor discharge temperature, GWP) and those of DME (high saturation pressure, high mass specific mechanical work) through their reciprocal combination. Besides obtaining new competitive eco-refrigerants, this idea allows to extend the use of R-152a/DME blend from air conditioning (A/C) to refrigeration applications and reduction of R-152a mass charge. As a support for the new proposed eco-refrigerants, there is a mixture between R-152a and DME (20/80) % mass fraction which has been

numbered and listed as a refrigerant mixture R-435A by ASHRAE recently.

### 3. Thermo Dynamic Study

In the present thermodynamic study, eleven refrigerants, R-152a/DME blends are taken into consideration, for which the DME mass fraction increases from 0%, (the blend referred to as A0, i.e., pure R-152a) to 100% (the blend referred to as A10, i.e., pure DME), with a mass fraction step of 10%. Consequently, R-435A is noted with the indicative A8. Figure 1 shows the variation of the saturation temperature with respect to R-152a mass fraction for various pressures (sat  $P = 1, 5, 10, 20$  and  $30$  bar), both for the saturated liquid and dry saturated vapor. It also shows that the obtained blends are azeotropic. Figure 2 shows the significant increase of the latent heat of vaporization with the increase of DME mass fraction. Consequently, R-435A has approximately 30% higher latent heat of vaporization than pure R-152a.

In order to establish which of the suggested new refrigerants is most recommended and which is the most appropriate DME mass fraction, the present study compares the performances obtained when using all of these eleven refrigerants in a single-stage vapor compression refrigeration system working in the same conditions. The calculation of these performances was carried out by Vapor compression cycle design program [12] based on their thermodynamic properties given by RefProp software [11].

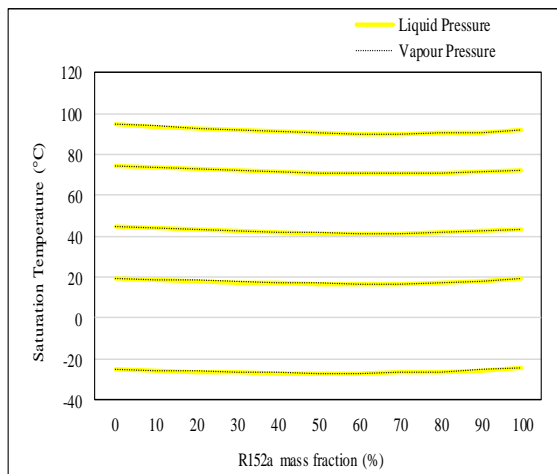


**Figure 1.** Saturation temperature depending on the pressure and R-152a mass fraction

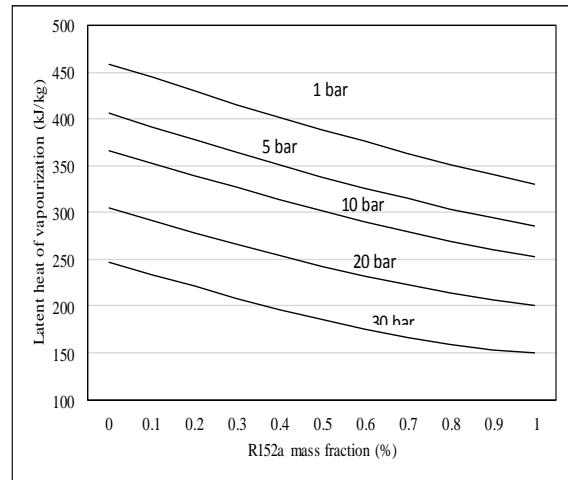


**Figure 2.** Latent heat of vaporization depending on the pressure and R-152a mass fraction

### 4. Calculation Methodology

In order to point out the optimum DME mass fraction and which of the eleven analyzed refrigerants is best suited for substituting R-152a, a comparative thermodynamic analysis was carried out, regarding the performances of a single-stage vapor compression refrigeration system. The schematic of sub critical cycle and thermodynamic cycle in  $p$ - $h$  diagram, for an azeotropic refrigerant blend between R-152a and DME (A6), are presented in Figures 3a and 3b. The thermal calculation of the thermodynamic refrigeration cycle asserting the same cooling load (1kW), for all types of the analyzed refrigerant blends, based on R-152a and DME, has been performed by applying the following study parameters:

- evaporation temperature ( $T_e$  [ $^{\circ}\text{C}$ ]);
- condensing temperature ( $T_c$  [ $^{\circ}\text{C}$ ]);
- super heating degree ( $T_{sh}$  [ $^{\circ}\text{C}$ ]);
- sub cooling degree ( $T_{sc}$  [ $^{\circ}\text{C}$ ]);

Using the previously shown calculation methodology for a cooling load of 1kW and for the following values of the study parameters  $T_c = +40^{\circ}\text{C}$ ,  $T_{sc} = 10^{\circ}\text{C}$ ,  $T_{sh} = 20^{\circ}\text{C}$ , calculations were made for different evaporation temperatures  $T_e = -30^{\circ}\text{C}$  to  $+10^{\circ}\text{C}$ , asserting a step of  $5^{\circ}\text{C}$ . The range chosen for the evaporation temperature refers to low temperature, refrigeration and A/C applications.

The performance parameters were determined by using calculation programs developed in CYCLE\_D 4.0 software, for each of the eleven considered refrigerants.

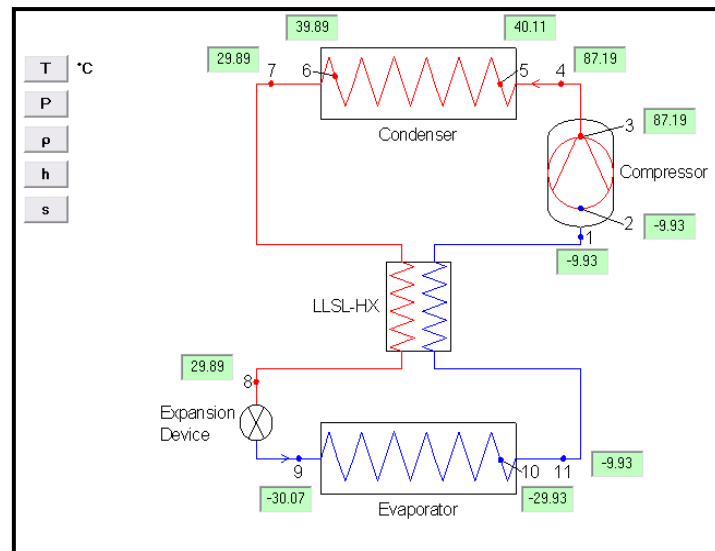


Figure 3. (a) Schematic of sub critical cycle for refrigerant blend A6

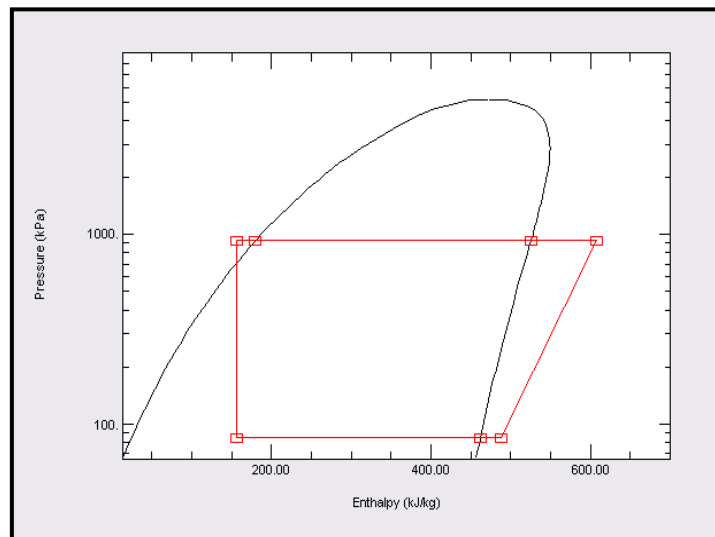


Figure 3. (b) Thermodynamic cycle in p - h diagram for azeotropic refrigerant blend A6

## 5. Materials and Methods

The test rig used for the experiment is a domestic refrigerator designed to work with R-134a. It consists of an evaporator, wire mesh air cooled condenser and hermetically sealed reciprocating compressor. Four pressure gauges were used and were respectively installed before and after each main component. All of these pressure gauges were fitted on a wooden panel to ensure that the gauge did not vibrate during testing. All of the ten points of the thermo couple wire were connected to the thermo couple scanner. Thermo couple scanner is a device to read the measured temperature. Among these points, 10 calibrated temperature sensors were installed at the evaporator inlet and outlet, compressor suction and discharge, compressor body, condenser outlet, dryer, freezer compartment and refrigerator cabin. In addition, the consumed voltage and current were recorded. The flow meter, which was connected to the pipe between condenser and filter dryer, was fixed to a wooden panel next to pressure gauges. The data were read through visualization and recorded every 15 minutes. Analyzing these data, the power consumption, working time, and ON time ratio of

the compressor were calculated. To check the quality of condensed liquid a sight glass was provided. As per the manufacturer's specification the quantity of the charge was 80gms of R-134a. Since additional pipes were used to fix the measuring devices the charge was optimized for the setup. The power consumption was found to be minimum for the charge quantity of 140gms.

A power meter was connected with a compressor to measure the power and energy consumption. Service ports were installed at the inlet of the expansion device and compressor for charging and recovering the refrigerant. The evacuation of moisture in the system was also carried out through the service port initially; the system was flushed with nitrogen gas to eliminate impurities, moisture and other materials inside the system, which may affect the performance of the system. The system was charged with the help of charging system and evacuated with the help of a vacuum pump. The refrigeration system was charged with 140gms of R-134a and the baseline performance was studied. After completing the baseline test with R-134a, the refrigerant was recovered from the system and the experimental procedures were repeated with R-152a and refrigerant mixture A6. Figure 4 shows a schematic

diagram of the measurement system used in the experimental setup. The most important specifications of the refrigerator are summarized in Table 3. Measured quantities with their range and uncertainties are listed in Table 4.



Figure 4. Schematic diagram of experimental setup

Table 3. Technical specifications of domestic refrigerator test unit

Cross Volume	180L
Storage Volume	169L
Current rating	1.1 max
Voltage	220-240V
Frequency	50Hz
No. of. Doors	1
Refrigerant type	R134a
Defrost System	Auto defrost
Refrigerant charged	0.140 kg
Capillary tube length	3.35m
Capillary tube inner diameter	0.00078m
Cooling capacity	182 W

Table 4. Measured quantities and their uncertainties

Quantity	Range	Uncertainty
Temperature	-40°C to 110°C	+1°C
Power consumption	0 to 1000W	0.001W
Voltage	0 to 240V	0.001V
Current	0 to 10A	0.001A
Pressure	0 to 300 PSI	+1PSI
Refrigerant flow meter	0 to 100 CC/Sec	0.1 CC/Sec

## 6. Experiments

As per the guide lines given by ASHRAE Hand book 2010, the energy consumption test and no load pull down test were conducted for the following conditions:

Freezer compartment : -18°C to -15°C  
 Food compartment : 3°C to 5°C  
 Steady ambient temperature : 25°C to 32°C

## 7. Results and Discussions

### 7.1. Thermodynamic Analysis

#### 7.1.1. Variation of the Refrigerating Effect

In Figure 5, the variation of the Refrigerating Effect (RE) is presented as depending on the evaporation temperature ( $T_e$ ) for each of the eleven types of refrigerants. For a certain type of blend (A0-A10), RE practically does not depend on  $T_e$ . In turn, RE increases with the increase of DME mass fraction. Thus, for R-435A refrigerant (A8 blend) RE increases by more than 30% in comparison with pure R-152a refrigerant (A0).

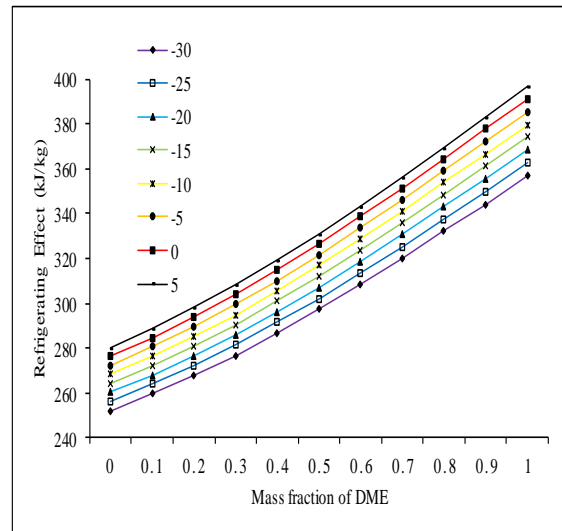


Figure 5. Variation of the Refrigerating effect depending on the evaporation temperature and the DME mass Fraction

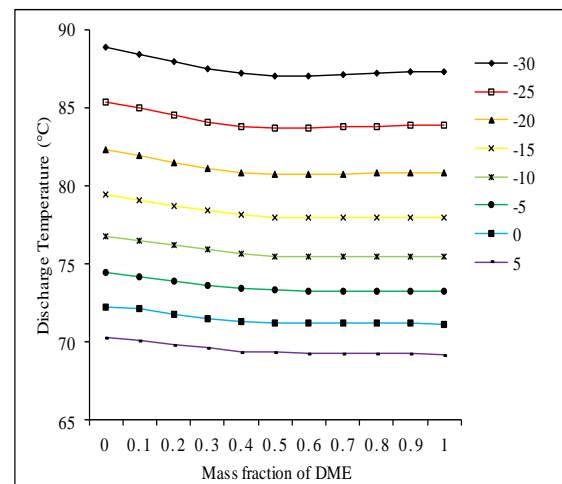


Figure 6. Variation of compressor discharge temperature depending on evaporating temperature and the DME mass Fraction

#### 7.1.2. Variation of Compressor Discharge Temperature

Figure 6 highlights the advantage of reducing the discharge temperature by increasing the DME mass fraction, in case of replacing R-152a with R-152a/DME blends. Thus, it results that the R-435A refrigerant may be also used in good conditions in refrigeration application area (-15°C <  $T_e$  < 0°C).

7.1.3. Variation of Saturation Pressure

Figure 7 shows that the saturation pressure increases with the increase of DME mass fraction, for the (0-55) % range. Therefore, at a certain constant evaporation temperature, the saturation pressure of R-152a/DME blends is higher than that of pure R-152a for the (20-80) % range.

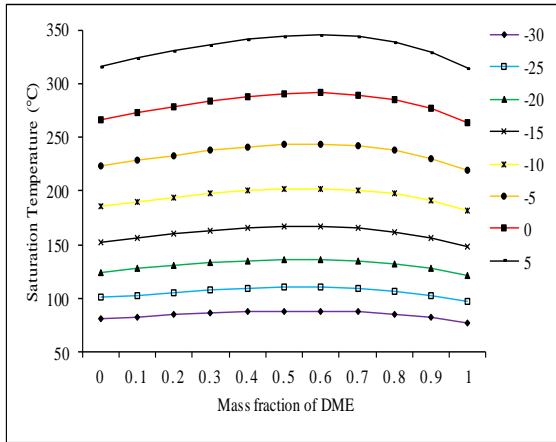


Figure 7. Variation of the saturation pressure depending on evaporating temperature and DME mass fraction

7.1.4. Variation of Coefficient of Performance

The COP variation, depending on the evaporation temperature and DME mass fraction, is shown in Figure 8. It results that for the same evaporation temperature, the COP of R-152a/DME blends is higher than that of pure R-152a. Thus, for R-435A refrigerant (A8 blend) COP increases by more than 30% in comparison with pure R-152a refrigerant (A0).

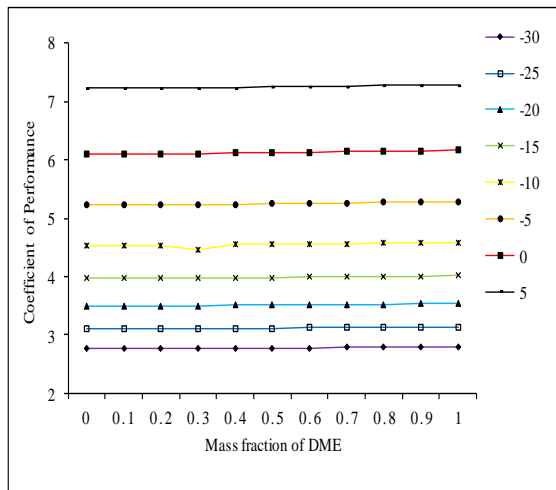


Figure 8. Variation of COP depending on evaporating temperature and DME mass fraction

7.1.5. Variation of Volumetric Refrigerating Capacity

Figure 9 displays the variation of the volumetric Refrigerating Capacity for R-152a/DME blend depending on the evaporation temperature and DME mass fraction. It results that for a certain evaporation temperature, within (0 - 40) % range the volumetric Refrigerating Capacity increases with the increase of DME mass fraction. This represents a very important advantage obtained when substituting R-152a with a blend having a DME mass fraction especially within (30-60) % range.

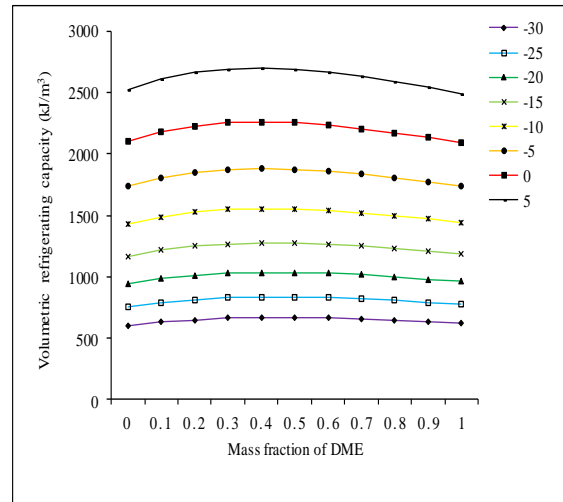


Figure 9. Variation of the volumetric Refrigerating Capacity depending on evaporating temperature and DME mass fraction

7.1.6. Variation of Refrigerant Volume Flow Rate

The variation of refrigerant volume flow rate at the compressor inlet depending on the evaporation temperature and DME mass fraction is shown in Figure 10. It results that with the increase of DME mass fraction within (10-90) % range, the refrigerant volume flow rate at the compressor inlet has lesser values than pure R-152a (A0). This represents another important advantage in the case of replacing R-152a, in an existing system, with the new proposed azeotropic blend containing (10-90)% DME mass fraction, which allows for the use of the same compressor.

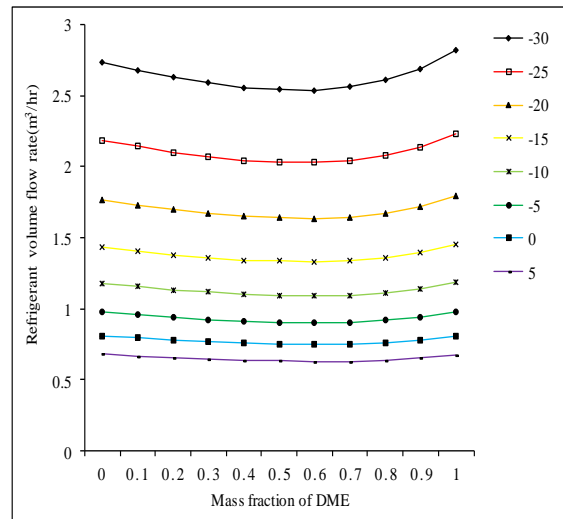


Figure 10. Variation of a refrigerant volume flow rate depending on evaporating temperature and DME mass fraction

7.1.7. Variation of Condenser Duty

The variation of condenser duty depending on the evaporation temperature and DME mass fraction is shown in Figure 11. It results that for a certain evaporation temperature, within the range the condenser duty increases with the increase of DME mass fraction.

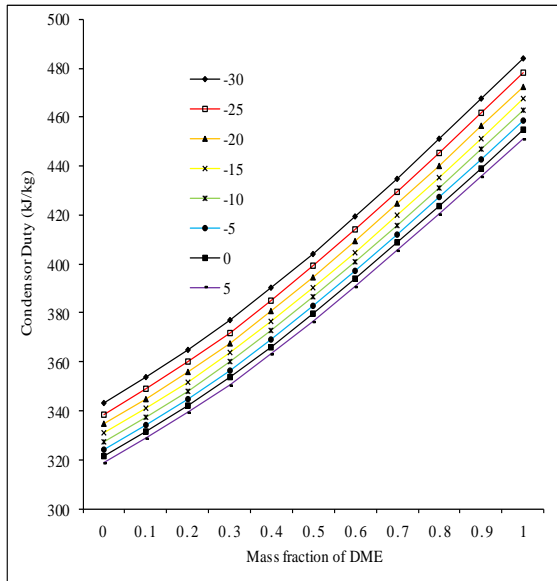


Figure 11. Variation of condenser duty depending on evaporation temperature and DME mass fraction

7.1.8. Variation of Compressor Power

The variation of compressor power depending on the evaporation temperature and DME mass fraction is shown in Figure 12. It highlights the advantage of reducing the compressor power by increasing the DME mass fraction, in the case of replacing R-152a with R-152a/DME blends.

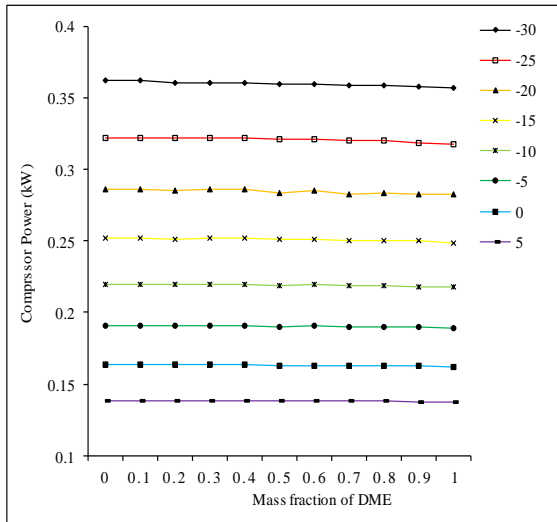


Figure 12. Variation of compressor power depending on evaporation temperature and DME mass fraction

7.2. Experimental Results

The average power consumption of the system is computed from the measurement system in the test rig. The coefficient of performance of the system for the refrigerants R-152a and new refrigerant mixture (A6) [DME 60% + R-152a 40%] are calculated and compared with base line refrigerant R-134a. The computational and experimental results are shown in Table 5.

Test conditions:

1. Evaporation Temperature ( $T_e$ ) =  $-16^{\circ}\text{C}$
2. Condensation Temperature ( $T_c$ ) =  $55^{\circ}\text{C}$

3. Degree of sub cooling ( $T_{sc}$ ) =  $10^{\circ}\text{C}$
4. Degree of super heating ( $T_{sh}$ ) =  $20^{\circ}\text{C}$

Table 5. Validation of results

Sl.No.	Refrigerants	Computational Results		Experimental Results	
		COP	CP*	COP	CP*
1	R-134a	2.728	0.075	1.466	0.117
2	R-152a	2.830	0.072	1.520	0.107
3	A6 (DME 60% + R-152a 40%)	2.847	0.072	1.537	0.117

\*Compressor Power (kW)

From the above results, it is observed that the COP of the system with new refrigerant mixture (A6) is 4.88% and 1.15% higher than that of R-134a and R-152a, respectively. The average compressor power consumption of the refrigerant mixture is similar with R-134a and 9.35% higher than that of R-152a.

8. Conclusions

Thermodynamic analysis was performed for R-152a and various refrigerant blends of DME and R-152a. Based on this analysis, the performance of the refrigerant mixtures (A4, A5, and A6) in the vapor compression refrigeration system is good.

After having compared the thermodynamic performances of the considered refrigeration system operating in the same imposed conditions the following advantages emerged:

- Being azeotropic blends, they do not cause any problems neither in maintaining their initial composition during the charging process, nor in case of gas leaks on the high pressure side;
- Higher volume heat load for the lesser volume flow rate at the compressor inlet;
- Higher coefficient of performance;
- Increased compressor life due to lower compressor discharge temperature; and
- Reduced mass flow rate and the compressor power for the operation.

An experimental analysis, carried out in a domestic refrigerator in which R-134a, R-152a and refrigerant mixture (A6), is used for performance investigation. The experimental results are compared with computational results.

Based on the results, the refrigerant mixture [A6] is recommended as an alternative refrigerant and leads to a reduction in the GWP (less than 50). By considering all kinds of performance parameters the proposed refrigerant mixture enhances the performance of the refrigerator.

Acknowledgement

The present study was supported through the Department of Mechanical Engineering, P. A. College of Engineering and Technology, Pollachi-2.

References

- [1] United Nation Environmental Programme, Montreal protocol on substances that deplete the ozone layer, Final Act, 1987.

- [2] Global Environment Change Report, A brief analysis of the Kyoto protocol, Vol. IX, No.24, December, 1997.
- [3] B. O. Bolaji , M. A. Akintunde, and T.O. Falade, "Comparative analysis of performance of three ozone-friends HFC refrigerants in a vapour Compression refrigerator", *Journal of Sustainable Energy & Environment*, Vol. 2, (2011) No.1, 61-64.
- [4] Nicholas Cox, "Developments and opportunities using hydrocarbons refrigerant blends", *Transforming Technologies Conference*, Institute of Mechanical Engineers, London, 2010.
- [5] Valentin Apostol, *et al.*, "Thermodynamic Study Regarding the Use of Dimethylether as Eco Refrigerant"; *Journal of Revista De Chime (Bucuresti)*, Vol. 60 (2009) No.7, 714-718.
- [6] Adamson, B.M., "Di methyl Ether as an R-12 Replacement", IIR - Commissions B & E - Oslo, Norway, 1998,
- [7] A. Baskaran, P. Koshy Mathews, "A Performance comparison of vapour compression refrigeration system using various alternative refrigerants", *International Journal of Scientific & Engineering Research*, Vol. 3 (2012) No.10, 1-6.
- [8] Choedaeseong (Daeseongchoe) the world wide (yo-hanlee) Air (Dangsoo Jung), "Performance of R435A on refrigeration system of domestic water purifiers", *International Journal SAREK*, Vol.11 (2010) No.1, 366-371.
- [9] Jung, Dong-Soo, et.al, "Performance Evaluation of R435A on Refrigeration System of Water Purifiers", *Journal of the Korean Solar Energy Society*, Vol. 33 (2013) No.1, 15-23.
- [10] A. Baskaran, P. Koshy Mathews, "Thermal analysis of vapour compression refrigeration system with R152a and its blends R429A, R430A, R431A and R435A", *International Journal of Scientific & Engineering Research*, Vol. 3 (2012) No. 10, 1-8.
- [11] Lemmon .EW, Huber .ML, McLinden. MO, NIST Reference Fluid Thermodynamic and Transport Properties – REFPROP. Version 9.0. National Institute of Standards and Technology, Boulder, USA 2010.
- [12] Steven Brown. J, Piotr. A, Domanski, Eric W. Lemmon, CYCLE\_D: NIST vapour compression cycle design program version 4.0 Gaithersburg (MD): National institute of standards and technology, Boulder, USA.2009.
- [13] A. Baskaran, P. Koshy Mathews, "A Performance comparison of vapour compression refrigeration system using Eco friendly refrigerants of low global warming potential", *International Journal of Scientific and Research Publication*, Vol. 2 (2012) No. 9, 1-8.
- [14] A. Baskaran, P. Koshy Mathews, "Investigation of New Eco Friendly Refrigerant Mixture Alternative to R134a in Domestic Refrigerator", *Australian Journal of Basic and Applied Sciences*, Vol. 9 (2015) No. 5, 297-306.

# Effect of 4% wt. Cu Addition on the Mechanical Characteristics and Fatigue Life of Commercially Pure Aluminum

Nabeel Alshabatat and Safwan Al-qawabah\*

*Mechanical Engineering Department, Tafila Technical University, PO Box 179, Tafila 66110, Jordan*

*Received 30 Nov 2014*

*Accepted 24 Aug 2015*

## Abstract

Aluminum is widely used in many engineering applications due to its light weight. However, pure aluminum has some weakness in its mechanical properties due to its columnar microstructure with large grain size. The mechanical properties can be improved by different methods, such as cold working, heat treatment, and alloying. This study aims at enhancing the mechanical properties of commercially pure aluminum through the addition of 4% wt. copper. Tensile test, microstructure test, microhardness test, and fatigue test were performed to investigate the effect of the copper addition on the mechanical properties of pure aluminum. The results depicted that copper addition significantly refined the aluminum grain size, which resulted in improved strength and microhardness, i.e., the fatigue strength was enhanced by more than 110% at 107 cycle, and the microhardness was enhanced by 57.9%.

© 2015 Jordan Journal of Mechanical and Industrial Engineering. All rights reserved

**Keywords:** *Aluminum, Copper, Fatigue Strength, Microhardness, Microstructure.*

## 1. Introduction

Aluminum and its alloys are widely used in engineering applications, such as automotive and aerospace industries, because of their high strength to weight ratio, besides other desirable properties such as machinability, high thermal and electrical conductivities, high corrosion resistance, improved damping capacity and ease of use. Similar to other structures and machine components, aluminum components are usually subjected to both static and dynamic loads. One example of dynamic loads is cyclic loads which cause fatigue failures. Fatigue properties of metals and alloys have been the subject of engineering efforts for more than 150 years because fatigue is the major cause of failure in metals, i.e., fatigue is estimated to cause approximately 80% of all material failures. Thus, the economic costs of fracture due to fatigue and its prevention are quite large. For example, the annual cost of the fatigue of materials to the U.S. economy is about 3% of the gross national product [1]. It is well-known that pure aluminum is too soft for most structural applications; therefore, the enhancement of its mechanical properties is an important requirement for engineers and metallurgists. The strengthening mechanisms of aluminum and its alloys can be introduced by strain hardening, solid solution, precipitation hardening and grain size reduction. In general, all strengthening techniques are based on the

principal of restricting dislocation motion [2]. The grain refinement mechanism will be adopted in the present study for aluminum strengthening. Aluminum grain refinement can be mainly achieved by heat treatment and alloying Aluminum with other elements such as copper, titanium, boron, magnesium, etc. [3]. On the other hand, some alloying processes and heat treatments would have a great influence in making discontinuities and weak links within the material, which act as nucleation sites for pit and crack origins [4, 5]. Grain refinement does not only strengthen aluminum and aluminum alloys under static loads, but also under cyclic loads. It is recognized that materials with fine grains have a greater resistance to fatigue-crack initiation [6-8]. In addition to grain refinement mechanism, the fatigue resistance is improved by surface treatment. The surface treatment includes creating residual compressive stresses by different methods such as shot peening [9-11] and roller burnishing [12, 13]. Alloying aluminum with copper affects the strength and hardness of both heat treated and unheat treated aluminum casting alloys at both ambient and elevated service temperature [14]. It also improves the machinability of alloys by increasing the matrix hardness. The addition of copper to Al-Si alloys can form CuAl<sub>2</sub> phases and other intermetallic compounds which increase the strength of the casting parts [15-17]. Copper also increases the heat treatability of the alloy. The addition of copper significantly decreases the melting point and the eutectic temperature of the alloy. Therefore,

\* Corresponding author. e-mail: safwan1q@gmail.com.

the copper increases the solidification range of the alloy [18, 19]. A previous work, by Al-Rawajfih and Al-Qawabah, studied different percentages of copper additions, namely 3, 6, and 9% Cu. They reported that the copper precipitated inside the grain as the copper percentage increased from 3 to 6, as shown in Figure 1 [20]. Therefore, it is worth to investigate the 4% Cu addition on the mechanical properties and fatigue life of pure aluminum, which is the main objective of the present study.

## 2. Materials, equipment and experimental procedures

### 2.1. Materials

Different materials have been used in the present work, namely commercially pure Al (99.8%), high purity Cu, pure graphite crucible and pure graphite rods. Copper is used as an alloying element in the present work. It was available as a powder of 99.8% purity, with a melting point of 1083°C, and density of 8.2 g/cm<sup>3</sup> at 20°C [8]. The chemical compositions, in weight percent, of aluminum are shown in Table 1.

### 2.2. Equipment

The following machines and equipment were used throughout the experimental work:

1. An electric resistance furnace (Type Carbolite) with 0-1100°C.
2. Digital microhardness tester (Model HWDM-3).
3. Universal Testing Machine (Qusar) with 100 KN capacities.
4. CNC lathe machine (CNC-1000L COLCHESTER).
5. Rotating Fatigue machine (HSM .19 mk.2).

### 2.3. Experimental Procedure

#### 2.3.1. Preparation of Al-4%Cu alloy

The Al-4%Cu was prepared by melting the pre-calculated amount of high purity aluminum rods at 750°C,

then the pre-calculated amounts of pure Cu was added to the melt in a graphite crucible. The melt was stirred for 2 minutes then poured to solidify in a brass mold and to cool in air. The Al-4%Cu alloy was synthesized in the form of 14 mm diameter and 70 mm length cylindrical rods from which test samples were machined.

#### 2.3.2. Metallurgical Examination

In this test, the general microstructures of pure Al and Al-4%Cu in the as cast condition were determined after grinding, polishing and etching in order to get clear microstructures. The etchant made of 1.5% HCl acid, 2.5% HNO<sub>3</sub>, 0.5% HF acid and 95.5% H<sub>2</sub>O by weight. Photomicrographs were obtained using the NIKON 108 type microscope at magnification of 200x.

#### 2.3.3. Microhardness Tests

Microhardness measurements were taken on the surface of the polished Al and Al-4%Cu specimens at magnification 200x using HWDM-3 at 300 gm load. The measurements were taken for three specimens of each material and five times for each specimen. Then, the average microhardness was calculated.

#### 2.3.4. Compression Tests

The compression test was performed to insure the homogeneity of the casted alloy when it was compared to tensile test results. Cylindrical specimens of 10 mm diameter and 10 mm length were machined using CNC lathe machine at the same cutting conditions (depth of cut, spindle speed, and feed rate). The compression test was carried out at room temperature using (Quasar 100 Universal Testing Machine of 100 KN capacity) at 10<sup>-3</sup> s<sup>-1</sup> strain rate. The load-deflection curve was obtained for each specimen of Al and Al-4%Cu alloy, from which the true stress-true strain curve was determined. The compression test was repeated three times for each condition, and then the average load-deflection curve was obtained.

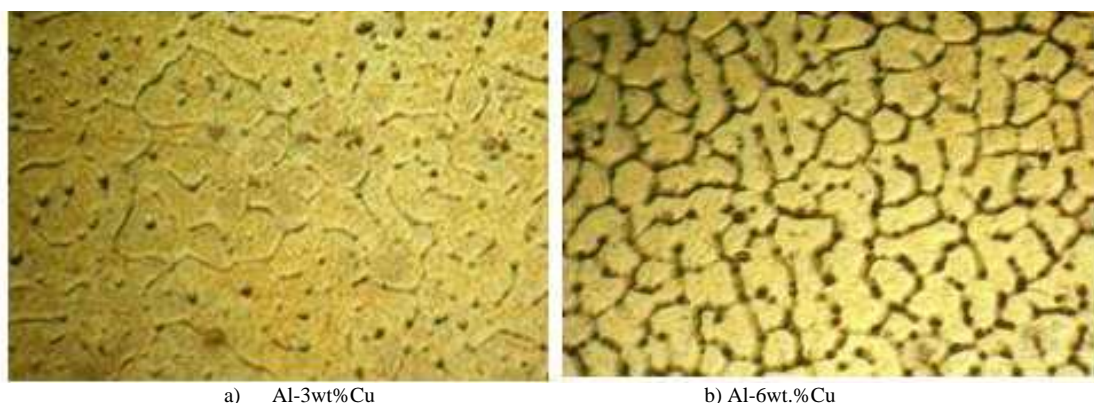


Figure 1. Photomicrograph of Al-3wt.%Cu and Al-6wt.% Cu, [20]

Table 1. Chemical composition of commercially pure aluminum

Element	Fe	Si	Cu	Mg	Ti	V	Zn	Mn	Na	Al
Weight %	0.09	0.05	0.005	0.004	0.004	0.008	0.005	0.001	0.005	Rem.

### 2.3.5. Tensile Tests

The tensile test is probably the most important fundamental test which can be performed on material. Tensile tests are simple, relatively inexpensive, and fully standardized. The tests were carried out on work pieces at strain rate of  $10^{-3} \text{ s}^{-1}$  using Instron machine type Quasar of 100 kN capacities, the load – deflection curves were obtained from which the true stress – strain diagrams were obtained. The dimension of tensile specimen is shown in Figure 2. The tensile test was repeated three times for each material, and then the average of load-deflection has been calculated.

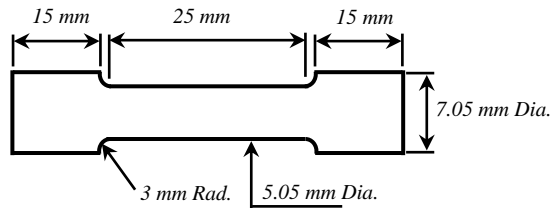


Figure 2. Tensile test specimen (ASTM-E8, 1975).

### 2.3.6. Fatigue Test

Rotating bending fatigue tests were performed according to ISO1143: 2010 [21]. The specimen has a circular cross section and is subjected to dead-weight loading at the free end while swivel bearings permit rotation. Points in the test-section surface, during each rotation, are subjected to sinusoidal stress variation from tension on the top to compression on the bottom. Standard fatigue specimens of the dimensions shown in Figure 3 were machined from the casted Al and Al-4%Cu ingots using a Colchester CNC-1000L lathe. Then, the specimens were mechanically polished using the same fine grades emery papers to achieve almost the same surface quality to avoid the effect of the surface conditions on fatigue results. Fatigue tests were conducted on the rotary bending fatigue machine (HSM. 19 mk. 2 apparatus) at different stress levels, where the number of cycles to fail at each stress level, was determined. The specimens rotated at 5700 rpm in a laboratory air at ambient temperature and the load ratio (i.e.,  $\sigma_{min} / \sigma_{max}$ ) was -1. The tests were conducted for three specimens at each stress level, and then the average life of these specimens was reported.

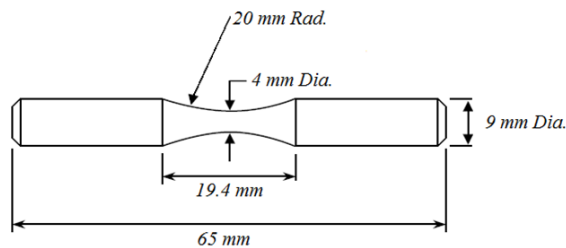


Figure 3. Standard fatigue specimen

## 3. Results and Discussions

### 3.1. Effect of Copper Addition on the Microstructure of Pure Aluminum

The microstructure of Al-4%Cu alloy at 200x

magnification is shown in the Figure 4. It can be seen that the grain refinement, due to copper addition, was achieved.

The grain size decreased significantly from 124  $\mu\text{m}$  for commercially pure aluminum to 30.7  $\mu\text{m}$  for Al-4%Cu alloy. This reduction is attributed to the intermetallic compound that resulted after the copper addition. Moreover, the grain shape was changed from columnar to equiaxial.

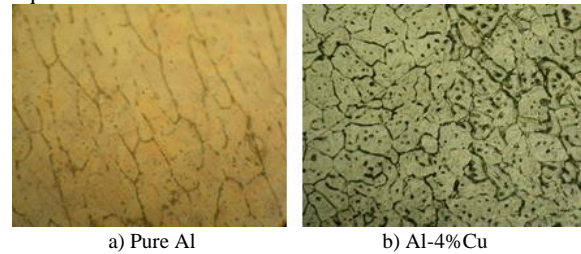


Figure 4. Photomicroscan of (a) pure Al, and (b) Al-4%Cu at 200x magnification

### 3.2. Effect of Copper Addition on the Mechanical Characteristics of Pure Aluminum

Figure 5 shows the effect of 4% wt. copper addition to Al on its mechanical behavior, which is represented by true stress-true strain curve. The figure shows a very pronounced improvement in its mechanical behavior; for example, an increase of 95% in its flow stress at 20% strain. Regarding the engineering hardening index,  $n$ , it was 0.31 for Al and increased to 0.39 for Al-4%Cu, and the strength coefficient,  $k$ , was 112.17 MPa for Al and increased to 249.64 MPa after 4% wt. Cu addition. This enhancement can be attributed to the formulation of  $\text{Al}_2\text{Cu}$  intermetallic compound that restricts the grain growth during solidification, which resulted in this refinement; however, this result is consistent with the Hall pitch equation:

$$\sigma_Y = \sigma_0 + k/d^{1/2} \quad (1)$$

where  $\sigma_Y$  is the yield stress,  $\sigma_0$  and  $k$  are constants for a particular material and  $d$  is the average grain diameter of material.

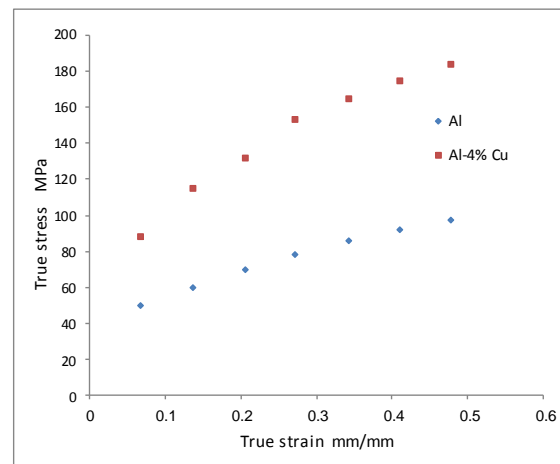
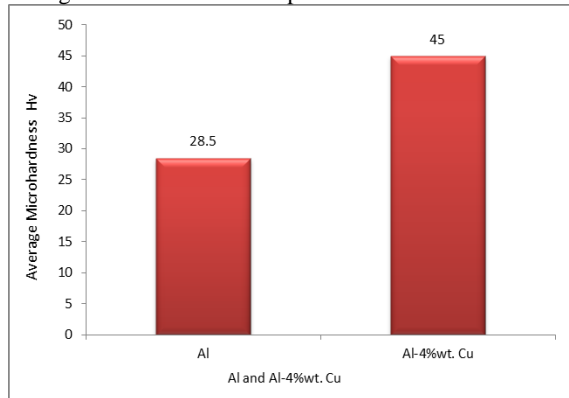


Figure 5. True stress-True strain of Al and Al-4% Cu alloy

### 3.3. Effect of Copper Addition on the Microhardness of Pure Aluminum Alloy by 4% Copper

It can be seen from the histogram of Figure 6 that the hardness was enhanced by 57.89% after 4% copper addition; this can be explained by the reduction of the grain size and due to intermetallic compounds formation throughout the solidification process.



**Figure 6.** Average microhardness of pure aluminum and Al-4%wt. Cu alloy

### 3.4. Effect of Copper Addition on the Fatigue Life of Pure Aluminum Alloy by 4% Copper

Figure 7 represents the S-N diagram for Al and Al-4%Cu alloy. As shown, the addition of copper by 4% wt. significantly increases the fatigue strength (i.e., the alloying increases the fatigue strength by more than 100% that attained at  $10^7$  cycles). This is attributed to the effect of grain refinement resulting after the copper addition caused by intermetallic compound formed during the solidification process. The small grain size enhances fatigue strength by slowing down the crack initiation, i.e., the fine grains act as obstacles for dislocation movement which reduces the possibility of micro cracks formation. Moreover, grain refinement tends to reduce both the amount of porosity and the size of the pores in casting alloys [3]. It is well-known that the defects, like porosities in casted aluminum, have a significant effect in shortening the fatigue life by reducing the crack initiation and propagation periods [22]. Thus, reducing the amount of porosity plays a significant role in increasing the fatigue life.

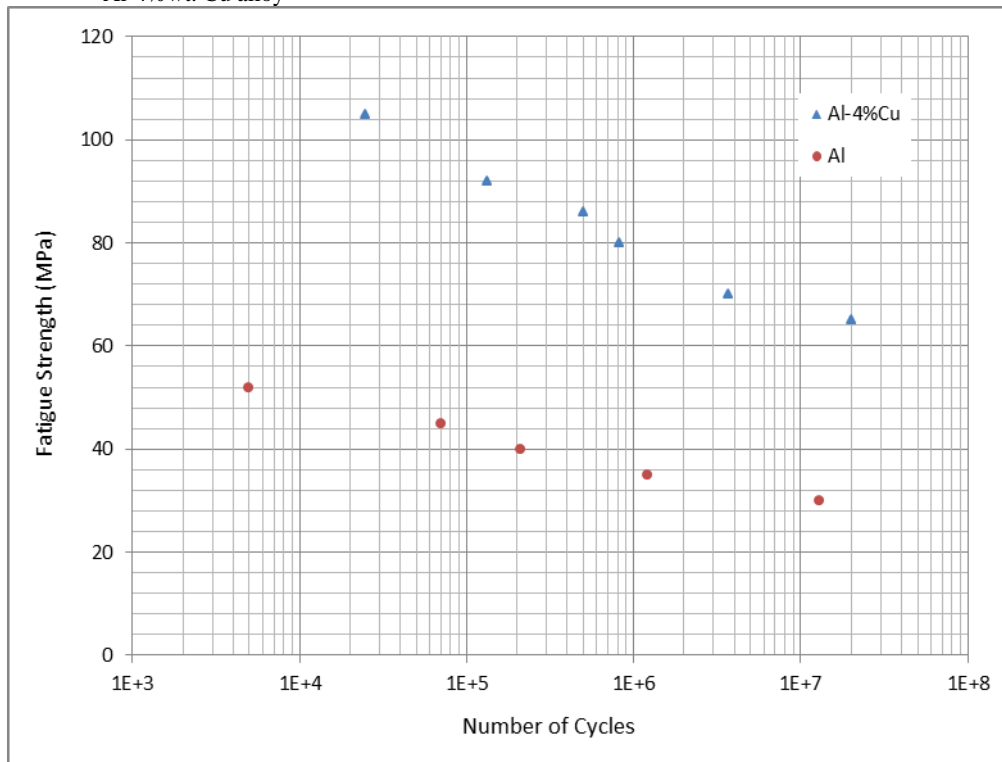


**Figure 7.** S-N diagram for Al and Al-4%Cu samples

## 4. Conclusions

The effect of alloying the aluminum by copper on some mechanical properties was investigated. In particular, copper was added at a rate of 4%wt to commercially pure aluminum. It is found that the alloying of aluminum with 4%wt of copper decreased the grain size (i.e., the copper worked as a grain refiner). Also, the alloying transforms the columnar structure to an equi-axial one.

The experiment showed that the addition of copper resulted in the enhancement of the alloy microhardness by

57.9%, and enhanced the mechanical behavior by 95% increase in its flow stress at 20% strain. Furthermore, the addition of copper by 4%wt increased the fatigue life significantly at all values of stress and shifted the S-N curve up (i.e., the alloying increases the fatigue life by 112% at 10 million cycles).

## References

- [1] Dowling N. Mechanical behavior of materials. 4<sup>th</sup> ed., New Jersey: Prentice Hall; 2012.

- [2] Rollasaon R. Metallurgy for engineers, 4<sup>th</sup> ed., Great Britain: Edward Arnold; 1973.
- [3] G.K. Sigworth, T.A. Kuhn, "Grain Refinement of Aluminum Casting Alloys". AFS Transactions, Vol. 115(2007), 1-12.
- [4] F.M. Khoshnaw, A. I. Kheder, F.S.M. Ali, (2005), "Corrosion fatigue behavior of nitrated low alloy steel compared to austenitic stainless steel", Stainless Steel World Conference, Holland; 2005.
- [5] A. Merati, "A study of nucleation and fatigue behavior of an aerospace aluminium alloy 2024-T3", International Journal of Fatigue, Vol. 27(2005) No. 1, 33-44.
- [6] T. Hanlon, Y.-N. Kwon, S. Suresh, "Grain size effects on the fatigue response of nanocrystalline metals". Scripta Materialia, Vol. 49 (2003) No. 7, 675–680.
- [7] T. Hanlon, E.D. Tabachnikova, S. Suresh, "Fatigue behavior of nanocrystalline metals and alloys". International Journal of Fatigue, Vol. 27 (2005) No. 10-12, 1147–1158.
- [8] H. Mughrabi, H.W. Hoppel, M. Kautz, "Fatigue and microstructure of ultrafine-grained metals produced by severe plastic deformation". Scripta Materialia, Vol. 51 (2004) No. 8, 807–812.
- [9] U. Martin, I. Altenberger, B. Scholtes, K. Kremmer, H. Oettel, "Cyclic deformation and near surface microstructures of normalized shot peened steel AZE 1045". Materials Science and Engineering A, Vol. 246 (2004) No. 1-2, 69–80.
- [10] L. Wagner, "Mechanical surface treatments on titanium, aluminum and magnesium alloys". Materials Science and Engineering A, Vol. 263 (1999) No. 2, 210–216.
- [11] I. Altenberger, B. Scholtes, U. Martin, H. Oettel, "Cyclic deformation and near surface microstructures of shot peened or deep rolled austenitic stainless steel AISI 304". Materials Science and Engineering A, Vol. 264 (1999) No. 1-2, 1–16.
- [12] C. Gardin, S. Courtin, D. Bertheau, G. Bezine, H. Ben, H. Hamouda, "The influence of roller burnishing on the fatigue crack propagation in notched round bars- Experimental observations under three-point bending". Fatigue & Fracture of Engineering Materials and Structures, Vol. 30 (2007) No. 4, 342–350.
- [13] P. Zhang, J. Lindemann, "Influence of shot peening on high cycle fatigue properties of the high-strength wrought magnesium alloy AZ80". Scripta Materialia, Vol. 52 (2005) No. 6, 1011–1015.
- [14] R.S. Rana, P. Rajesh, S. Das, "Reviews on the influences of alloying elements on the microstructure and mechanical properties of aluminum alloys and aluminum alloy composites". International Journal of Scientific and Research Publications, Vol. 2 (2012) No. 6, 1-7.
- [15] J. Gauthier, P.R. Louchez, F.H. Samuel, "Heat treatment of 319.2 aluminum automotive alloy: part 1, Solution heat treatment". Cast Metals, Vol. 8 (1994) No. 2, 91–106.
- [16] M.H. Mulazimoglu, N. Tenekedjiev, B.M. Closset, J.E. Gruzleski, "Studies on the minor reactions and phases in strontium-treated aluminum–silicon casting alloys". Cast Metals, Vol. 6 (1993) No. 1, 16-28.
- [17] F.H. Samuel, A.M. Samuel, H.W. Doty, "Factors controlling the type and morphology of Cu-containing phases in 319 Al alloy, AFS Transactions, Vol. 104 (1996), 893–901.
- [18] P.N. Anyalebechi, "Analysis of the effects of alloying elements on hydrogen solubility in liquid aluminum alloys". Scripta Materialia, Vol. 33 (1995) No. 8, 1209–1216.
- [19] C.H. Cacers, M.B. Djurdjevic, T.J. Stockwell, J.H. Sokolowski, "The effect of Cu content on the level of microporosity in Al–Si–Cu–Mg casting alloys". Scripta Materialia, Vol. 40 (1999) No.5, 631–637.
- [20] A.E. Al-rawajfeh, S.M. Al-Qawabah, " Investigation of copper addition on the mechanical properties and corrosion resistance of commercially pure Aluminum" Emirates Journal for Engineering Research, Vol. 14 (2009) No. 1, 47-52.
- [21] ISO 1143:2010 Metals-Rotating bar bending fatigue testing.
- [22] Q. G. Wang, D. Apelian, D. A. Lados, "Fatigue Behavior of A356/357 Aluminum Cast Alloys: Effect of Microstructural Constituents - Part II", Journal of Light Metals, Vol. 1 (2001) No. 1, 85-97.



# Implementation of Systems Engineering Lifecycle-Tools-Model Framework on Large Industrial Scale

Islam Helaly Afefy<sup>a\*</sup>, Ahmed Mohamed El-kamash<sup>b</sup> and Nihal Mahmoud El-Sayar<sup>c</sup>

<sup>a</sup> Assistant professor, Industrial Engineering Dept., Faculty of Engineering, Fayoum University, Fayoum, Egypt.

<sup>b</sup> Professor, Hot Laboratory, Atomic Energy Authority of Egypt.

<sup>c</sup> P.G. Student, Industrial Engineering Dept., Faculty of Engineering, Fayoum University, Fayoum, Egypt.

Received 21 Dec 2014

Accepted 29 Jun 2015

## Abstract

Systems Engineering Lifecycle-Tools-Model Framework (SELTMF), based on integrating ISO/IEC 15288 with seven point of view architecture framework, is presented. The developed framework considers the service oriented point of view in addition to the common points of view suggested in the British Ministry of Defense architecture framework. Studied Key Performance Indicators (KPIs) included financial, internal business, quality, innovation learning and integrated measures. The proposed framework is implemented on the Egyptian Company for Development Industries. The results helped in identifying the problems that face the company at different levels, including production and administration. After the implementation, it was found that the total production time decreased by 52.1% and the total productivity increased by 28.1%.

© 2015 Jordan Journal of Mechanical and Industrial Engineering. All rights reserved

**Keywords:** SELTMF, Lifecycle Analysis, KPIs, Productivity.

## 1. Introduction

The application of Systems Engineering (SE) tools is considered an important task to reduce risks associated with the establishment of new systems and/or modifying complex systems. These tools are dependent on system lifecycle simulation and the evaluation of system performance. The identification and inclusion of performance indicators measures is a critical step to ensure that the system evaluation process is reliable. Overall Equipment Effectiveness is one of the performance evaluation methods that are most common and popular in the production industries [1]. Beilei *et al.* [2] discussed an evaluation methodology by considering a documentation matrix which included process flow diagram and value tool documentation to analyze the necessity and redundancy of the process. Ghader *et al.* [3] identified Key Performance Indicator measure (KPI) of the equipment and the production machinery in Idem Company, Tabriz, Iran. František [4] discussed financial KPIs in engineering companies. Overall equipment effectiveness is a kind of measurement tool used in total productive, repair and maintenance and shows how effectively the machinery functions [5, 6].

This work is a continuation of our previous work in which the implementation of total productive maintenance

and overall equipment effectiveness evaluation were introduced and the presentation of tools-model framework application in industry was tested [7, 8]. These efforts proved that the framework could be used to improve both the productivity and the economy of the production process. In the present work, the framework is applied to a large-scale industry to identify the problems that face the establishment; then these problems are addressed by proposing changes in the routine work and finally the proposed changes are implemented on the process.

## 2. Systems Engineering Applications in Varied Fields

The Systems Engineering (SE) is applied to varied fields, such as education, lawmaking, energy, human integrations, etc., as it could be presented in industry or service. Applying SE in education describes or discusses (1) issues which need to be addressed for the creation of curricula and professional degree programs in Service Systems Engineering (SSE) at the graduate level; and (2) the development of an autonomous litter collecting robot as a vehicle for combining several systems design and engineering tools in a real multidisciplinary student project. Clyde and Yacov [9] investigated the needs, requirements, and challenges associated with the academic and professional certification of systems engineers, given the breadth and depth required of them, and especially the

\* Corresponding author. e-mail: islamhelaly@yahoo.com.

specific domain knowledge and expertise required supplementing their competence in SE. David [10] applied the methods of SE to the design of the laws of the government. The SE approach brings the knowledge and expertise of investigative science and engineering to bear upon the design, operation, follow up evaluation, and optimization of laws that effectively solve societal problems. The standards have been evolving from the United States (US) Military to international and commercial, with recent standards taking a broader scope. Two capability maturity models have been merged into a third, which is tied to the standards [11, 12].

SE can be applied on all projects: small, large, simple, or complex. The degree of formality and rigor applied to the SE process varies depending on the complexity of the project. This is called tailoring. All projects need to be assessed for the amount of formal SE processes needed. Projects can be tailored up, more formality, for more complex projects as well as tailored down for simpler projects. The SE discipline emerged as an effective way to manage complexity and change. Both complexity and change escalated in our products, services, and society. Reducing the risk associated with new systems or modifications to complex systems continues to be a primary goal of the systems engineer [13, 14].

### 3. Proposed KPIs

The Proposed KPIs are presented in Figure 1. Evaluation business trends are categorized into five classes: financial, internal business, quality, innovation learning and integrated measures. Proposed KPIs are used to assess the system and compare between the situation before and after applying the systems engineering tools framework (SETF). These measures are applied to the application firm during two periods one before applying the SELTMF and the other one is after the application of this proposed model as an assessment method. Each period is three months, i.e., a quarter of the year (Qtr.), the first Qtr. presents the firm state before applying the proposed

SELTMF model and the second Qtr. presents the firm state after applying it.

### 4. The Proposed SELTMF Model Verification

The proposed model SELTMF presents a framework integrating the main three activities of SE, which contribute to system development in several ways. Simulation of the high level operating concept models can contribute to a deeper understanding of the big picture and the requirements; this puts on the System Of Interest (SOI). Executable models can also serve as a communication tool for different stakeholders to express their needs. An executable model depicting the big picture can also be used to try out alternative concepts; a prototype can, for example, be tested in this virtual operational environment to evaluate to what extent the suggested solutions can fulfill the stakeholders needs. Table 1 illustrates a simple comparison between this proposed model framework to one of the previous model frameworks: Tommy's model framework [15, 16, 17, 18]. Tommy, in his framework, depended on integrating the ISO/IEC 15288 system lifecycle processes and stages as illustrated in Figure 4. He used the architectural framework represented in British Ministry of Defense Architecture Framework (MODAF) with six viewpoints as illustrated in Figure 2, as an architectural tool, for the description of all solutions during a systems lifecycle, and M&S that made Systems Engineering more efficient, as in Figure 4. However, the proposed model of the present research depends on integrating ISO/IEC 15288 system lifecycle processes, stages and SETF, as in Figure 6, to serve at each stage and process for any system lifecycle. Also, developed the MODAF tool to the latest version with seven viewpoints as shown in Figure 3, and recommended the proper tools category for any process or stage during the system lifecycle. The two references made their specific proposed model. Tommy made his model where its pivot is modeling and simulation (M & S), as shown in Figure 6, where the proposed SELTMF model, of the present research, is based on SETF, as shown in Figure 7.

**Table 1.** Mapping the proposed SELTMF model to another model framework

Comparison Point	Tommy's model framework [19]	The proposed model framework SELTMF [1]
Used tools	Architecture framework (MODAF), and M & S	SE tools template (SETF)
The basic building block	MODAF and M & S	SETF
The standard	ISO/IEC 15288	ISO/IEC 15288
Adopted framework	Architectural framework; MODAF (only 6 viewpoints) See Figure 2	Developed MODAF (7 viewpoints) See Figure 3
System integration	Lifecycle processes and stages See Figure 4	See Figure 5
The main model	The interplay between SOI, ISO/IEC 15288, MODAF and M&S See Figure 6	See Figure 7

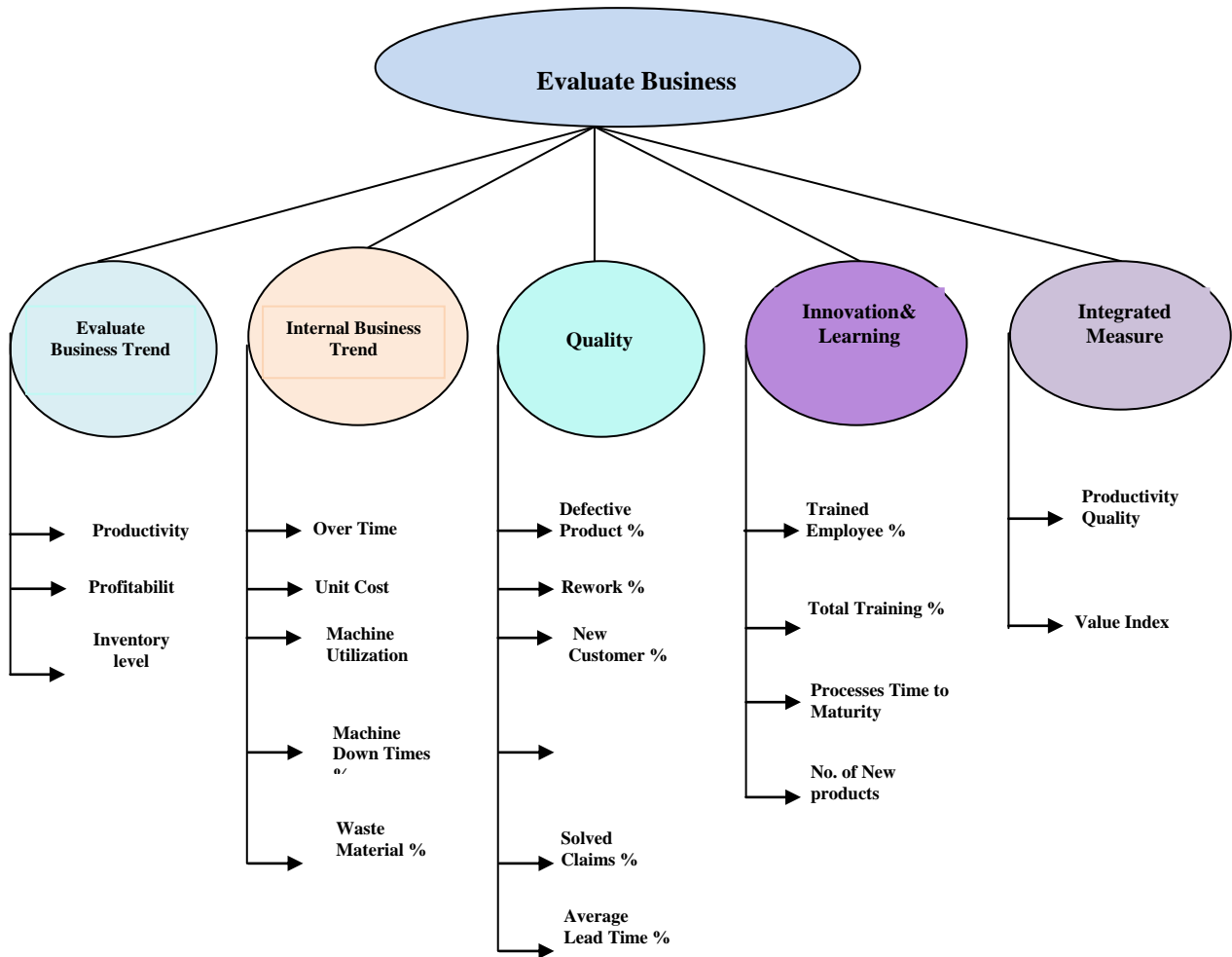


Figure 1. Proposed KPIs

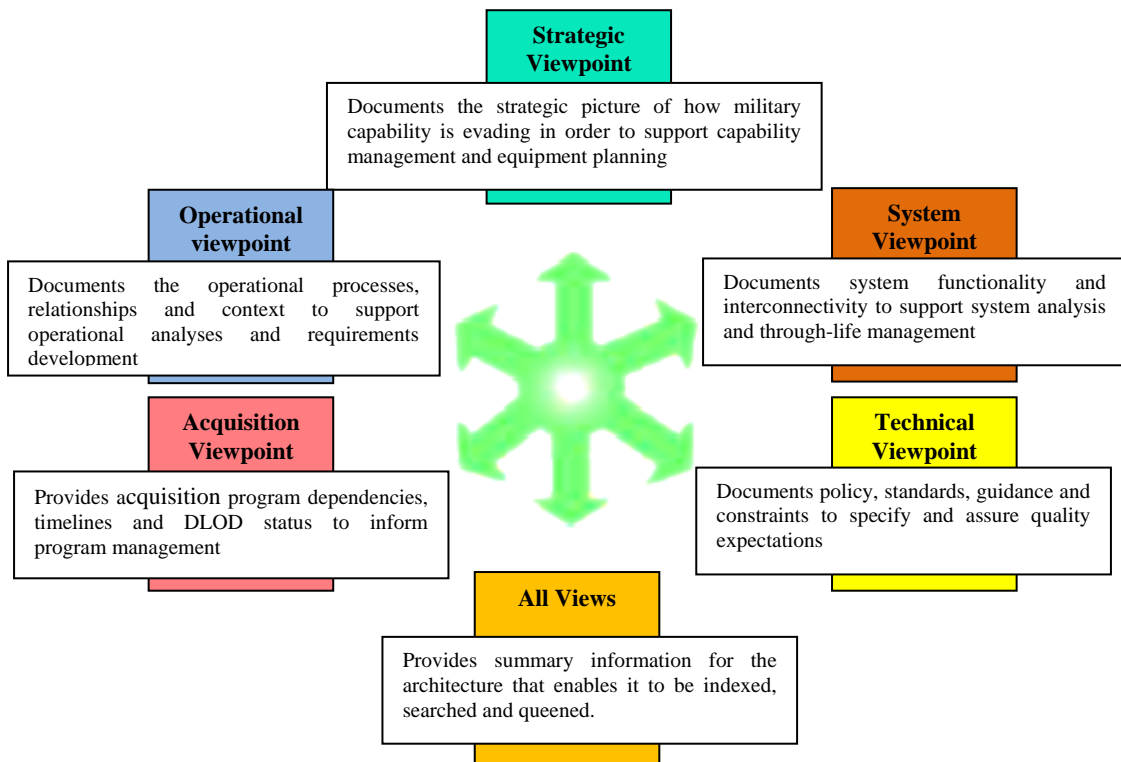


Figure 2. MODAF six viewpoints

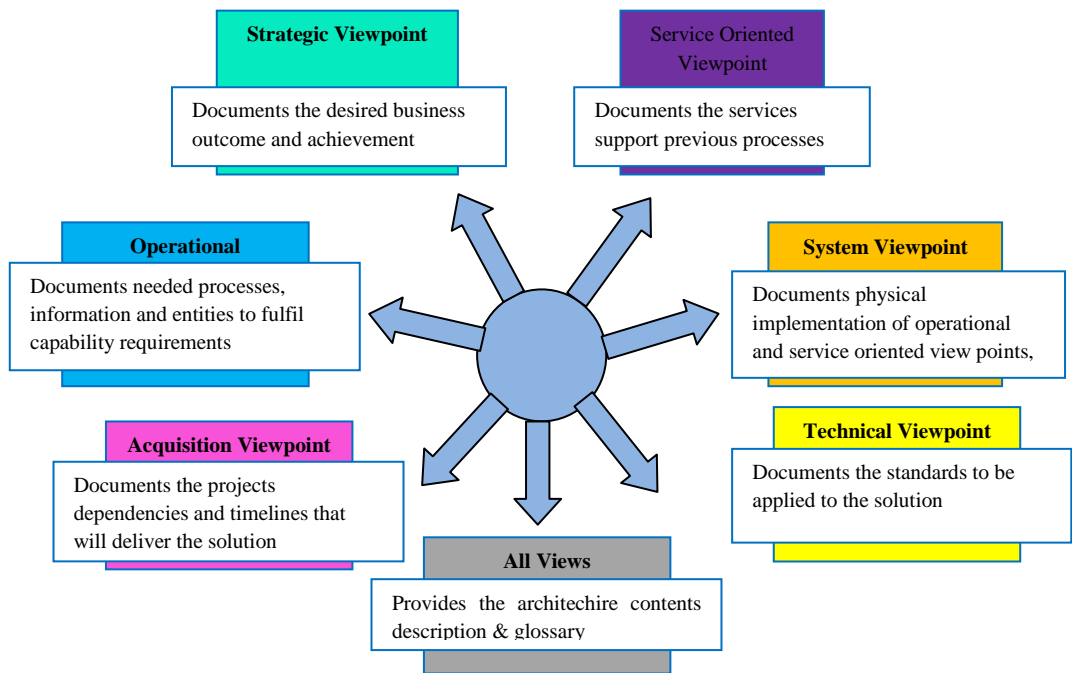


Figure 3. The modified MODAF seven viewpoints and SETF

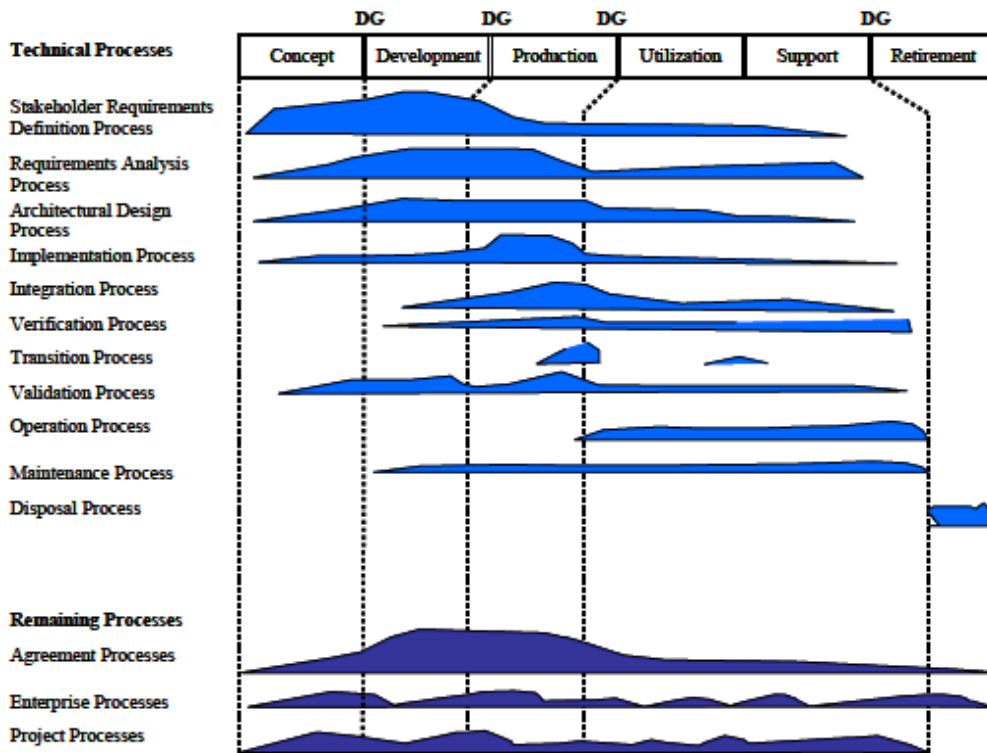


Figure 4. An example of the processes in relation to the lifecycle presented by ISO/IEC 15288

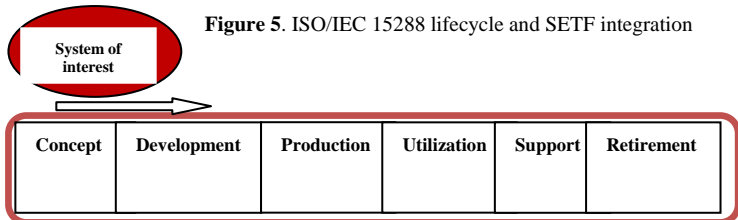
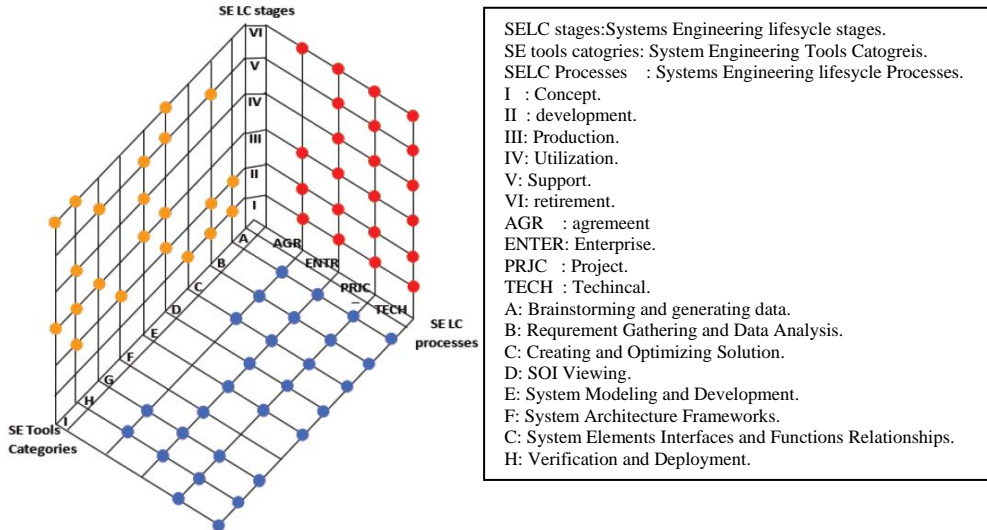


Figure 5. ISO/IEC 15288 lifecycle and SETF integration

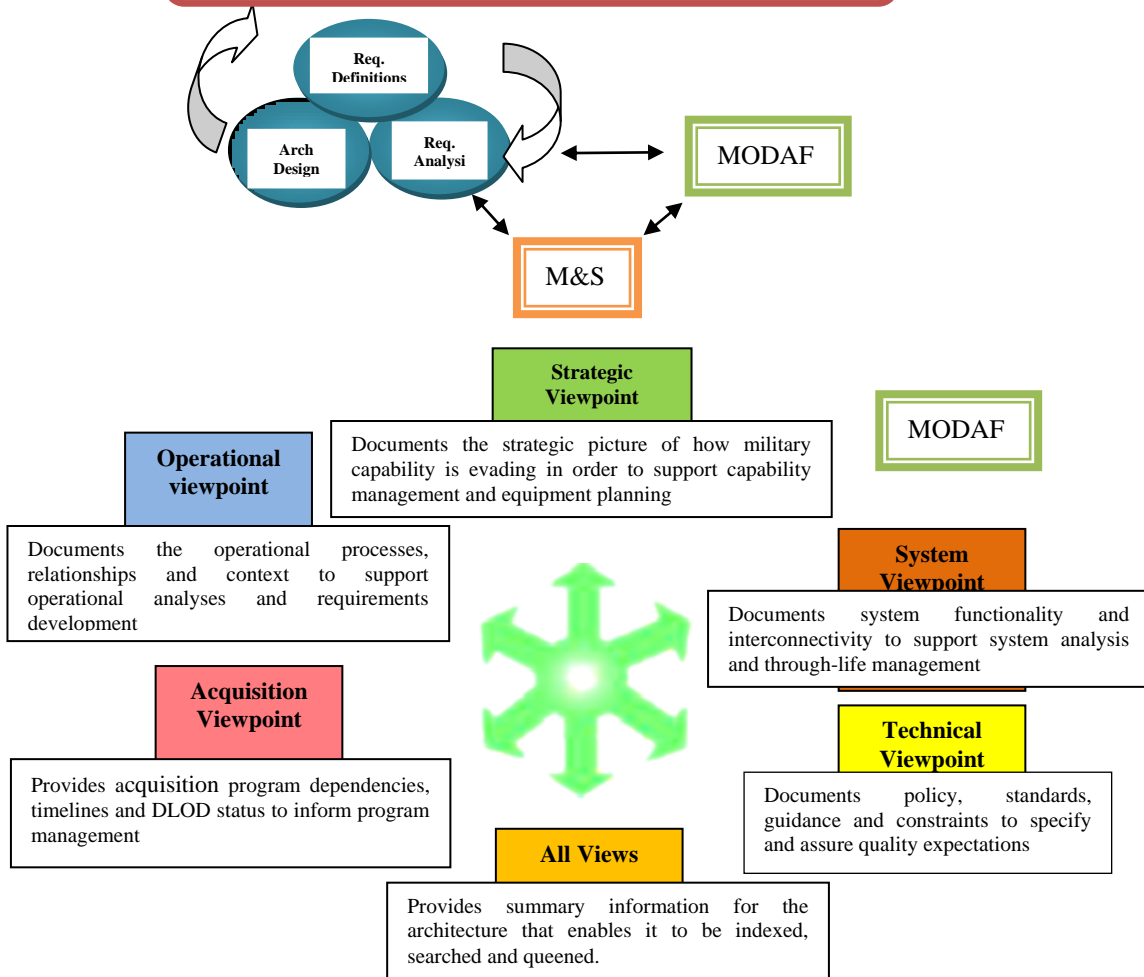


Figure 6: The interplay between SOI, ISO/IEC 15288, MODAF and M&S.

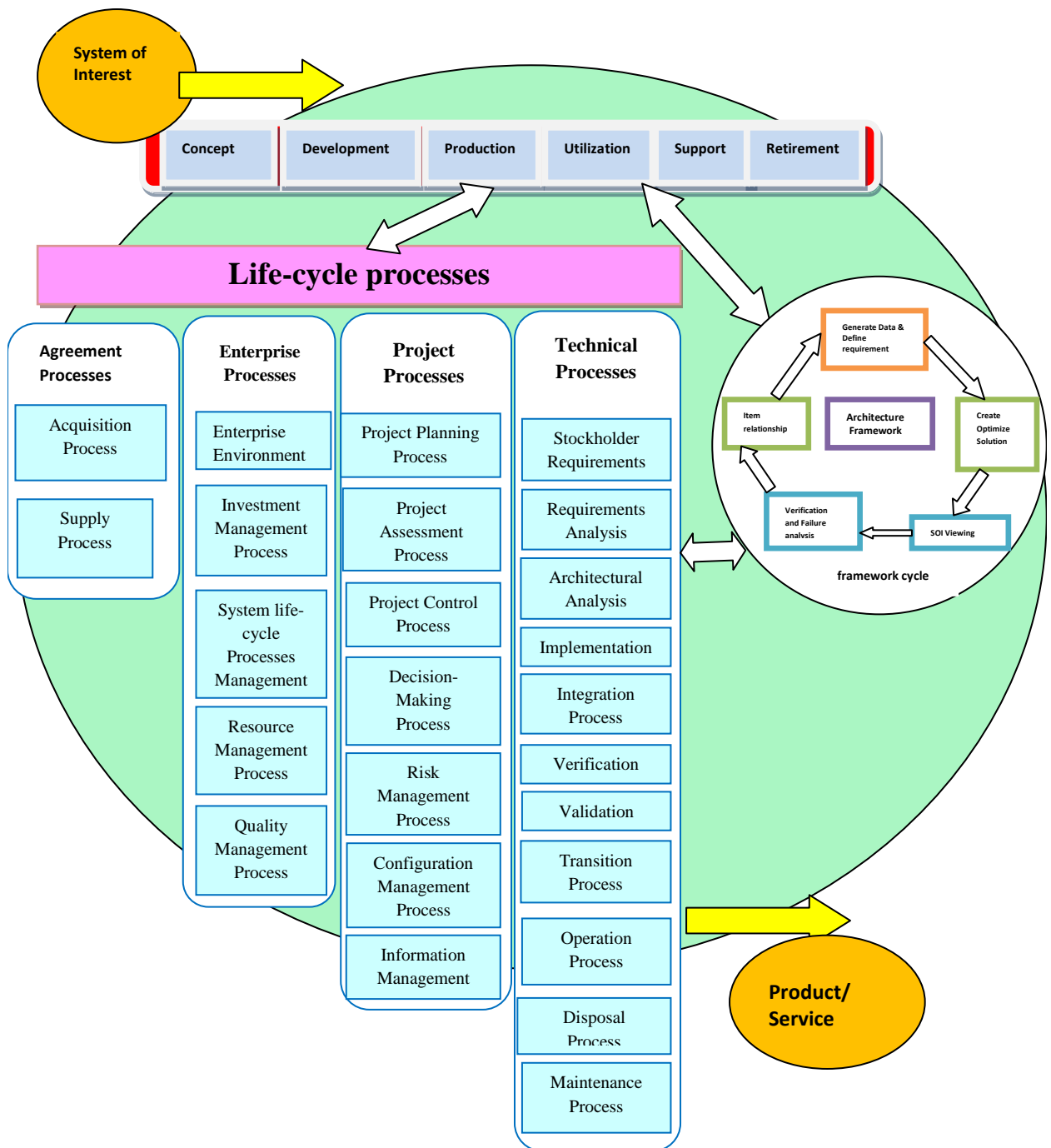


Figure 7. The proposed SELTMF

5. Result and Discussion

The proposed model is applied to an international company for development industries (ECDI); our organization of application has some branches around Egypt for fabricating vehicles metal parts, plastic parts and then delivering to the assembly companies. It is applied to ECDI company system during two quarters (each quarter has three months) one quarter before applying SE tools-model and the second one is

after the application of this study. We got the following results. Figure 8 illustrates the average time spent in each main process in the product life cycle for Qrt.1 that presents the previous situation, e.g., before implementing SELTMF model of this research; Figure 9 presents the Qrt.2 state, e.g., after SELTMF model implementation. As shown in Figure 10, a significant decrease in process time of each process of the implemented quarter, Qrt.2, that gives a chance for more system improvement thus finding new businesses, acquiring new customers,

increasing products, and increasing profit. Through performance analysis these results are presented in Table 2.

These results show that the increase of input (cost) with increases of output (revenue) consequently increasing material consuming, labor hiring, overtime, concerning products quality, decreasing rework, scrap, M/C downtime, and commitment to delivery time thus fulfillment customer needs and handling its claims properly. As a global result, increasing the number of customers and new products, and definitely increasing the value added as illustrated in Figures 11 up to 32. The analysis of the company performance ensures that due to SELTMF model application, the company started to improve its performance as illustrated by measures. Noticed is the increasing of the firm total productivity by 28.1% as shown in Figure 11. This may be due to the increase of the partial productivity. As shown in Figure 12, the increase of the labor partial productivity is 39.4%.

Moreover, material partial productivity increased by 16.7%, as shown in Figure 13. This may be due to the decrease of the material scrap. The inventory level of raw materials is increased by 40%, as shown in Figure 14. This may be due to the decrease of the material scrap and rework. Consequently, the increase of profit by 66.9%, as illustrated by Figure 15, that is for financial management improvement, takes place. According to internal business improvement, there is an increase by 20% for unit cost, meaning increasing its price, as shown in Figures 16 and Figure 17, illustrating that overtime is the same, but Figure 18 illustrates the significant positive decrease in overall cycle time of the product lifecycle.

On another side, the stability of downtime is given in Figure 19. To improve quality, the defective products percentage decreased as plotted in Figure 20; it must be prevented from the beginning through decreasing rework, as presented in Figure 23. Due to this improvement, the company acquired new customers, as shown in Figure 22, became deliver orders on time as required, as presented in Figure 23, thus the lead time has to be decreased, as shown in Figure 24. Based on improving quality programs, customer claims would be, as soon as possible, solved as illustrated in Figure 25. All

this exertion would not be done without a human factor; so they should be update to get different training programs through establishing periodic training programs for all the employees, as shown in Figure 26 and recording each employee training hours by its own training card, as shown in Figure 27. From Figure 28, the total processing time decreased due to decreasing time spent in each process. They are doing the all work thus the company gets new products, as shown in Figure 29. The overall view is clear by measuring global indicators for the whole systems. So, measuring quality-productivity index indicates an increase by 27.6%, as illustrated in Figure 30. Of course, after all this effort, there must be a value added that truly increased by 54.3%, as shown in Figure 31; and if it is compared to the variable costs of material cost, for example, it indicates an increase by 23.8% of the value added percent, as shown in Figure 32.

## 5. Conclusion

An integrated system engineering framework was developed and tested for its implementation on a large industrial scale; from the results the following pertaining conclusions could be drawn:

- The adopted framework included service-oriented point of view that leads to a deeper understanding of the service requirements and its effect on the process.
- The implementation of the framework to first quarter data of a large-scale company that includes six different processes, indicating that assembly, injection and pre-treatment are the main prolonged processes
- After problem identifications and re-evaluation of the industrial process performance, the process time notably decreased for the six processes and epically for injection and assembly processes.
- The key performance measures were compared before and after the solution of the problems and it was found that the total and partial productivity increased considerably, the percentage of defective products reduced, and added values increased.

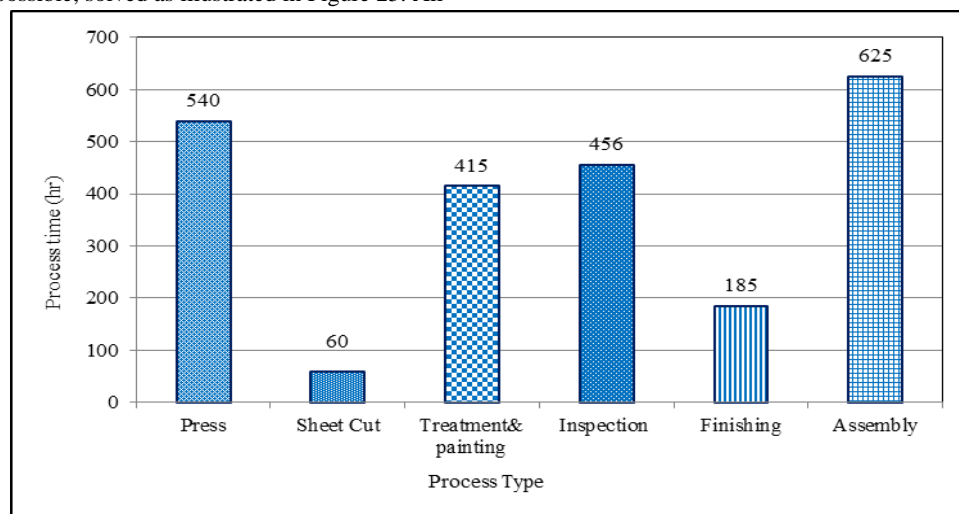


Figure 8. Time spent in each process - Qrt.1 (current) - for ECDI firm

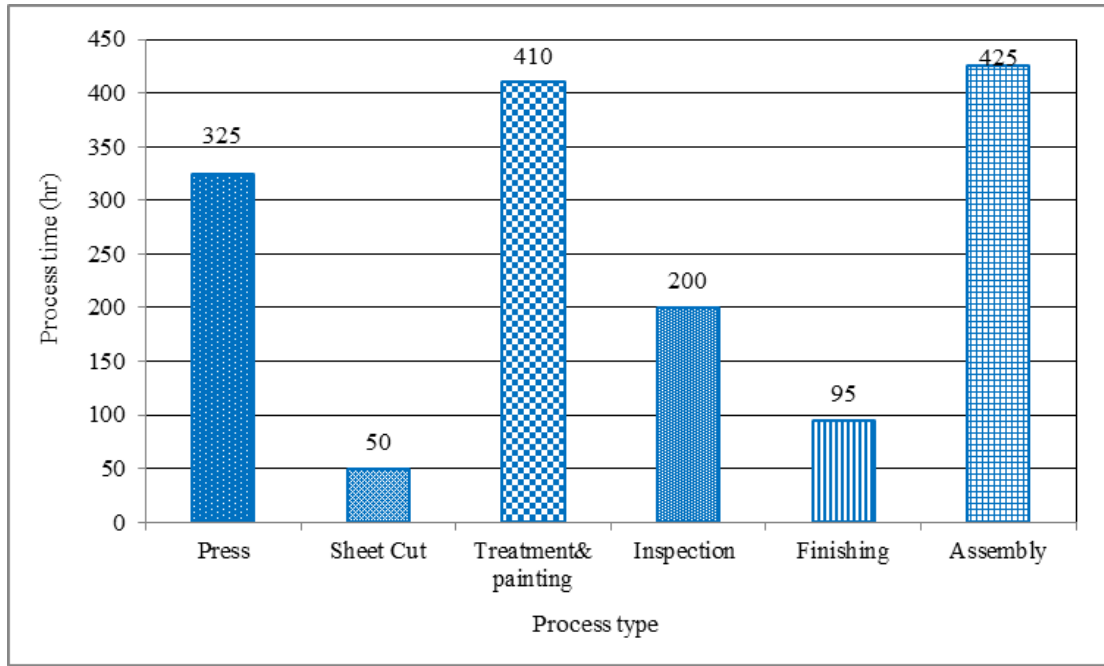


Figure 9. Time spent in each process - Qrt.2 (implemented) - for ECDI firm

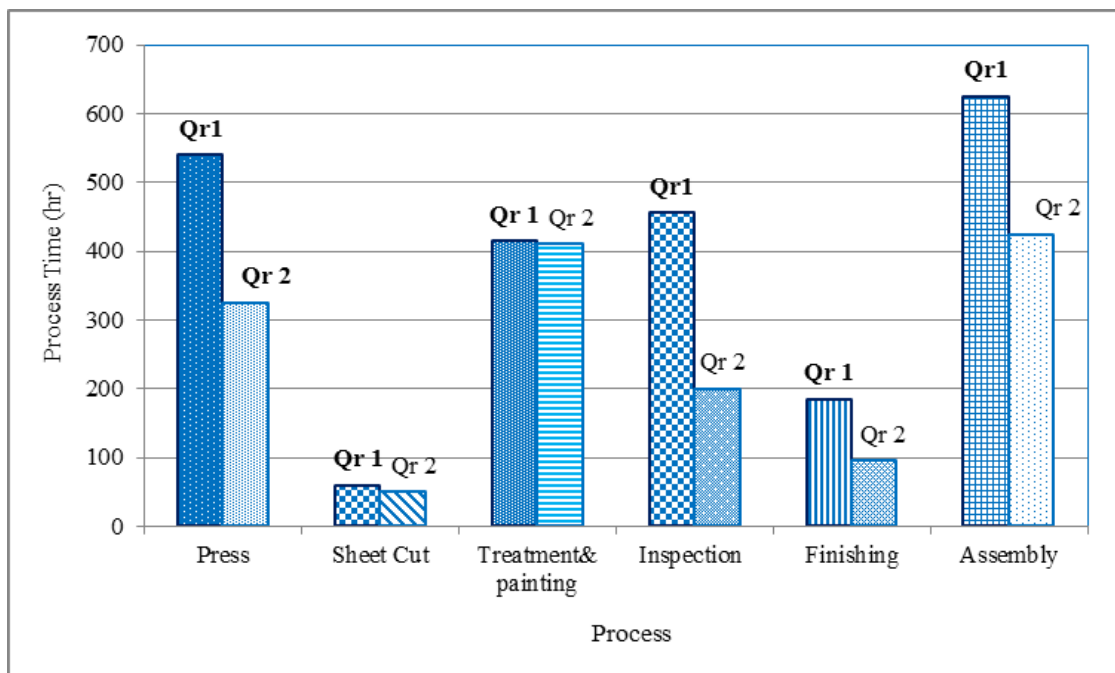


Figure 10. Comparison of time spent in each process for Qrt.1 to Qrt.2 - for ECDI firm

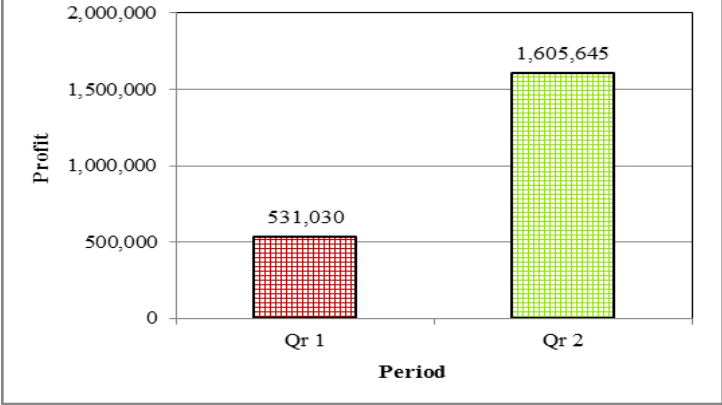
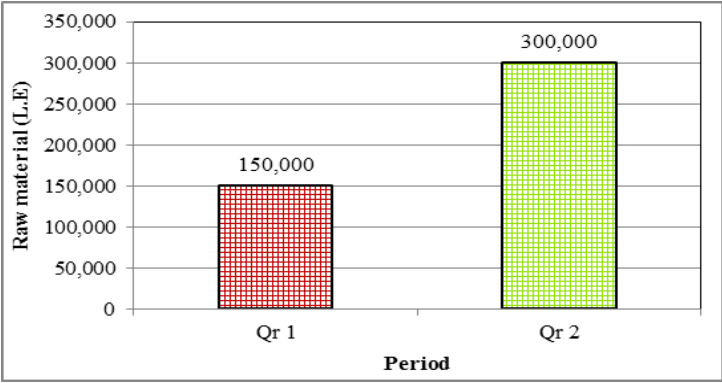
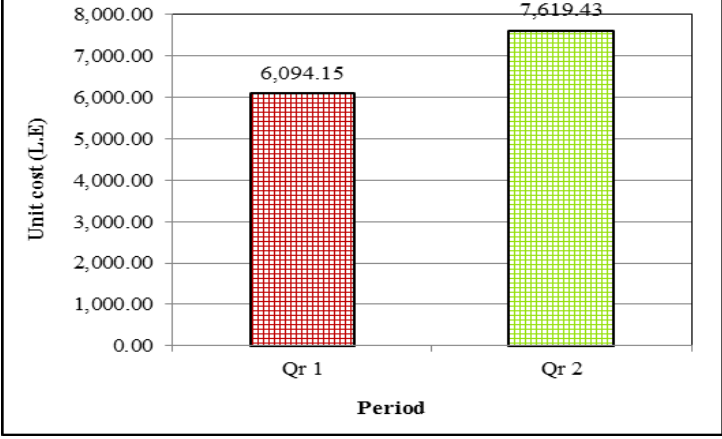
**Table 2.** KPIs results analysis

Perspective	KPIs	Period of comparison						
		Qrt.1 (current) : Qrt. 2 (implemented)						
Financial	Total Productivity of Firm (TPF)	<p>A bar chart comparing TPF for Qrt 1 and Qrt 2. The y-axis is labeled 'TPF' and ranges from 0 to 2.5. The x-axis is labeled 'Period' with categories 'Qr 1' and 'Qr 2'. The bar for Qrt 1 is red with a grid pattern and has a value of 1.548. The bar for Qrt 2 is green with a grid pattern and has a value of 2.152.</p> <table border="1"> <thead> <tr> <th>Period</th> <th>TPF</th> </tr> </thead> <tbody> <tr> <td>Qr 1</td> <td>1.548</td> </tr> <tr> <td>Qr 2</td> <td>2.152</td> </tr> </tbody> </table>	Period	TPF	Qr 1	1.548	Qr 2	2.152
	Period	TPF						
	Qr 1	1.548						
Qr 2	2.152							
Partial Productivity of Labors (PPL)	<p>A bar chart comparing PPL for Qrt 1 and Qrt 2. The y-axis is labeled 'PPL' and ranges from 0 to 16. The x-axis is labeled 'Period' with categories 'Qr 1' and 'Qr 2'. The bar for Qrt 1 is red with a grid pattern and has a value of 8.338. The bar for Qrt 2 is green with a grid pattern and has a value of 13.765.</p> <table border="1"> <thead> <tr> <th>Period</th> <th>PPL</th> </tr> </thead> <tbody> <tr> <td>Qr 1</td> <td>8.338</td> </tr> <tr> <td>Qr 2</td> <td>13.765</td> </tr> </tbody> </table>	Period	PPL	Qr 1	8.338	Qr 2	13.765	
Period	PPL							
Qr 1	8.338							
Qr 2	13.765							
Partial Productivity of Materials (PPM)	<p>A bar chart comparing PPM for Qrt 1 and Qrt 2. The y-axis is labeled 'PPM' and ranges from 0 to 3.5. The x-axis is labeled 'Period' with categories 'Qr 1' and 'Qr 2'. The bar for Qrt 1 is red with a grid pattern and has a value of 2.77. The bar for Qrt 2 is green with a grid pattern and has a value of 3.333.</p> <table border="1"> <thead> <tr> <th>Period</th> <th>PPM</th> </tr> </thead> <tbody> <tr> <td>Qr 1</td> <td>2.77</td> </tr> <tr> <td>Qr 2</td> <td>3.333</td> </tr> </tbody> </table>	Period	PPM	Qr 1	2.77	Qr 2	3.333	
Period	PPM							
Qr 1	2.77							
Qr 2	3.333							

**Figure 11.** TPF comparison of Qrt.1 & Qrt2.

**Figure 12.** Labors productivity comparison of Qrt.1 & Qrt.2

**Figure 13.** Material productivity comparison of Qrt.1&Qrt.2

Perspective	KPIs	Period of comparison						
		Qrt.1 (current) : Qrt. 2 (implemented)						
	Profit (L.E)	 <p>A bar chart comparing profit for Qrt.1 and Qrt.2. The y-axis is labeled 'Profit' and ranges from 0 to 2,000,000 in increments of 500,000. The x-axis is labeled 'Period' with categories 'Qr 1' and 'Qr 2'. The bar for Qr 1 is red with a grid pattern and has a value of 531,030. The bar for Qr 2 is green with a grid pattern and has a value of 1,605,645.</p> <table border="1"> <thead> <tr> <th>Period</th> <th>Profit (L.E)</th> </tr> </thead> <tbody> <tr> <td>Qr 1</td> <td>531,030</td> </tr> <tr> <td>Qr 2</td> <td>1,605,645</td> </tr> </tbody> </table>	Period	Profit (L.E)	Qr 1	531,030	Qr 2	1,605,645
	Period	Profit (L.E)						
Qr 1	531,030							
Qr 2	1,605,645							
<p><b>Figure 14. Profit comparison of Qrt.1 &amp; Qrt.2</b></p>								
	Inventory Level (Raw material) (L.E)	 <p>A bar chart comparing raw material inventory for Qrt.1 and Qrt.2. The y-axis is labeled 'Raw material (L.E)' and ranges from 0 to 350,000 in increments of 50,000. The x-axis is labeled 'Period' with categories 'Qr 1' and 'Qr 2'. The bar for Qr 1 is red with a grid pattern and has a value of 150,000. The bar for Qr 2 is green with a grid pattern and has a value of 300,000.</p> <table border="1"> <thead> <tr> <th>Period</th> <th>Raw material (L.E)</th> </tr> </thead> <tbody> <tr> <td>Qr 1</td> <td>150,000</td> </tr> <tr> <td>Qr 2</td> <td>300,000</td> </tr> </tbody> </table>	Period	Raw material (L.E)	Qr 1	150,000	Qr 2	300,000
	Period	Raw material (L.E)						
Qr 1	150,000							
Qr 2	300,000							
<p><b>Figure 15. Material inventory comparison of Qrt.1 &amp; Qrt.2</b></p>								
Internal Business	Unit Cost (L.E)	 <p>A bar chart comparing unit cost for Qrt.1 and Qrt.2. The y-axis is labeled 'Unit cost (L.E)' and ranges from 0.00 to 8,000.00 in increments of 1,000.00. The x-axis is labeled 'Period' with categories 'Qr 1' and 'Qr 2'. The bar for Qr 1 is red with a grid pattern and has a value of 6,094.15. The bar for Qr 2 is green with a grid pattern and has a value of 7,619.43.</p> <table border="1"> <thead> <tr> <th>Period</th> <th>Unit cost (L.E)</th> </tr> </thead> <tbody> <tr> <td>Qr 1</td> <td>6,094.15</td> </tr> <tr> <td>Qr 2</td> <td>7,619.43</td> </tr> </tbody> </table>	Period	Unit cost (L.E)	Qr 1	6,094.15	Qr 2	7,619.43
Period	Unit cost (L.E)							
Qr 1	6,094.15							
Qr 2	7,619.43							
<p><b>Figure 16. Unit cost comparison of Qrt.1 &amp; Qrt.2</b></p>								

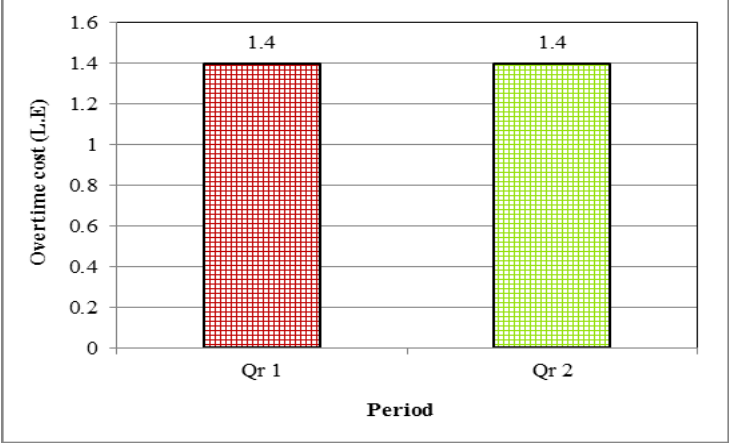
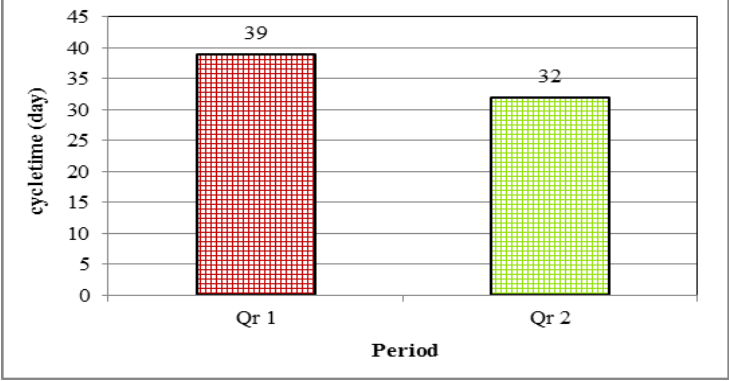
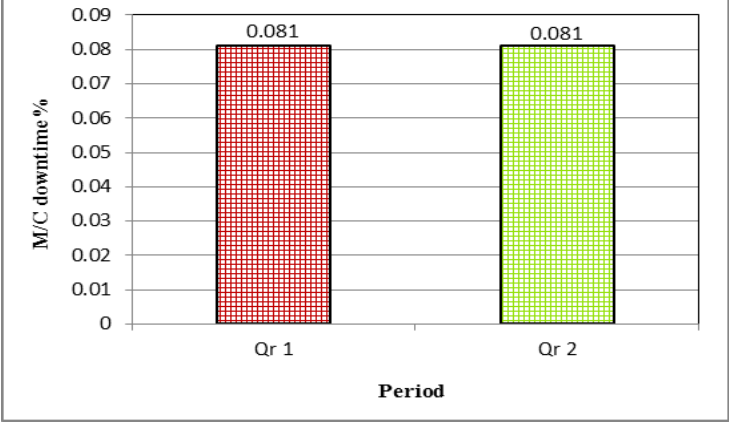
Perspective	KPIs	Period of comparison
		Qrt.1 (current) : Qrt. 2 (implemented)
	Over Time Cost (L.E)	 <p>A bar chart comparing overtime costs for Qr 1 and Qr 2. The y-axis is labeled 'Overtime cost (L.E)' and ranges from 0 to 1.6 in increments of 0.2. The x-axis is labeled 'Period' with categories 'Qr 1' and 'Qr 2'. The bar for Qr 1 is red with a grid pattern and has a value of 1.4. The bar for Qr 2 is green with a grid pattern and also has a value of 1.4.</p>
	Overall Cycle Time (day)	 <p>A bar chart comparing overall cycle times for Qr 1 and Qr 2. The y-axis is labeled 'cycletime (day)' and ranges from 0 to 45 in increments of 5. The x-axis is labeled 'Period' with categories 'Qr 1' and 'Qr 2'. The bar for Qr 1 is red with a grid pattern and has a value of 39. The bar for Qr 2 is green with a grid pattern and has a value of 32.</p>
	M/C Down Time %	 <p>A bar chart comparing M/C downtime percentages for Qr 1 and Qr 2. The y-axis is labeled 'M/C downtime %' and ranges from 0 to 0.09 in increments of 0.01. The x-axis is labeled 'Period' with categories 'Qr 1' and 'Qr 2'. The bar for Qr 1 is red with a grid pattern and has a value of 0.081. The bar for Qr 2 is green with a grid pattern and also has a value of 0.081.</p>

Figure 17. Overtime comparison of Qrt.1 & Qrt.

Figure 18. Time cycle comparison of Qrt.1 & Qrt.2

Figure 19. M/C downtime % comparison of Qrt.1 & Qrt.2

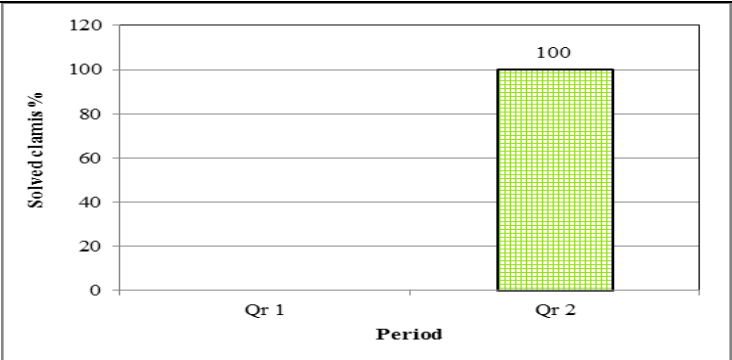
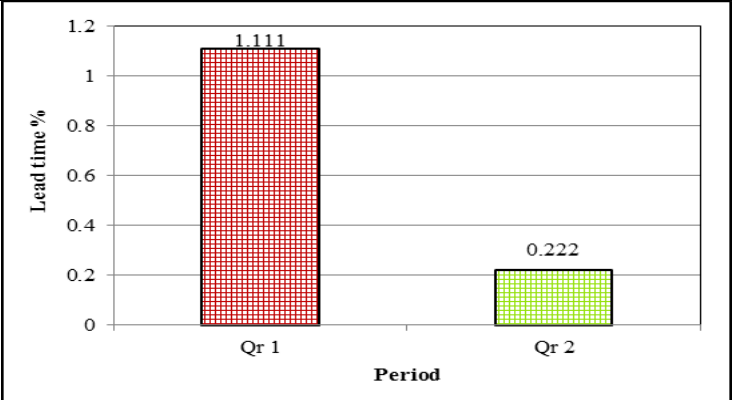
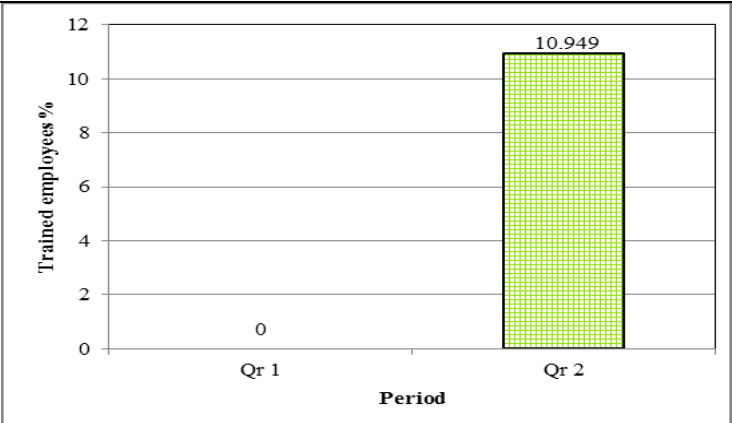
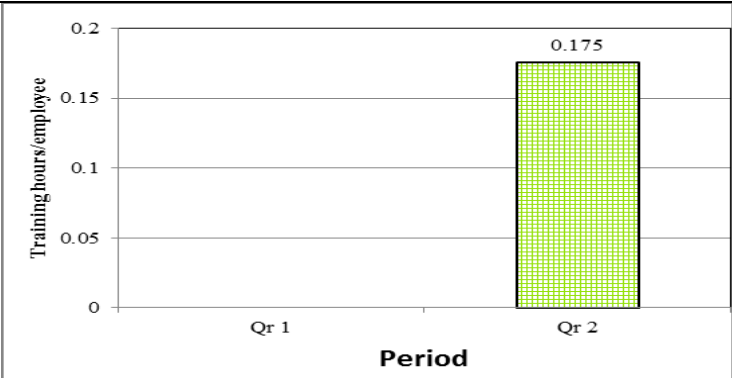
Perspective	KPIs	Period of comparison						
		Qrt.1 (current) : Qrt. 2 (implemented)						
Quality	Defective products %	<p>A bar chart comparing the percentage of defective products between Qr 1 and Qr 2. The y-axis is labeled 'Defective product %' and ranges from 0 to 2.5. The x-axis is labeled 'Period' with categories 'Qr 1' and 'Qr 2'. The bar for Qr 1 is red with a grid pattern and has a value of 2.189. The bar for Qr 2 is green with a grid pattern and has a value of 0.447.</p> <table border="1"> <thead> <tr> <th>Period</th> <th>Defective product %</th> </tr> </thead> <tbody> <tr> <td>Qr 1</td> <td>2.189</td> </tr> <tr> <td>Qr 2</td> <td>0.447</td> </tr> </tbody> </table>	Period	Defective product %	Qr 1	2.189	Qr 2	0.447
	Period	Defective product %						
	Qr 1	2.189						
	Qr 2	0.447						
Rework %	<p>A bar chart comparing the percentage of rework between Qr 1 and Qr 2. The y-axis is labeled 'New customers %' and ranges from 0 to 16. The x-axis is labeled 'Period' with categories 'Qr 1' and 'Qr 2'. The bar for Qr 1 is at 0. The bar for Qr 2 is green with a grid pattern and has a value of 15.</p> <table border="1"> <thead> <tr> <th>Period</th> <th>New customers %</th> </tr> </thead> <tbody> <tr> <td>Qr 1</td> <td>0</td> </tr> <tr> <td>Qr 2</td> <td>15</td> </tr> </tbody> </table>	Period	New customers %	Qr 1	0	Qr 2	15	
Period	New customers %							
Qr 1	0							
Qr 2	15							
New Customers %	<p>A bar chart comparing the percentage of new customers between Qrt. 1 and Qrt. 2. The y-axis is labeled 'New customers %' and ranges from 0 to 16. The x-axis is labeled 'Period' with categories 'Qrt. 1' and 'Qrt. 2'. The bar for Qrt. 1 is at 0. The bar for Qrt. 2 is blue with diagonal lines and has a value of 15.</p> <table border="1"> <thead> <tr> <th>Period</th> <th>New customers %</th> </tr> </thead> <tbody> <tr> <td>Qrt. 1</td> <td>0</td> </tr> <tr> <td>Qrt. 2</td> <td>15</td> </tr> </tbody> </table>	Period	New customers %	Qrt. 1	0	Qrt. 2	15	
Period	New customers %							
Qrt. 1	0							
Qrt. 2	15							
On-Time Delivered Order %	<p>A bar chart comparing the percentage of on-time delivered orders between Qr 1 and Qr 2. The y-axis is labeled 'On time order %' and ranges from 0 to 90. The x-axis is labeled 'Period' with categories 'Qr 1' and 'Qr 2'. The bar for Qr 1 is at 0. The bar for Qr 2 is green with a grid pattern and has a value of 77.778.</p> <table border="1"> <thead> <tr> <th>Period</th> <th>On time order %</th> </tr> </thead> <tbody> <tr> <td>Qr 1</td> <td>0</td> </tr> <tr> <td>Qr 2</td> <td>77.778</td> </tr> </tbody> </table>	Period	On time order %	Qr 1	0	Qr 2	77.778	
Period	On time order %							
Qr 1	0							
Qr 2	77.778							

Figure 20: Defective products % comparison of Qrt.1 & Qrt.2

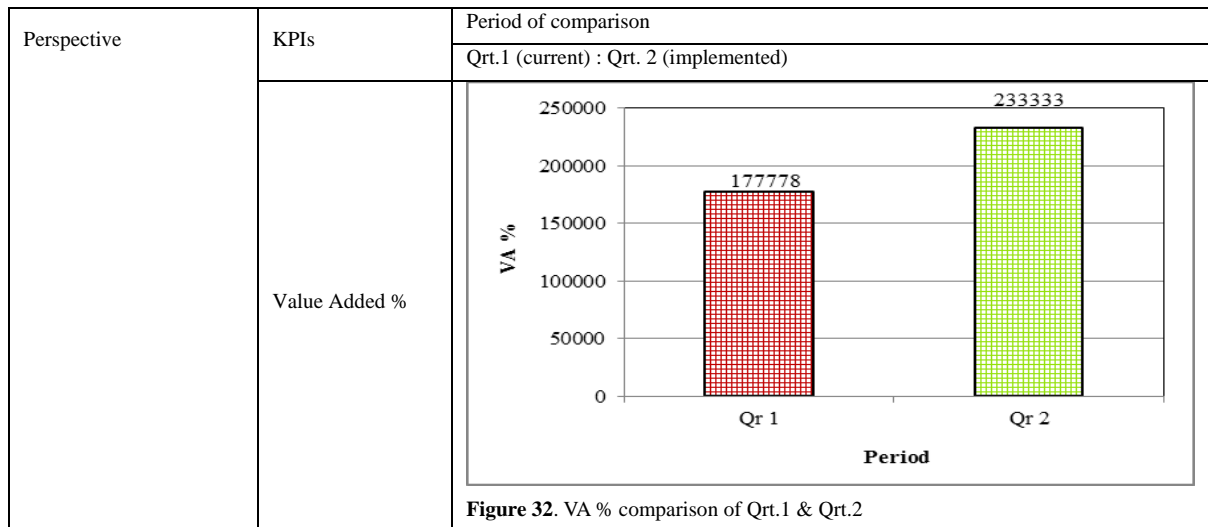
Figure 21. Rework % comparison of Qrt.1 & Qrt.2

Figure 22. New customers % comparison of Qrt.1 & Qrt.2

Figure 23. On-time delivered orders % comparison of Qrt.1 & Qrt.2

Perspective	KPIs	Period of comparison						
		Qrt.1 (current) : Qrt. 2 (implemented)						
	Solved Claims (Customer Complaints) %	 <p>A bar chart comparing 'Solved claims %' for two periods: Qrt 1 and Qrt 2. The y-axis is labeled 'Solved claims %' and ranges from 0 to 120 in increments of 20. The x-axis is labeled 'Period' with categories 'Qr 1' and 'Qr 2'. The bar for Qrt 1 has a value of 0. The bar for Qrt 2 has a value of 100.</p> <table border="1"> <thead> <tr> <th>Period</th> <th>Solved claims %</th> </tr> </thead> <tbody> <tr> <td>Qr 1</td> <td>0</td> </tr> <tr> <td>Qr 2</td> <td>100</td> </tr> </tbody> </table>	Period	Solved claims %	Qr 1	0	Qr 2	100
	Period	Solved claims %						
Qr 1	0							
Qr 2	100							
		<b>Figure 24.</b> Solved claims % comparison of Qrt.1 & Qrt.2						
	Average Lead Time %	 <p>A bar chart comparing 'Average Lead Time %' for two periods: Qrt 1 and Qrt 2. The y-axis is labeled 'Lead time %' and ranges from 0 to 1.2 in increments of 0.2. The x-axis is labeled 'Period' with categories 'Qr 1' and 'Qr 2'. The bar for Qrt 1 has a value of 1.111. The bar for Qrt 2 has a value of 0.222.</p> <table border="1"> <thead> <tr> <th>Period</th> <th>Average Lead Time %</th> </tr> </thead> <tbody> <tr> <td>Qr 1</td> <td>1.111</td> </tr> <tr> <td>Qr 2</td> <td>0.222</td> </tr> </tbody> </table>	Period	Average Lead Time %	Qr 1	1.111	Qr 2	0.222
	Period	Average Lead Time %						
Qr 1	1.111							
Qr 2	0.222							
		<b>Figure 25.</b> Average lead time comparison of Qrt.1 & Qrt.2						
Innovation & Training	Trained Employees %	 <p>A bar chart comparing 'Trained employees %' for two periods: Qrt 1 and Qrt 2. The y-axis is labeled 'Trained employees %' and ranges from 0 to 12 in increments of 2. The x-axis is labeled 'Period' with categories 'Qr 1' and 'Qr 2'. The bar for Qrt 1 has a value of 0. The bar for Qrt 2 has a value of 10.949.</p> <table border="1"> <thead> <tr> <th>Period</th> <th>Trained employees %</th> </tr> </thead> <tbody> <tr> <td>Qr 1</td> <td>0</td> </tr> <tr> <td>Qr 2</td> <td>10.949</td> </tr> </tbody> </table>	Period	Trained employees %	Qr 1	0	Qr 2	10.949
	Period	Trained employees %						
Qr 1	0							
Qr 2	10.949							
		<b>Figure 26.</b> Trained employees % comparison of Qrt.1 & Qrt.2						
	Total Training hours / employee	 <p>A bar chart comparing 'Training hours/employee' for two periods: Qrt 1 and Qrt 2. The y-axis is labeled 'Training hours/employee' and ranges from 0 to 0.2 in increments of 0.05. The x-axis is labeled 'Period' with categories 'Qr 1' and 'Qr 2'. The bar for Qrt 1 has a value of 0. The bar for Qrt 2 has a value of 0.175.</p> <table border="1"> <thead> <tr> <th>Period</th> <th>Training hours/employee</th> </tr> </thead> <tbody> <tr> <td>Qr 1</td> <td>0</td> </tr> <tr> <td>Qr 2</td> <td>0.175</td> </tr> </tbody> </table>	Period	Training hours/employee	Qr 1	0	Qr 2	0.175
	Period	Training hours/employee						
Qr 1	0							
Qr 2	0.175							
		<b>Figure 27.</b> Total training hours / employee comparison of Qrt.1 & Qrt.2						

Perspective	KPIs	Period of comparison						
		Qrt.1 (current) : Qrt. 2 (implemented)						
Integrated Measures	Process time to maturity (hr)	<p>A bar chart comparing total process time in hours between Qrt 1 and Qrt 2. The y-axis is labeled 'Total process time (hr)' and ranges from 0 to 2500 in increments of 500. The x-axis is labeled 'Period' with categories 'Qr 1' and 'Qr 2'. The bar for Qrt 1 is red with a grid pattern and has a value of 2281. The bar for Qrt 2 is green with a grid pattern and has a value of 1500.</p> <table border="1"> <thead> <tr> <th>Period</th> <th>Total process time (hr)</th> </tr> </thead> <tbody> <tr> <td>Qr 1</td> <td>2281</td> </tr> <tr> <td>Qr 2</td> <td>1500</td> </tr> </tbody> </table> <p><b>Figure 28:</b> Total spent time in processes comparison of Qrt. 1 &amp; Qrt. 2</p>	Period	Total process time (hr)	Qr 1	2281	Qr 2	1500
	Period	Total process time (hr)						
	Qr 1	2281						
Qr 2	1500							
No. of New Products	<p>A bar chart comparing the number of new products between Qrt 1 and Qrt 2. The y-axis is labeled 'New products #' and ranges from 0 to 2.5 in increments of 0.5. The x-axis is labeled 'Period' with categories 'Qr 1' and 'Qr 2'. The bar for Qrt 1 is red with a grid pattern and has a value of 0. The bar for Qrt 2 is green with a grid pattern and has a value of 2.</p> <table border="1"> <thead> <tr> <th>Period</th> <th>New products #</th> </tr> </thead> <tbody> <tr> <td>Qr 1</td> <td>0</td> </tr> <tr> <td>Qr 2</td> <td>2</td> </tr> </tbody> </table> <p><b>Figure 29:</b> No. of new products comparison of Qrt.1 &amp; Qrt.2</p>	Period	New products #	Qr 1	0	Qr 2	2	
Period	New products #							
Qr 1	0							
Qr 2	2							
Quality-Productivity Index	<p>A bar chart comparing the Quality-Productivity Index between Qrt 1 and Qrt 2. The y-axis is labeled 'Q-P Index' and ranges from 0 to 3 in increments of 0.5. The x-axis is labeled 'Period' with categories 'Qr 1' and 'Qr 2'. The bar for Qrt 1 is red with a grid pattern and has a value of 1.994. The bar for Qrt 2 is green with a grid pattern and has a value of 2.759.</p> <table border="1"> <thead> <tr> <th>Period</th> <th>Q-P Index</th> </tr> </thead> <tbody> <tr> <td>Qr 1</td> <td>1.994</td> </tr> <tr> <td>Qr 2</td> <td>2.759</td> </tr> </tbody> </table> <p><b>Figure 30:</b> Quality-Productivity index comparison of Qrt.1 &amp; Qrt.2</p>	Period	Q-P Index	Qr 1	1.994	Qr 2	2.759	
Period	Q-P Index							
Qr 1	1.994							
Qr 2	2.759							
	Value Added (VA) (L.E)	<p>A bar chart comparing Value Added (VA) in L.E between Qrt 1 and Qrt 2. The y-axis is labeled 'VA(L.E)' and ranges from 0 to 2,500,000 in increments of 500,000. The x-axis is labeled 'Period' with categories 'Qr 1' and 'Qr 2'. The bar for Qrt 1 is red with a grid pattern and has a value of 960,000. The bar for Qrt 2 is green with a grid pattern and has a value of 2,100,000.</p> <table border="1"> <thead> <tr> <th>Period</th> <th>VA(L.E)</th> </tr> </thead> <tbody> <tr> <td>Qr 1</td> <td>960,000</td> </tr> <tr> <td>Qr 2</td> <td>2,100,000</td> </tr> </tbody> </table> <p><b>Figure 31:</b> VA comparison of Qrt.1 &amp; Qrt.2</p>	Period	VA(L.E)	Qr 1	960,000	Qr 2	2,100,000
Period	VA(L.E)							
Qr 1	960,000							
Qr 2	2,100,000							



## References

- [1] M.A. Nihal, H. A. Islam, A. M. El-kamash, "Addressing Problems by Systems Engineering Methods, Techniques, and Tools-Model Framework". International Journal of Innovative Research in Science, Engineering and Technology, Vol. 2 (2013), 7369-7381.
- [2] Z. Soheil, A. Seyed, G. Mahsa, "Evaluation of Overall Equipment Effectiveness in a Continuous Process Production System of Condensate Stabilization Plant in Assalooyeh". Interdisciplinary Journal of Contemporary Research Business, Vol. 3 (2012), 590-599.
- [3] Z. Ghader, R. Kamaledin, P. Mehdil, K. Majid, "Evaluating the Overall Effectiveness of Production Equipment and Machinery". American Journal of Scientific Research, Issue 31 (2011), 59-68.
- [4] M. František, "Financial Key Performance Indicators in Engineering Companies", Journal of Periodica Polytechnica Social and Management Sciences, vol. 23 (2015), 60-67.
- [5] V. B. Patel, H. R. Thakkar, "Review Study on Improvement of Overall Equipment Effectiveness through Total Productive Maintenance", Journal of Emerging Technologies and Innovative Research, Vol. 1 (2014), 720-726.
- [6] M. Motavallian, "Overall Effectiveness of Equipment". First Edition, Rasa Cultural Services Institute, Tehran, Iran, (2007).
- [7] H. A. Islam, "Studied Implementation of Total Productive Maintenance and Overall Equipment Effectiveness Evaluation". International Journal of Mechanical & Mechatronics Engineering IJMME-IJENS, Vol.13 (2013), 69-75.
- [8] S. Mark, "Software Engineering and Systems Engineering in the Department of Defense". Journal of Defense Software Engineering, (1998), 3 – 6.
- [9] C. Chittister, Y. Y. Haimes, "Harmonizing ABET Accreditation and the Certification of Systems Engineers", Wiley Periodicals, Inc., Correspondence, Syst Eng. Vol. 14 (2010), 341-348.
- [10] M. C. David, "Practical Application of Chaos Theory to Systems Engineering". New Challenges in Systems Engineering and Architecting Conference on Systems Engineering Research (CSER) 2012–St. Louis, MO Cihan H. Dagli, Editor in Chief Organized by Missouri University of Science and Technology, Elsevier Ltd. Selection, Procedia Computer Science Vol. 8 (2012), 39 – 44.
- [11] S. Alice, W. Jon, W. Bill, B. Doug, R. Richard, D. Peter, "Year One of the Systems Engineering Experience Accelerator", New Challenges in Systems Engineering and Architecting Conference on Systems Engineering Research (CSER) (2012) – St. Louis, MO Cihan H. Dagli, Editor in Chief Organized by Missouri University of Science and Technology, Elsevier Ltd. Selection, Procedia Computer Science Vol. 8 (2012), 267 – 272.
- [12] Defense Acquisition University, "Systems Engineering Fundamentals", Press Fort Belvoir, Virginia 22060-5565, 2001.
- [13] Cecilia Haskins, "Systems Engineering Handbook, a Guide for System Lifecycle Processes and Activities". INCOSE-TP-2003-002-03, INCOSE Systems Engineering Handbook, version 3 (2006).
- [14] S. Albert, K. John, "Systems Engineering Framework for Integrated Product and Industrial Design Including Trade Study Optimization". New Challenges in Systems Engineering and Architecting Conference on Systems Engineering Research (CSER), Missouri University of Science and Technology, Elsevier Ltd. Selection, Procedia Computer Science Vol. 8 (2012), 413 – 419.
- [15] P. S. Andrew, "Systems Engineering: Purpose, Function, and Structure". John Wiley & Sons, Inc., Editorials (1998), 1 – 3.
- [16] P. S. Andrew, B. R. William, "Handbook of Systems Engineering and Management - An Introduction to Systems Engineering and Systems Management". John Wiley & Sons, Inc., (1999).
- [17] G. Yariv, D. Dov, "Generating Sys. ML Views from an OPM Model: Design and Evaluation". Systems Engineering, Wiley Periodicals, Inc., Regular Paper, and Syst. Eng Vol. 14 (2011), 327-340.
- [18] E. K. Joseph, Conference Co-Chair, "Preface to Part V, Systems Engineering Applications", New Challenges in Systems Engineering and Architecting Conference on Systems Engineering Research (CSER) (2012) – St. Louis, MO Cihan H. Dagli, Editor in Chief Organized by Missouri University of Science and Technology, Elsevier B.V., Procedia Computer Science Vol.8 (2012), 295 – 296.
- [19] N. Tommy, A. Edberg, H. Byström, M. L. Gustafsson, "Systems Engineering, Architecture Frameworks and Modeling & Simulation", www.modaf.com/file\_download/30





الجامعة الهاشمية



المملكة الأردنية الهاشمية

المجلة الأردنية  
للمهندسة الميكانيكية والصناعية

JJIMIE

مجلة علمية عالمية محكمة  
تصدر بدعم من صندوق البحث العلمي

<http://jjmie.hu.edu.jo/>

ISSN 1995-6665

# المجلة الأردنية للهندسة الميكانيكية والصناعية

## مجلة علمية عالمية محكمة

المجلة الأردنية للهندسة الميكانيكية والصناعية: مجلة علمية عالمية محكمة تصدر عن الجامعة الهاشمية بالتعاون مع صندوق دعم البحث العلمي في الأردن

### هيئة التحرير

#### رئيس التحرير

الأستاذ الدكتور نبيل عناقرة

قسم الهندسة الميكانيكية و الصناعية، الجامعة الهاشمية، الزرقاء، الأردن.

#### الأعضاء

الأستاذ الدكتور ناصر الحنيطي

الأستاذ الدكتور محمد أحمد حمدان

الأستاذ الدكتور ستهيل كيوان

"" " " " " ""

الأستاذ الدكتور محمود زعل ابو زيد

الأستاذ الدكتور امين الربيدي

#### مساعد رئيس هيئة التحرير

الدكتور خالد الوديان

### فريق الدعم

#### تنفيذ وإخراج

م . علي أبو سليمة

#### المحرر اللغوي

الدكتور قصي الذبيان

ترسل البحوث إلى العنوان التالي

رئيس تحرير المجلة الأردنية للهندسة الميكانيكية والصناعية

الجامعة الهاشمية

كلية الهندسة

قسم الهندسة الميكانيكية

الزرقاء - الأردن

هاتف : 00962 5 3903333 فرعي 4537

Email: [jjmie@hu.edu.jo](mailto:jjmie@hu.edu.jo)

Website: [www.jjmie.hu.edu.jo](http://www.jjmie.hu.edu.jo)